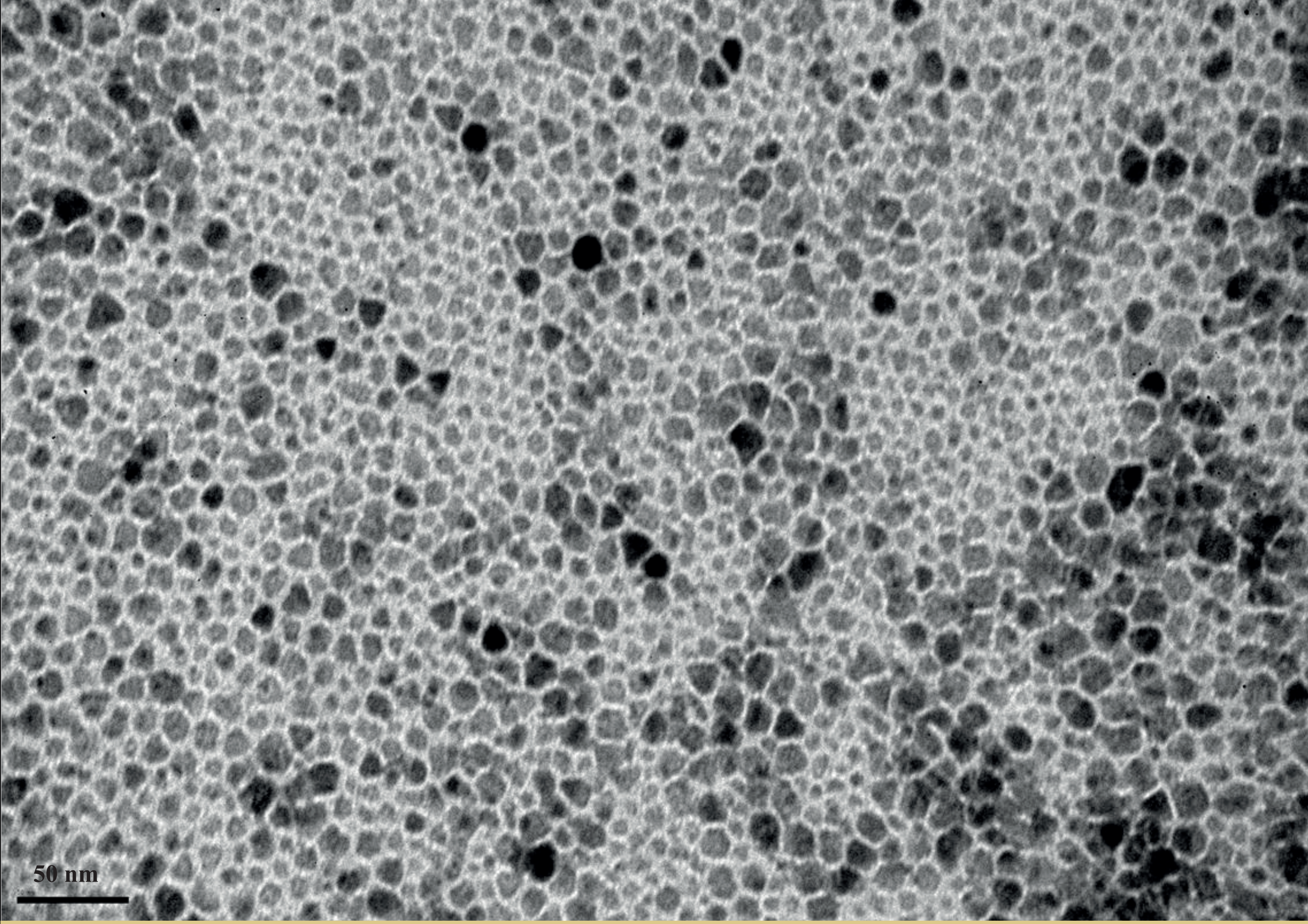

Paulo Henrique da Costa Santos

DEVELOPMENT OF A BIODEGRADABLE NANOFLUID FOR BRAIN DRUG DELIVERY

Development presented to the University of Coimbra to complete the necessary requirements for obtaining the degree of Master Science in Biomedical Engineering, held under scientific orientation of Maria Benilde Faria de Oliveira e Costa, PhD, Luísa Maria Rocha Durães, PhD and Olga Maria Fernandes Borges Ribeiro, PhD

September 2015

· U C ·

UNIVERSIDADE DE COIMBRA

FCTUC FACULDADE DE CIÊNCIAS
E TECNOLOGIA
UNIVERSIDADE DE COIMBRA

Paulo Henrique da Costa Santos

Desenvolvimento de um Nanofluido Biodegradável para Libertação de Fármaco no Cérebro

Dissertação apresentada à Universidade de Coimbra para cumprimento dos requisitos necessários à obtenção do grau de Mestre em Engenharia Biomédica

Orientadores:

Maria Benilde Faria de Oliveira e Costa (CEMDRX, Dep. de Física)

Luísa Maria Rocha Durães (CIEPQPF, Dep. de Engenharia Química)

Olga Maria Fernandes Borges Ribeiro (CNC, Faculdade de Farmácia)

Coimbra, 2015

This work was developed in the following host institutions:

CEMDRX

Centro de Estudos de Materiais por Difração de Raios-X

University of Coimbra, Portugal

CIEPQPF

Chemical Process Engineering and Forest Products Research Centre

University of Coimbra, Portugal

CNC

CENTER FOR NEUROSCIENCE AND CELL BIOLOGY

UNIVERSITY OF COIMBRA, PORTUGAL

Center for Neuroscience and Cell Biology

University of Coimbra, Portugal

“The dictionary is the only place that success comes before work. Work is the key to success, and hard work can help you accomplish anything.”

(Vince Lombardi)

Acknowledgements

First of all, I would like to thank my supervisors, Dr. Benilde Costa, Dr. Luísa Durães and Dr. Olga Borges for giving me the honor and privilege of working with them, for all the guidance provided and the necessary support throughout the course of this work. I would also like to thank the Biomedical Engineer Nuno André Gaspar for advising me during the early stages of this work and for clarifying some doubts during this thesis.

I would also like to acknowledge Professor José António Paixão, coordinator of CEMDRX, who made possible the access to TAIL facilities for the XRD and the VSM analysis on our samples. I would like to thank Dr. Francisco Figueiredo from IBMC (University of Porto) as well, for the knowledge provided and for making the TEM analysis possible. Dr. Benilde Costa (CEMDRX) help also proved to be much valuable during the Mössbauer analysis.

I want to recognize all the people from the research groups for an excellent working environment, providing assistance whenever it was necessary. I would like to leave a special “thank you” note for the Chemistry Engineer Telma Matias and the Biochemistry Master Edna Soares for the help provided throughout the course of the experimental work.

To my family, without their unconditional support and comprehension the elaboration of this thesis would not be possible.

To all my friends, whom were always there in pivotal points of my life, whether good or bad.

Last, but not least, a big thank to Cartonagem Trindade, Lda., for all the financial support and motivation through my entire academic career.

Abstract

Nowadays, there is a great seek of a targeted drug delivery system. Guiding magnetic iron oxide nanoparticles to its target with the help of an external magnetic field is the principle behind the development of superparamagnetic iron oxide nanoparticles (SPIONs) as novelty drug delivery vehicles. The main purpose of this work is to develop an improved biodegradable magnetic nanofluid for drug delivery in the brain. The drug delivery system allies the superparamagnetic versatility of iron oxide nanoparticles with their capacity to increase the therapeutic protein adsorption.

The synthesis method that creates the SPIONs – thermal decomposition, was studied, and different procedures were tested in order to improve the reaction product and to increase the accuracy of the drug delivery targeting. These new procedures evaluated the effect of: changing the initial ratio of oleylamine/benzyl ether (A, B and C), the time for nanocrystals growth (A*, B* and C*), the addition of seeds in the synthesis process (A+A, B+B and C+C) and the amount of the precursor (A(2x) and C(2x)) used on the characteristics of the obtained nanoparticles. The stability of the SPIONs suspensions and their capacity to adsorb proteins (BSA and α-casein) were also tested, as well as the cytotoxicity of the produced SPIONs.

Procedure C(2x) revealed itself the most promising to synthesize high quality, size controlled SPIONS. As desired, DLS, XRD and TEM tests showed an increase of particle sizes (~10 nm) for the samples prepared by this procedure. Although XRD and Mössbauer analysis indicate a mixture between magnetite and maghemite in the particles, the content of magnetite was also increased. VSM results also showed improved magnetization saturation (68 emu/g at 300 K and 78 emu/g at 2 K) with the SPIONs obtained from procedure C(2x). The protein adsorption tests on these SPIONs proved that the adsorption can be enhanced when the dependence relation between the dispersive solution and the protein to be adsorbed was considered.

The obtained results on the characterization performed on the various samples seem promising towards a biodegradable magnetic iron oxide nanofluid for drug delivery in the brain. However, further studies are required in order to improve this drug delivery system and to evaluate the drug releasing kinetics.

Keywords: SPIONs; drug delivery; superparamagnetism; protein adsorption; biodegradable magnetic nanofluid, TEM, XRD, Mössbauer spectroscopy.

Resumo

Os sistemas de libertação localizada de fármaco são uma necessidade atual. A condução de nanopartículas de óxido de ferro até ao seu alvo através de um campo magnético aplicado é o princípio do desenvolvimento de nanopartículas superparamagnéticas de óxido de ferro (SPIONs) como novos veículos de libertação de fármaco. O principal objetivo deste trabalho foi desenvolver um nanofluido magnético biodegradável para libertação de fármacos no cérebro. Um sistema de libertação de fármaco alia a versatilidade associada ao superparamagnetismo das nanopartículas de óxido de ferro, com a sua capacidade de aumentar a adsorção de proteínas terapêuticas.

O método de síntese – decomposição térmica, que cria estes SPIONs foi estudado e, diferentes procedimentos a partir deste método foram testados, de modo a melhorar o produto da reação e a aumentar a eficácia do sistema de libertação localizada de fármaco. Estes novos procedimentos avaliaram o efeito: da alteração do rácio inicial de oleilamina/éter benzílico (A, B e C), do tempo de crescimento dos nanocristais (A*, B* e C*), da adição de sementes no processo de síntese (A+A, B+B e C+C) e da quantidade de precursor (A(2x) e C(2x)) usado; nas características das nanopartículas obtidas. A estabilidade das suspensões de SPIONs e a sua capacidade de adsorver proteínas (BSA e α-caseína) foi também testado, assim como a citoxicidade dos SPIONs produzidos.

O procedimento C(2x) revelou-se o mais promissor na síntese de SPIONs de alta-qualidade e de tamanho controlado. Como era desejado, os testes de DLS, XRD e TEM exibiram um aumento nos tamanhos das partículas (~10 nm) para amostras obtidas por este procedimento. Apesar das análises recorrendo a espectroscopia de Mössbauer e XRD indicarem uma mistura de magnetite e maghemite, o conteúdo de magnetite foi também aumentado. Os resultados obtidos por VSM mostraram uma saturação de magnetização melhorada (68 emu/g a 300 K e 78 emu/g a 2 K) com os SPIONs obtidos pelo procedimento C(2x). Os testes de adsorção proteica nos SPIONs provaram que esta pode ser aprimorada, quando a relação de dependência entre a solução dispersiva e a proteína a ser adsorvida foi considerada.

Os resultados obtidos na caracterização das várias amostras, parecem promissores na obtenção de um nanofluido magnético biodegradável de óxido de ferro para libertação de fármaco no cérebro. Contudo, estudos adicionais são ainda necessários de modo a melhorar o sistema de libertação de fármaco e avaliar a cinética de libertação do mesmo.

Palavras-chave: SPIONs; libertação de fármaco; superparamagnetismo; adsorção proteica; nanofluido magnético biodegradável, TEM, XRD, espectroscopia de Mössbauer.

Acronyms

BBB – Blood-Brain Barrier

BSA – Bovine Serum Albumin

DSC – Differential Scanning Calorimetry

DLS – Dynamic Light Scattering

EELS - Electron Energy Loss Spectrometer

EDS - Energy Dispersive X-ray Spectrometer

FC – Field Cooled

FTIR – Fourier Transform Infra-Red

FWHM – Full Width at Half Maximum

H- Hyperfine magnetic field

$Fe(acac)_3$ - Iron(III) Acetylacetonate

IS – Isomeric Shift

γ-Fe_2O_3 – Maghemite

MRI – Magnetic Resonance Imaging

Fe_3O_4 – Magnetite

PCS - Photon Correlation Spectroscopy

QS – Quadrupole Splitting

QELS - Quasi-Elastic Light Scattering

RT – Room Temperature

SPIONs – Superparamagnetic Iron Oxide Nanoparticles

TGA – Thermal Gravimetric Analysis

TEM – Transmission Electron Microscopy

VSM – Vibrating Sample Magnetometer

XRD – X-Ray Diffraction

ZFC – Zero Field Cooled

List of Figures

List of Tables

Table of Contents

1. Introduction

The actual knowledge and the ability to control the matter at its most fundamental level (atomic and molecular scales), learned by nanoscale science and engineering, allowed the development of systems that have great interest to biomedical applications. In particular, nanoparticles have attracted great attention due to their particular electronic [1], optical [2] and magnetic [3] properties. The nanodimension of these particles enables their use for nanoengineering of surfaces and the production of functional nanostructures. These modifications make easier their application in the biomedical area, for instance, for targeted drug delivery in delicate, damaged and not well-known organs, like the brain.

The main problems usually associated with drug administration include the general systemic distribution of therapeutic drugs, the necessity of a large dose to properly achieve the desired site, the lack of drug specificity towards a pathological site, nonspecific toxicity, and other adverse side effects. The use of superparamagnetic iron oxide nanoparticles (SPIONs) is one of the main solutions to overcome the mentioned problems of drug delivery involving magnetic targeting. Their inherent superparamagnetism provides them the ability of being targeted to the required area through an external magnetic field application, as they behave like a giant paramagnetic atom granting a quick response to the applied magnetic fields with negligible remnant magnetization momentum and coercivity. This is a fundamental aspect in biomedical applications since it decreases the risk of forming agglomerates [4]. Due to such properties, the particles do not show magnetic interaction after the removal of the external magnetic field. The concept of using magnetic carriers coupled with an external magnetic field was firstly introduced in the late 1970s by Freeman *et al.* [5]; nowadays, a variety of magnetic nanoparticle carriers have been developed and optimized to deliver drugs to target sites in vivo [6–8]. The optimization of these carriers has two main goals: to reduce both the amount of accumulated systemic distribution of the cytotoxic drug and the dosage required by more efficient, localised targeting of the drug.

Magnetic targeting is related with a magnetic force applied on SPIONs by a magnetic field gradient. The therapy efficiency depends on some significant parameters such as: the mentioned field gradient, the field strength and the volumetric and magnetic properties of the particles. The magnetic field gradient is generated by a strong permanent magnet fixed outside the body over the target site. The drug-carrier complexes, usually a biocompatible nanofluid, are normally injected into the patient via the circulatory system. Once the drug-carrier complexes are concentrated at the target, the drug is released either via enzymatic activity or changes in environment physiological conditions such as pH, osmolality, or temperature [6], and may be internalized by the cells of the target tissue [9].

SPIONs application in medical therapy associated to pathologies in the brain requires their stabilization in water at neutral pH and physiological salinity. Such dispersion stability depends on the dimensions of the particles, which should be sufficiently small to avoid precipitation due to gravity forces.

Nanoparticles size affects their ability to extravasate from the vasculature. While most endothelial barriers allow nanoparticles <150 nm in diameter to pass, more stringent barriers, such as the blood-brain barrier (BBB) are far more restrictive. The BBB allows passive diffusion of only small, neutrally charged lipid soluble molecules, prohibiting >98% of all potential neurotherapeutics from passing through it. Consequently, this has become an area of intense research in the development of treatment strategies for brain tumors, Parkinson's, Alzheimer's, and Huntington's diseases. To determine the influence of nanoparticles size on BBB permeability, Sonavane *et al.* recently reported that gold nanoparticles of 20 to 50 nm in hydrodynamic size could permeate across the BBB, while larger nanoparticles, specifically 100 and 200 nm sized could not. However, BBB permeability is likely influenced by all physicochemical properties of the drug delivery system and nanoparticles size alone may not dictate their permeability across the BBB [10].

Another important factor is the charge and surface chemistry, which gives rise to both steric and coulombic repulsions [11]. Because of their oxidative instability, SPIONs must have a protective shell against degradation. This shell is also used to bind specific drugs, proteins, enzymes, antibodies and other molecular targets [12].

Other important criteria to take into account for their biomedical applications is the cytotoxicity of SPIONs. The nature of the magnetically responsive component and the final size of the particles, including their core and the coatings, are some aspects that determine their cytotoxicity [13].

Also, targeting SPIONs into specific cells is an important issue. It is severely limited by a short blood half-life of the particles, non-specific targeting, and low internalization efficiency of surface grafted ligands [13]. Various efforts are directed towards improving these properties of SPIONs and modifying their synthesis methods to better control their size and surface.

During the development of this thesis, drug delivery using SPIONs as carriers will be studied, but their use in other applications is also important: their use in high resolution molecular imaging and in cancer treatments by hyperthermia has also been in development and shows promising results [12][14].

1.1. Objectives and motivation

During the development of this thesis we intended to study into further detail the synthesis of superparamagnetic iron oxide nanoparticles obtained by thermal decomposition of iron acetylacetonates. To have an accurate knowledge of the process involved in this synthesis, several aspects that could affect the reaction were addressed, such as the use of different amounts of the iron precursor, nucleation and growth times, as well as various ratios between solvent and surfactant.

Besides studying the effect of some synthesis parameters on the iron oxide nanoparticles characteristics, the observation of the effects of coating the nanoparticles with some surfactants and posterior protein loading on their properties were also investigated. The proteins that were more efficiently adsorbed on the obtained nanoparticles in an administration environment were also selected.

Mössbauer spectroscopy and XRD analysis were the main techniques used to determine the formed iron oxide phases. TEM and DLS were applied to accurately determine the nanoparticles size. FTIR allowed to confirm the presence of the chemical groups on the protective shell of the nanoparticles. VSM allowed us to quantify the magnetic properties of the prepared nanoparticles. The Zeta Potential was also applied to determine the surface charge of the nanoparticles in different pH solutions with the aim of better selecting the more interesting therapeutic protein loaded on the nanoparticles and determining the efficiency of its adsorption. The samples were also subjected to cytotoxic analysis to confirm their biocompatibility.

As motivation, it is expected that this work will contribute to a better understanding of the studied nanoparticles synthesis method and properties, and assess the effects and changes in their properties when they are treated with different surfactants and/or loaded with different therapeutic proteins. We believe that this will help the further development of the application of a biodegradable nanofluid as a vector for drug release in the human brain.

1.2. Thesis outline

This thesis was organized in six chapters. In the present chapter, chapter 1, the framework objectives and motivation for this work and a brief summary of contents are presented.

In chapter 2, the basic theoretical concepts related to magnetism and the type of magnetization phenomena exhibit by the nanoparticles with interest for this work are explained. Furthermore, some information related to SPIONs as drug delivery carriers and their synthesis methods will be described, as well as the basic principles needed to understand the characterization techniques applied in this work.

Chapter 3 will focus on enlightening the used experimental methodology. A detailed description of the experimental assembly and the steps of the original synthesis method (based on literature) and its modifications, which were developed during the course of this work; will be done throughout this chapter. Chapter 3 also contains the methodologies for characterizing the samples with the different analytical techniques.

All the chosen routes will be explained and the obtained results will be discussed in chapters 4 and 5. Chapter 4 will mainly focus on the physical analysis of the samples such as nanoparticles size, their oxide phase, magnetic properties, and chemical groups of their protective shell. Chapter 5 discusses the influence of surfactant coating in SPIONs stability of water dispersions, the SPIONs cytotoxic results, and the protein adsorption quantification.

In the last chapter, chapter 6, the final conclusions will be presented and suggestions for future works will be formulated.

2. Basics Theoretical Concepts

The basic theoretical concepts covering all the themes related with magnetism and types of magnetization phenomena, particularly important for the synthesized nanoparticles, are described in this section. The knowledge about the physical characteristics of iron oxide nanoparticles and the drug delivery application focused on brain treatment is also gathered. Moreover, all basic principles associated with the characterization techniques used throughout the course of this work are also covered in this section.

2.1. Magnetism

Magnetism was first approached in ancient Greece (VI century BC) in a region called Magnesia, where the Greek philosopher Tales de Milo observed a strange behaviour of a certain stone. Those so called lodestones exhibited the property to interact with each other (attracting or repelling themselves) or attract materials such as iron. Simultaneous Greek and Chinese studies involving this naturally magnetized form of the mineral magnetite, and all the phenomena related to it, introduced the concept of magnetism; that knowledge led to the first application of a magnetism related invention, the magnetic compass [15].

Despite that antique empirical knowledge, theoretical magnetic phenomena were only systematically studied after the XVII century, when in 1600 William Gilbert, author of *De Magnete, Magneticisque Corporibus, et de Magno Magnete Tellure*, enunciated the fundamental properties of magnetism and discovered the Earth's magnetic field. In the XVII century, Charles-Augustin de Coulomb developed Magnetostatic laws, similar to the ones that governed the attraction and repulsion movements between electric quiescent charges. He postulated that a magnetic force between objects was directly proportional to some quantities that he called magnetization units, or magnetic pole intensities, and inversely proportional to the square of the distance between the objects.

Nowadays, there are multiple interesting studied effects involving magnetism in condensed matter systems, knowing that the atoms in these systems have magnetic moments and that these moments, somehow, interact with each other. In real systems there is a wide diversity of magnetic properties that can exist, and that can be explained by the variety of magnetic interactions, which are dependent on whether or not the magnetic moments can act together in a cooperative way [15].

2.1.1. Diamagnetic, paramagnetic and ferromagnetic materials

There is always a duality in materials due to their magnetic susceptibility and, concerning it, materials may be classified by their behaviour to externally applied magnetic fields as diamagnetic, paramagnetic, or ferromagnetic. That duality is explained by the opposition (diamagnetic material) or alignment (paramagnetic material) of the induced magnetic momentum with the applied magnetic field which caused it [15].

Since diamagnetism is an inherent property of all materials, there is a balance between diamagnetic and paramagnetic effects and, depending on which effect overcomes the other, those materials are classified as diamagnetic or paramagnetic.

When there is no applied magnetic field to a paramagnetic material, its magnetic momentum points in random directions because there are weak interactions between neighbouring atoms. The magnetization of a paramagnetic material directly depends on the intensity of the applied magnetic field, and inversely depends on the temperature of the material as shown by the Curie's law:

$$M = C \times \frac{B}{T} \quad , \tag{1}$$

where *M* is the magnetization, *B* is the magnetic field, *C* is the constant of Curie and *T* is the temperature of the material, in Kelvin. Consequently, an increase of the applied magnetic field will align the spins whereas an increase of temperature will randomize them [15].

Ferromagnetic materials exhibit a long-range ordering phenomenon at the atomic level, which causes the unpaired electron spins to line up parallel with each other in a region called a domain. Within the domain, the magnetic field is intense, but in a bulk sample the material will usually be unmagnetized because the many domains will themselves be randomly oriented with respect to one another. Ferromagnetism manifests itself in the fact that a small externally imposed magnetic field can cause the magnetic domains to align with each other and the material is said to be magnetized. The driving magnetic field will then be increased by a large factor which is usually expressed as a relative permeability for the material. These materials will tend to stay magnetized to some extent after being subjected to an external magnetic field. This tendency to "remember their magnetic history" is called hysteresis [15].

A commonly used magnetic quantification that differentiates these type of materials is their bulk magnetic susceptibility, which specifies how much the relative permeability differs from one. The bulk magnetic susceptibility is expressed by:

$$\chi_m = k_m - 1, \tag{2}$$

where k_m is the relative permeability. For paramagnetic and diamagnetic materials the relative permeability is very close to 1 and the magnetic susceptibility very close to zero ($\approx$-10^{-5} and $\approx 10^{-5}$-10^{-3}, respectively). For ferromagnetic materials, this quantity may be very large ($\approx$50-10^4) and they will undergo a small mechanical change when magnetic fields are applied, either expanding or contracting slightly [16].

2.1.2. Ferrimagnetic materials

Ferrimagnetism is a type of permanent magnetism that occurs in solids in which the magnetic fields associated with individual atoms spontaneously align themselves, some parallel, or in the same direction (as in ferromagnetism), and others generally antiparallel, or paired off in opposite directions (as in antiferromagnetism). Ferrimagnetism occurs mainly in magnetic oxides known as ferrites. The natural magnetism exhibited by lodestones, recorded as early as the 6th century AC, is that of a ferrite, the mineral magnetite, a compound containing negative oxygen ions O^{2-} and positive iron ions in two states, iron(II) ions, Fe^{2+}, and iron(III) ions, Fe^{3+}. The magnetic behaviour of the two sublattices that make the crystallographic arrangement is the explanation for this magnetic phenomenon. When the magnetization of the sublattices is not equal and opposite, then they cannot cancel each other, resulting in a net magnetization of the material. Due to the different molecular field in each sublattice, they have a distinguish temperature dependence, which means that one of the sublattices can dominate the magnetization at a higher temperature while the other dominates at a lower one. When this occurs, the net magnetization will be decreased to zero and changes sign at a temperature identified as the compensation temperature [15].

2.1.3. Superparamagnetic materials

Superparamagnetism is a phenomenon related to the decrease in size of materials and leads to delicate and ultimately valuable modifications in their magnetic behaviour. When the particle size is reduced below a specific critical size, the material changes its behaviour from a multi-domain system to a single-domain one. This behaviour modification occurs if the cost of domain wall formation is not compensated by savings in demagnetizing energy, causing a single-domain particle constrained to lie parallel or anti-parallel to the direction of the applied magnetic field [15].

Assuming that each particle in a non-magnetic matrix is sufficiently far apart so that no interparticle interaction exists, then this system will behave similar to a paramagnetic one differing in each independent moment; there is then a large group of moments instead of longer atomic one, as was before. Each of those large groups is inside each and every particle of the system and that is what is known as a superparamagnetic system [15].

When working with nanoparticles, a uniaxial magnetic anisotropy is considered where the magnetic anisotropy energy is expressed by:

$$E(\theta) = kV\,(\sin\theta)^2, \tag{3}$$

being k the magnetic anisotropy constant, V the particle volume and θ is the angle between the magnetization direction and the easy direction of magnetization. The previous equation shows that the magnetic anisotropy energy has two minima at θ=0° and θ=180°, separated by an energy barrier kV. The phenomenon called superparamagnetic relaxation can be described as the spontaneous fluctuations of magnetic nanoparticle's magnetization direction between the easy directions corresponding to the two minima, which are a consequence of an energy barrier smaller than or comparable to the thermal energy.

2.2. Iron oxides

Iron oxides are common compounds which are abundant in nature and readily synthesized in laboratory. They are present in all of the different compartments of the global system: atmosphere, pedosphere, biosphere, hydrosphere and lithosphere. The logical consequence of this widespread distribution of iron oxides is that many different scientific disciplines (such as Biology, Geology, Industrial Chemistry, Medicine, *etc.*) have an interest in them. Naturally this has led to a much fruitful, interdisciplinary communication and interaction [17].

There are sixteen iron oxide/hydroxide compounds distributed in oxides, hydroxides or oxyhydroxides. The iron oxides are composed of Fe together with O and/or OH but only six out of those sixteen have only iron and oxygen. Throughout the course of this work only two of those six will be more deeply discussed: magnetite and maghemite. To allow the distinction between these interchangeable iron oxides, some physicochemical properties are described and exhibited in Table 1 [17].

Table 1. Physicochemical properties of Magnetite (Fe_3O_4) and Maghemite (γ-Fe_2O_3)

Iron Oxide	Formula	Crystallographic structure	Lattice parameter – a (nm)	ρ (g.cm^{-3})	Curie Temperature (K)	Magnetization saturation at 300K (emu/g)
Magnetite (Black)	Fe_3O_4	Cubic	0.8396	5.18	850	92 - 100
Maghemite (Reddish-Brown)	γ-Fe_2O_3	Cubic or tetragonal	0.8347	4.87	820 - 986	60 - 80

2.2.1. Magnetite

Magnetite or lodestone, Fe_3O_4, is a black, ferromagnetic mineral containing both Fe^{II} and Fe^{III}. Together with titanomagnetite, it is responsible for the magnetic properties of rocks, which are objects of paleomagnetic studies. It has an inverse spinel structure as shown in Figure 1 but, below Verwey transition temperature (T_v = 120 K), the species of Fe^{2+} and Fe^{3+} arrange themselves in a regular pattern, turning into a normal spinel structure [17].

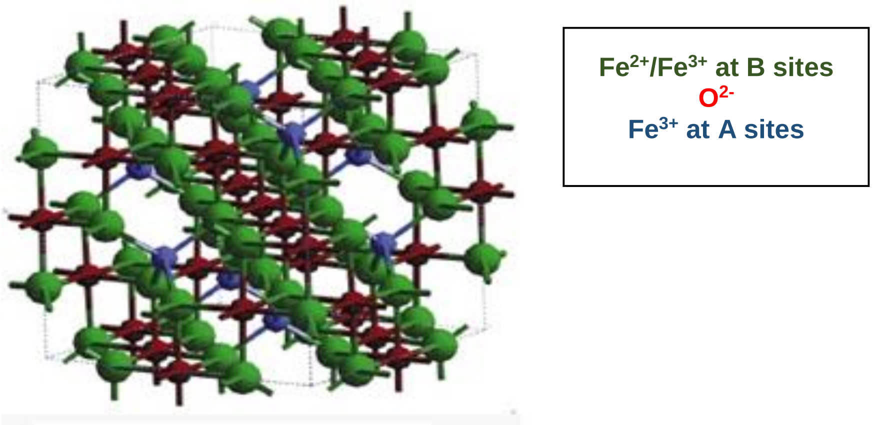

Figure 1. Crystallographic structure of magnetite (inverse spinel).

In order to determine the details of its structure, magnetite was one of the first mineral structure to which X-ray diffraction was applied by Bragg in 1915. It is defined as having a face-centred cubic unit cell on an inverse spinel structure with a unit cell edge length of 0.8396 nm.

Due to divalent (Fe^{2+}) and trivalent (Fe^{3+}) iron atoms present in magnetite, the two main crystal sites are occupied in different ways. While tetrahedral sites or A sites are occupied with Fe^{3+}, the octahedral ones or B sites are distributed between Fe^{2+} and Fe^{3+}. The good electrical conductivity presented by this iron oxide is explained by the crystallographic spatial changes of Fe^{2+} and Fe^{3+} ions, along the close packed structure. Those cation substitutions are accompanied by changes in the unit cell edge length. Since magnetite can be slightly metal deficient on Fe^{3+} octahedral sites, causing vacancies, its stoichiometric Fe^{2+}/Fe^{3+} ratio of 0.5 is often not attained [17].

Two interpenetrating magnetic sublattices with antiparallel spins are formed by the two cation sites in the structure - A and B sites, in which the spin direction is equal but its magnetic extents are not. In condensed macro systems, at room temperature, this results in a ferrimagnetic effect that is modified into a superparamagnetic behaviour when magnetite particles have a size below a constant critical and nanometric size: 25-30 nm [17].

At atmospheric O_2 pressure, magnetite is thermodynamically unstable due to its mixed valence. That fact makes magnetite much more susceptible to oxidation which is related with an incessant decrease of Fe^{2+} levels in its composition and a consequent cell edge change, although the crystal size and morphology remain constant [18].

2.2.2. Maghemite

Maghemite (γ-Fe_2O_3) is a reddish-brown ferrimagnetic iron oxide and is the second most stable polymorph of iron oxide. It occurs naturally in soils as a weathering product of magnetite (Fe_3O_4), to which it is structurally related [17].

Both maghemite and magnetite exhibit a spinel crystal structure, but while the latter contains both Fe^{2+} and Fe^{3+} cations in octahedral sites, in maghemite all the iron cations are in trivalent state, and the charge neutrality of the cell is guaranteed by the presence of cation vacancies in those sites, where in magnetite a divalent iron state atom exists. Maghemite can have different symmetries depending on the degree of ordering of those vacancies and its structure can be obtained by creating 8/3 vacancies out of the 24 Fe sites in the cubic unit cell of magnetite. That's the reason why maghemite has a cubic unit cell value of 0.83474 nm, which is slightly below the unit cell value for magnetite [18].

The presence of vacant sites in maghemite makes its magnetic structure composed by one sublattice in tetrahedral sites and another in the octahedral sites. The spin sublattices orientations are both antiparallel with a difference of magnitude between each other, resulting in ferromagnetic behaviour at room temperature. When maghemite particles have a size below 10 nm, the magnetic system behaves superparamagnetically [17].

2.3. Synthesis of magnetic nanoparticles

Two types of methods are described in the literature for synthesis of magnetic nanoparticles, physical and chemical ones. Physical methods such as gas-phase deposition and electron beam lithography are elaborated procedures incapable of controlling particle size in nanometric scale. Unlike these physical procedures, the chemical ones are known to produce highly stable, high-quality, monodispersive and shape and size-controlled nanoparticles [19]. In fact, in 2011, Mahmoudi *et al.* proved that 90% of magnetic nanoparticles are synthesized using chemical procedures [20]. The following table presents and compares the chemical procedures more often used in the synthesis of magnetic nanoparticles.

Table 2. Comparison between different chemical methods for synthesis of magnetic nanoparticles [4].

Method	**Thermal decomposition**	**Hydrothermal synthesis**	**Co-precipitation**	**Microemulsion**
Synthesis	Complex, inert atmosphere	Simple, high pressure	Very simple, ambient conditions	Complex, inert atmosphere
Reaction temp. (°C)	100 - 320	220	20 – 90	20 - 50
Reaction period	Hours-days	Hours-days	Minutes	Hours
Solvent	Organic	Water-ethanol	Water	Organic
Size distribution	Very narrow	Very narrow	Narrow	Narrow
Shape Control	Very good	Very good	Poor	Very Good
Yield	High scalable	Medium	High scalable	Low

Although thermal decomposition involves complex processes and requires higher temperatures and a longer reaction period, a very narrow size distribution can be obtained, a very good shape control of nanoparticles, and a high and scalable yield can be achieved (see Table 2). Those aspects fit perfectly on the requirements of our work. As result of that, thermal decomposition was the nanoparticle synthesis route used throughout the course of this work, and the principle basics involved in this type of synthesis will be next described.

2.3.1. Thermal decomposition

Thermal decomposition is a very promising synthesis method that allows obtaining of mono-dispersive and high-quality magnetic nanoparticles, which is highly desirable when trying to control their physicochemical properties [21].

There are several important aspects in this synthesis method that influence the control of the size and morphology of the obtained magnetic nanoparticles such as the ratio between reagents, the reaction temperature and time, as well as the posterior aging period [4].

This method involves the thermal decomposition of organometallic compounds in high-temperature boiling solvents containing stabilizing surfactants. The most often used organometallic precursors are acetylacetonates, being oleylamine, oleic acid and fatty acids the most conventional surfactants [4]. Nanoparticles formed by this method follow a sol formation mechanism known as nucleation process, where the initial number of particles and its subsequent growth is crucial [22].

From the formation of the new solid phase energy is released, which is thermodynamically balanced with the energy needed to form the surface of small nuclei in this same phase. Therefore, the surface free energies are responsible for the growth of colloidal particles. Exchange of molecules amongst the particles will happen so that equilibrium with the solution surrounding them can be achieved. Above a critical size, clusters tend to grow and if the dispersion contains particles with multiple sizes, a diffusional flow of solutes will occur from the smaller particles to the largest [22].

Nucleation and growth processes from a supersaturated system can be described using a model implemented by La Mer. When the reaction begins, the dissolved solute increases at a stabilized rate, until the critical supersaturation point of concentration is achieved. At this stage, nucleation starts to occur. Eventually, nucleation will cause a decrease in concentration; at that point particle growth is substituted by particle nucleation and the concentration will continue to decline, due to growth mediated by diffusion, until it reaches an equilibrium solubility value [22].

It is important to clarify that if more nuclei are formed at the beginning of the process, the obtained nanoparticles will be smaller because the same amount of mass is going to be distributed by more nucleation centres [22].

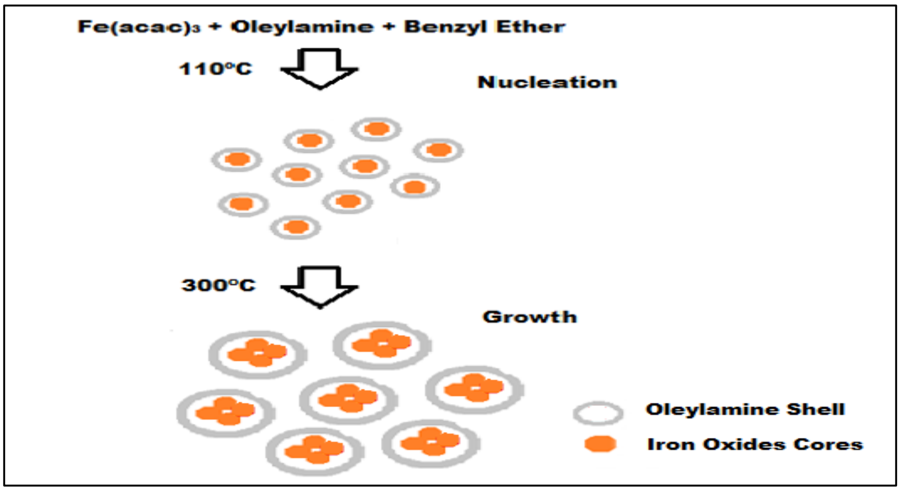

Figure 2. Different phases of the reaction - details for the system under study.

Figure 2 exemplifies the different stages previously explained when applied to the specific reaction synthesis to be used in this work. The nucleation process is guaranteed when an 110°C threshold is established and the subsequent growth of nanocrystallites is obtained at a higher threshold of 300°C. When this threshold is obtained, a nanostructured iron oxide composed by magnetite/maghemite nanoparticles starts to form through the aggregation of the nucleation cores.

2.4. SPIONs in drug delivery systems

Most of SPIONs applied in drug delivery consist of nanoparticles, nanospheres, liposomes and microspheres. In these systems, the drugs are bound to the surface of SPIONs (especially for nanoparticles) or encapsulated in magnetic liposomes and microspheres. The recent applications of SPIONs in diagnosis and therapy are presented in Figure 3.

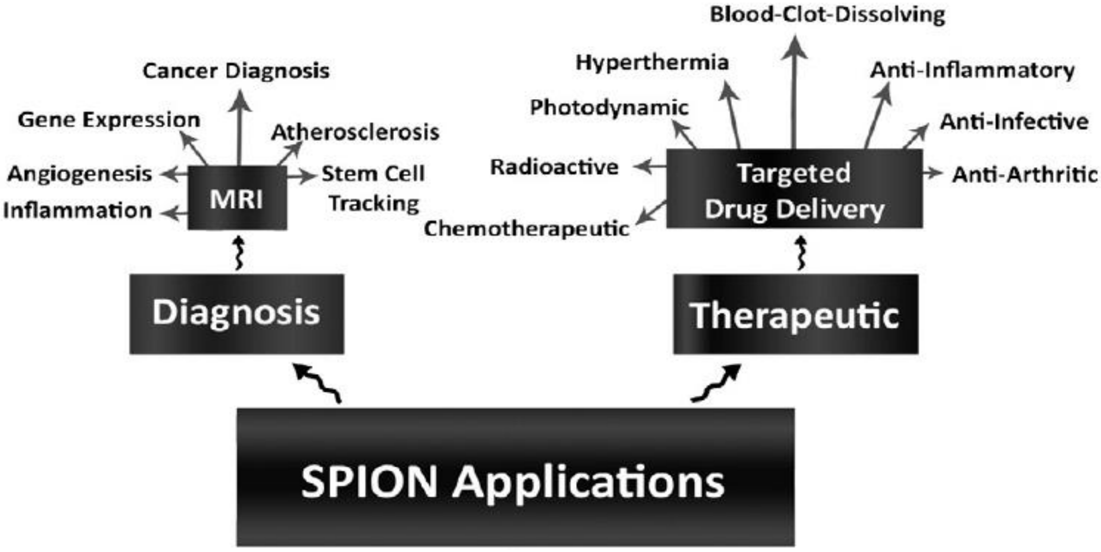

Figure 3. Diagnostic and therapeutic applications of SPIONs.

In order to minimise the side effects and the required dosage of the drugs, the surface engineered SPIONs (*e.g.* with targeting ligand/molecules attached to their surfaces) are used together with an external magnetic field so that the particles can be taken to the proper drug release site [23].

With the aim of obtaining the desired drug delivery system, with uniform biophysicochemical properties, a very narrow size distribution of the SPIONs coupled with superparamagnetic properties should be considered.

The magnetic properties are strongly associated to impurity content, structural imperfections of the particles or the composition of their protective shell. The concentration of SPIONs in solutions is also a crucial factor affecting magnetic properties. When the concentration of magnetic nanoparticles is increased, a clustering of the particles may occur, leading to magnetic interactions and to a subsequent significant effect on the net magnetization.

In addition to the superparamagnetic properties that SPIONs must exhibit, careful consideration should also be given to SPIONs with different sizes and shapes, due to their different behaviour along distinct fluid environments. During the movement through the systemic circulation, the SPIONs will suffer the effect of a viscous force rather than an inertial force [24].

The stabilisation of SPIONs in a biological suspension is a critical matter in order to improve their function as drug carriers. The changes in the isoelectric point of SPIONs (due to the type of coating used), their size distribution, shape, surface characteristics, concentration and volume, as well as reversibility and strength of the drug-nanofluid bond, access to the organism, rate of the injection, duration of magnetic field application and geometry and strength of the magnetic field, are crucial parameters that affect the colloidal stability of drug-loaded SPIONs [25].

2.4.1. Limitations of SPIONs for drug delivery

- Restriction and progress in magnets

The major limitation of SPIONs for drug delivery applications is the inadequate magnetic gradient (due to the distance between magnet and targeted site) in order to control the residence time of nanoparticles at the targeted site. Preliminary investigations of the hydrodynamics of drug targeting suggest that for most magnetite-based carriers, flux densities at the target site must be of the order of 0.2 T with field gradients of approximately 8 T m^{-1} for femoral arteries and greater than 100 T m^{-1} for carotid arteries [26]. This suggests that targeting is likely to be most effective in regions of slower blood flow, particularly if the target site is closer to the magnet source. Two-dimensional computational simulations of magnetic particle motion in the carotid artery have been performed [27]. They showed that it was not possible to obtain a maximum magnetic force on a magnetic particle inside the body using an externally applied magnetic field. Since drug targeting is affected by pulling magnetic particles to the edge of blood vessels, this suggests that it will not be possible to target interior regions of the body without strongly targeting some of the surrounding regions. Thus, the use of magnetically targeted drug delivery carriers with an externally applied field is appropriate only for targets close to the surface of the body.

- Brain delivery

Results have confirmed the low efficiency of SPIONs for brain targeted imaging and drug delivery applications, due to their restrictions in crossing the blood-brain barrier (BBB) [28]. The BBB, which has the role of isolate the brain tissue with special endothelial cells, has the potential to inhibit the entrance of therapeutic compounds (*e.g.* for treatment of neurological or psychiatric disorders) to the brain [29]. One alternative is the direct injection of SPIONs to the desired part of the brain tissue by disruption of the BBB; however, this method may cause unpredictable and high risks for patients. In one study, SPIONs with a size of 10–20 nm were taken up by the blood tumour barrier and their ability to target rat glioma tumours was analysed [30]. It is worth noting that a magnetic field of 0.6 T was applied to the brain in order to increase the targeting efficiency. After specific times, the rats were sacrificed and the brain tissue was analysed for iron contents. The results confirmed significant differences between the SPIONs-targeted tumour tissues and normal ones *(i.e.* a 2–21 fold increase in concentration for 0.5 and 6h after injection of SPIONs, respectively) with a low total concentration of SPIONs in normal brain tissue.

2.5. Nanoparticles characterization techniques

2.5.1. X-Ray Diffraction (XRD)

XRD has a good potential for the analysis of nanoparticles, due to yield information about the substructure of the materials (sizes of crystallites, microstrain of a lattice, dislocation structures, etc.). Since it is based on the long range order of the atoms, X-ray diffraction is also one of the most reliable characterization techniques used to identify iron oxides crystalline phases.

The operating basis is related to electromagnetic radiation (X-ray) interacting with the atoms of the sample to be analysed. Depending on how the X-ray beam interacts with the crystal planes of the solid, the crystal lattice composed by those atoms diffracts X-ray in various directions, which results in distinct diffraction patterns or diffractograms [31]. These diffraction patterns work as a very specific crystallographic print that should be compared and matched with reference ones from existing databases [17].

Depending on the X-ray source and positioning of the electromagnetic beam, the X-ray that interacts with the sample has its characteristic wavelength (λ) and hits the sample with an oriented angle of incidence (θ). When an X-ray beam hits an atom, the electrons around the atom start to oscillate with the same frequency as the incoming beam. In almost all directions, destructive interference will take place, as result of the combining waves being out of phase, and there is no resultant energy leaving the solid sample. However, the atoms in a crystal are arranged in a regular pattern and, in a very few values of θ, constructive interference will occur with the defined sets of parallel planes of the crystal, with interplanar spacing (d) enhancing the intensity of the diffracted radiation. Bragg's equation correlates all these parameters:

$$n\lambda = 2d_{hkl}\sin\theta \tag{4}$$

where n is an integer indicating the order of diffraction and d_{hkl} is the lattice spacing of the plane family (hkl) of the sample [31]. Since each crystalline phase has its characteristic set of interplanar spacing and intensities, it's possible to identify the phase of the sample under study [17]. The ultimate condition for Bragg's law application is that the incident beam and the diffracted beam should be symmetric in relation to the normal of the diffracting surface, as shown in Figure 4.

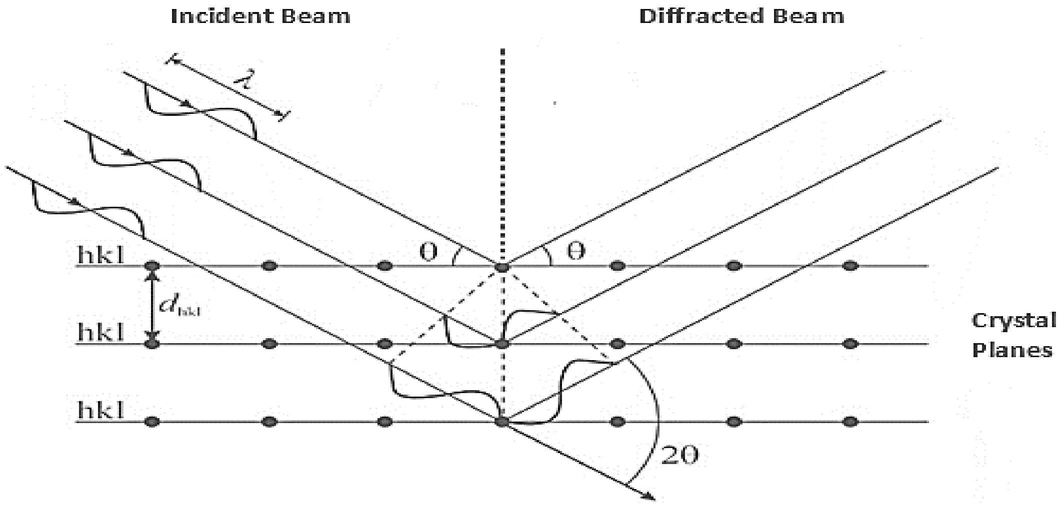

Figure 4. Schematic representation of X-ray diffraction phenomenon (Bragg's Law).

The intensities of the obtained diffracted radiation for 2θ angles appear in diffractograms as diffraction peaks and they are related to the diffraction of the incident beam by a set of crystal planes with the same interplanar spacing, each one identified by their own Miller indices *hkl*. Each peak is characterized by 3 significant features: position, intensity and shape [31].

In a brief description, the position is related to the medium value of d_{hkl}, depending on the unit cell parameters, while the integrated intensity is proportional to the number of crystallites in the cited conditions for Bragg's diffraction, and influenced by the orientation of coherent domains of diffraction. On the other hand, the shape of the diffraction peaks is related to the dimension and deformation of each coherent domain.

The Full Width at Half Maximum (FWHM) of a diffraction peak is another parameter to consider and results from a convolution of three distinct effects: the size of crystallites, the instrumental resolution and the degree of strain. The average size of crystallites (*D*) is determined using the Scherrer formula:

$$\beta = \frac{\varepsilon\lambda}{D\cos\theta} \quad , \tag{5}$$

where β is the FWHM of the peak in terms of 2θ and measured in radians, ε is a form factor of the crystallites, usually with an approximated value of 0.9 and λ is the wavelength of the incident X-ray beam. The FWHM due to instrumental resolution can be neglected within a nanomaterial analysis. Also the degree of strain related with displacements, imperfections and internal tensions in the crystal lattice, usually observed when the peaks are dislocated or extended, can be disregarded in this case since we used a chemical method to synthesize nanoparticles.

A diffractogram obtained with monochromatic radiation of a known wavelength has all the information to obtain the lattice parameter of the crystal, calculated by the quadratic formulae corresponding to the crystalline systems [31].

2.5.2. Transmission Electron Microscopy (TEM)

Transmission Electron Microscopy (TEM) is a vital characterization tool for directly imaging nanomaterials to obtain quantitative measures of particle and/or grain size, size distribution, and morphology.

The TEM operates on the same basic principles as the light microscope, but uses an electron beam interacting with the sample instead of light, and it is much more complex. Their transmission mode imposes a "transparency" of the sample to the electrons, thus the maximum thickness at the borders should be about 100 nm [32].

In such instruments, the gun chamber generates a beam of high energy electrons which are accelerated by changing the electrical potential difference in the range 40 to 400 kV. Then, this beam is collimated by magnetic lenses and allowed to overpass the sample under high vacuum. The obtained transmitted beam and several diffracted beams generate the image and also a diffraction pattern, which are displayed on a fluorescent screen located under the sample. The lattice spaces of the crystalline structure can be obtained from the diffraction pattern [32]. The several layers of components inside a TEM are shown in Figure 5.

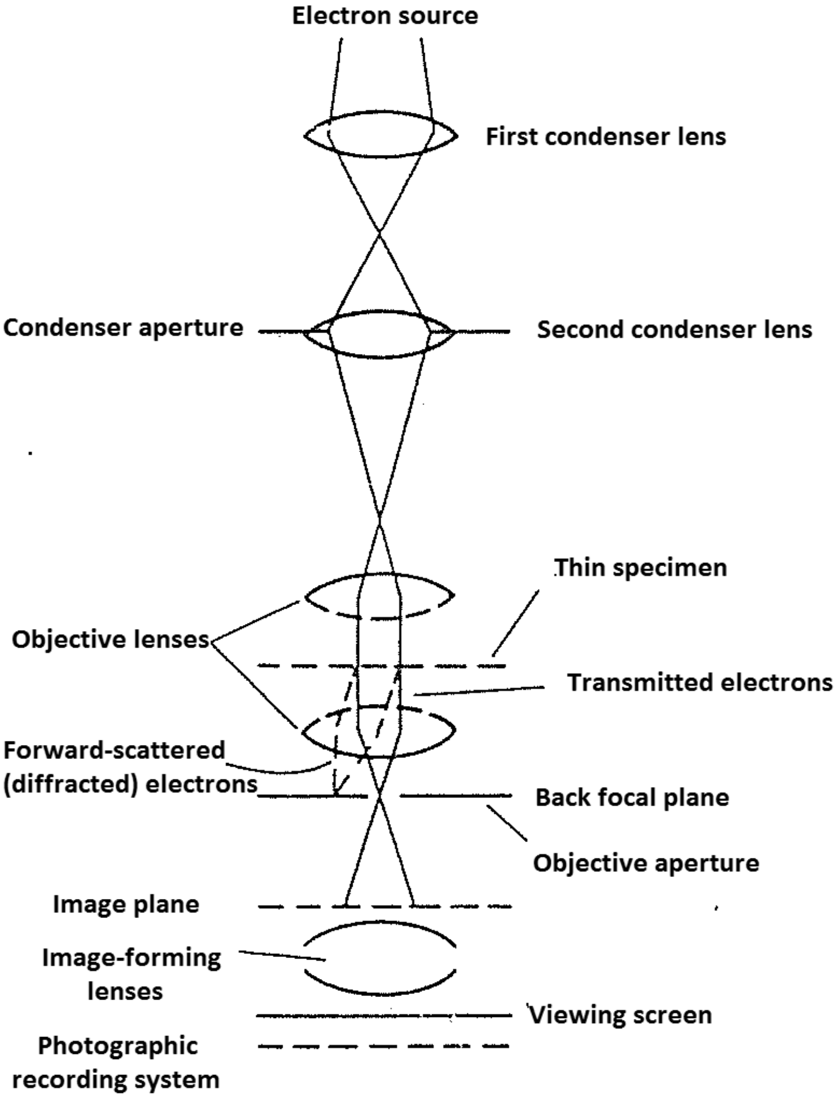

Figure 5. Schematic representation of the basic principle and components involved in TEM.

Sensors such as EELS (Electron Energy Loss Spectrometer) and EDS (Energy Dispersive X-ray Spectrometer) can be coupled to TEM, enabling chemical analysis of the sample and making this characterization technique go further than just outputting a high resolution magnified image of a sample [32].

2.5.3. Dynamic Light Scattering (DLS)

Dynamic light scattering (DLS) is a well-established technique used to determine the size and size distribution of molecules and particles suspended in a liquid, typically in the submicron region, with the latest technology measuring sizes lower than 1 nm. This technique is also called photon correlation spectroscopy (PCS) and quasi-elastic light scattering (QELS). The latter terms are more common in older literature.

The DLS technique measures the Brownian motion related to the size of the particles. Brownian motion designates the random movement of particles due to the bombardment of the solvent molecules that surround them. The larger the particle, the slower the Brownian motion will be [33].

The basic principle of DLS technique is based in Stokes-Einstein equation:

$$D_{\mathrm{h}} = \frac{k_{\mathrm{B}}T}{3\pi\eta D_t} \ , \tag{6}$$

where D_{h} is the hydrodynamic diameter to be determined, D_{t} the translational diffusion coefficient of the particles in the liquid, k_{B} the Boltzmann's constant, T is the absolute temperature and η is the viscosity of the liquid. The translational diffusion coefficient is found by dynamic light scattering and depends not only on the size of the particles "core", but also on any surface structure, as well as the concentration and type of ions in the medium [33].

In a DLS instrument, a laser beam is directed to the suspension and, when it interacts with particles, the light is scattered in several directions. The scattered light is a function of the hydrodynamic size and concentration of the sample and is detected on a photon detector connected to a correlator. The correlator compares the intensity of the scattered light in consecutive intervals of time and generates a correlation function [33]. The operation basis of DLS is shown in Figure 6.

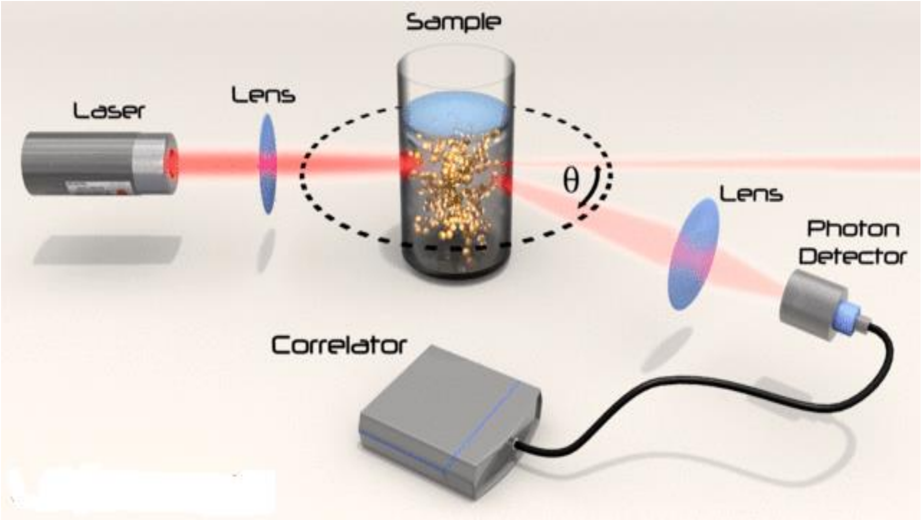

Figure 6. Schematic illustration of the optical configuration of a DLS instrument.

This hydrodynamic diameter corresponds to the diameter of a sphere that has the same translational diffusion coefficient as the particle, and it is obtained from the correlation function by using the cumulant method. By fitting a polynomial of third degree to the logarithm of the intensity correlation function, the decay rate Γ is obtained. The decay rate is directly related to the diffusion coefficient D_t:

$$\Gamma = q^2 D_t \quad , \tag{7}$$

where q is the wave vector, which is dependent of the scattering angle.

Particles of different sizes scatter with different intensities in correlation with the scattering angle. Thus, there is an optimum angle of detection for each particle size. A high quality analysis should always be performed at several scattering angles (multiangle DLS). This becomes even more important in case of polydisperse samples with unknown particle size distribution, since at certain angles the scattering intensity of some particles will completely overwhelm the weak scattering signal of other particles, thus making them invisible to the data analysis at this angle [33].

2.5.4. Fourier Transform InfraRed (FTIR) Spectroscopy

This characterization technique was applied to characterize the type of coat of Fe_3O_4 nanoparticles by identifying the chemical groups/bonds present in the synthesized samples.

The total internal energy of a molecule in a first approximation can be resolved into the sum of rotational, vibrational and electronic energy levels. Infrared spectroscopy is the study of interactions between matter and electromagnetic radiation (photons) in a wave number range of 400 to 4000 cm^{-1}. These interactions induce the excitation of the vibration or rotation of molecules to a higher energy state and they are normally related with stretching deformations of interatomic bonds and bending deformations of the interbond angles [17].

The probability of a particular beam of infrared light to be absorbed by the sample depends on the actual interaction between its frequency and the molecule. In general, a frequency will be strongly absorbed if its photon energy coincides with the vibrational/rotational energy levels and force constants associated with interatomic bonds of the molecule [17].

The FTIR spectrometer operates on a different principle called Fourier transform. The mathematical expression of Fourier transform can be expressed as:

$$F(w) = \int_{-\infty}^{+\infty} f(x) e^{iwx} dx \, , \tag{8}$$

where ω is angular frequency and x is the optical path difference. $F(\omega)$ is the spectrum and $f(x)$ is called the interferogram. It is clear that if the interferogram $f(x)$ is experimentally determined, the spectrum $F(\omega)$ can be obtained by using Fourier transform. The operation principle linked to the interferogram acquisition is represented in Figure 7 and it's based on the operation mode of a Michelson Interferometer.

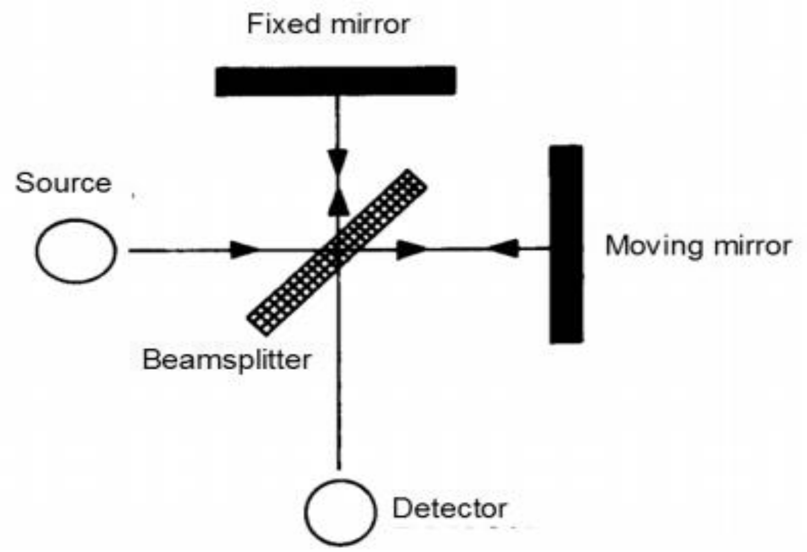

Figure 7. Schematic diagram of a Michelson Interferometer.

The light source produces a light beam that is directed to the beamsplitter. Half of the light is reflected and half is transmitted but then, both are reflected in two mirrors. The two beams reaching the detector come from the same source and have an optical path difference determined by the positions of the two mirrors, *i.e.* they have a fixed phase difference. Therefore the two beams interfere constructively or destructively for a particular frequency depending on the positioning of the moving mirror. Due to the movement of this mirror, a sinusoidal signal (interferogram) will be detected with the same frequency as this movement occurs. Fourier transform is then computationally applied and a spectrum with the percentage of radiation absorbed/transmitted versus the wavenumber frequency of the incident radiation is obtained [34].

The differences in the chemical structure (bonds) of materials gives rise to unique infrared spectra for each material, making possible the identification of substances present in the sample.

2.5.5. Thermal Analysis

Thermal analysis is a branch of materials science characterization methods that measure with high precision distinct properties of the sample (weight, volume, temperature, *etc.*) when this is subjected to heating with a programed profile (usually at a constant rate between 2 and 10°C.min^{-1}). In order to characterize iron oxides, two main thermal analysis methods are commonly used: thermogravimetric analysis (TGA) and differential scanning calorimetry (DSC) [17].

TGA is a method of thermal analysis that precisely measures the weight of the sample as a function of increasing temperature (with constant heating rate), or as a function of time (with constant temperature and/or constant mass loss) [35]. Therefore, the basic instrumental requirements for TGA are a precise scale with a pan loaded with the sample, and a programmable furnace (Figure 8). As the temperature increases, the various components of the sample are volatilized/decomposed and the percentage of weight loss for each one can be measured. The first derivative is often also plotted to determine points of inflection for more in-depth interpretations and framing of the phenomena.

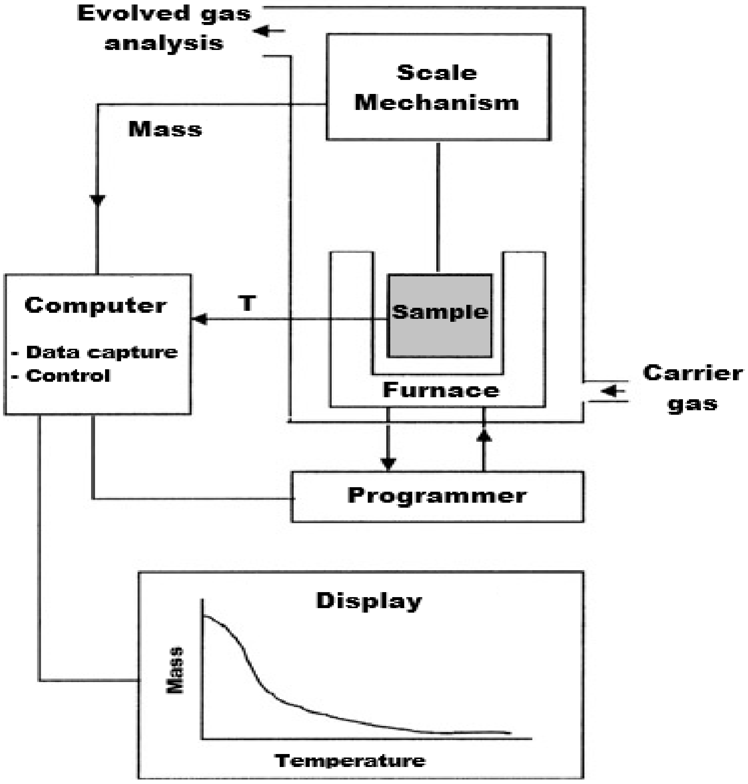

Figure 8. Schematic arrangement of a TGA equipment.

In DSC, an accurate measurement of the exchanged heat flow is made, as a function of temperature or time. With this thermoanalysis technique is possible to determine endothermic and exothermic events in the sample from the obtained peaks. These peaks are normally representative of phase changes in the sample or undergoing reactions [36]. For magnetite, thermograms show a first exothermic peak involving a phase transformation from magnetite (Fe_3O_4) to maghemite (γ-Fe_2O_3) – at 225 ^{0}C - and a second one (also exothermic) demonstrative of maghemite to hematite (α-Fe_2O_3) phase transformation – at 590 ^{0}C.

In both methods, the experiments can be conducted in various atmospheric conditions, *e.g.*, vacuum, inert, oxidative or reactive.

2.5.6. Vibrating Sample Magnetometer

A vibrating sample magnetometer (VSM) is a scientific instrument that measures magnetic properties of the materials such as the type, strength and direction of the remnant magnetization of magnetic materials. The creator of this characterization instrument was Simon Foner, in 1955, and despite of several possible detection-coil configurations existing nowadays, all of them (older and new) follow Faraday's Law of Induction. This law states that an electromagnetic field is generated when a change in flux linking the coil is induced.

Thus, a coil with *n* turns of cross sectional area *a* can generate a electromotive force *V* described as:

$$V = -na\frac{\mathrm{d}B}{\mathrm{d}t} \tag{9}$$

being *B* the magnetic flux density.

When the coil is positioned in a constant magnetic field, H:

$$B = \mu_0 H \tag{10}$$

where μ_0 is the vacuum permeability constant ($4\pi \times 10^{-7}$ N.A^{-2}).

If the sample with a magnetization *M* is introduced into the coil:

$$B = \mu_0(H + M) \tag{11}$$

The flux changes can now be expressed by:

$$\Delta B = \mu_0 M \tag{12}$$

Combining the previous equations (10) and (13):

$$Vdt = -na\mu_0 M \tag{13}$$

From these equations, it can be concluded that the output signal of the coil is proportional to the magnetization of the sample (*M*) but independent of the magnetic

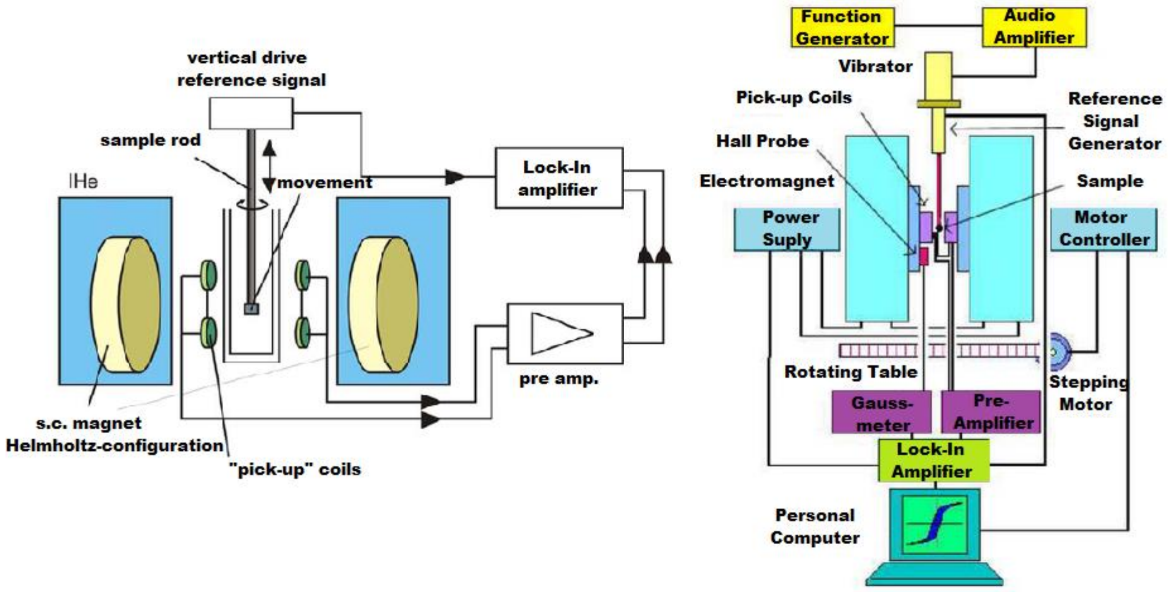

Figure 9. Schematic configuration of VSM equipment [38].

field applied to it (*H*) [37]. The fundamental schematic configuration of a VSM equipment is represented in Figure 9.

The operation mode involves a rod, where, in the nonmagnetic tip, a small sample is attached, and the other end is fixed to a linear motor, which makes the sample oscillate according to a desired frequency. This movement induces an electromagnetic field in the detection coil.

Because of the small alternated electromagnetic field, it is required the use of a look-in amplifier with high sensitivity only at the frequency of vibration. It is important to highlight that this amplifier must be provided with a reference signal originated from a sensor coupled to the driving system, which makes the sample oscillate.

When performing this analysis, the preparation of the sample must be done as clean as possible, because any amount of contaminating material can saturate the measurement of small amounts of magnetic materials. Other important aspect is the required calibration of the equipment, made with a specimen of known magnetic moment. This should have the same size and similar shape to the samples to be measured.

Since magnetite and maghemite have higher magnetic susceptibility (χ) than any other iron oxides, their presence will dominate the magnetization characteristics [16]. Due to the versatility and sensitivity of VSM, it is used either for weakly or strongly magnetic materials [38].

2.5.7. Mössbauer Spectroscopy

Mössbauer spectroscopy is a versatile technique used to study the nuclear structure of elements with the absorption and re-emission of gamma rays. This radiation is the most energetic of the electromagnetic spectrum. The technique uses a combination of the Mössbauer effect and Doppler shifts to probe the hyperfine transitions between the excited and ground states of the nucleus.

The phenomenon of resonant absorption of gamma rays, without recoil of the nucleus (also known as Mössbauer effect), only occurs in solid-state when the nucleus of the element is rigidly fixed in the crystal lattice. Only a certain number of elements exhibit Mössbauer characteristics, e.g. Fe, Ni, Zn, *etc.* The most commonly used isotope for iron is ^{57}Fe. It is a non-destructive and reliable technique, offering high resolution of charge state, ordering temperature and magnetic moment direction [39].

In order to study Fe atoms, the application of this method of spectroscopy consists on a source with ^{57}Co nuclei which decay by electron capture to an excited state of ^{57}Fe and, then, to a ground state of ^{57}Fe emitting the desired gamma-ray in the process. If the radiation is absorbed resonantly, the emitted gamma-ray can excite a transition in the sample being studied [15]. That interaction is then recorded by the computer as a point. When data acquisition finishes, a lorentzian approximation is performed to the scattered data, obtaining a Mossbauer spectra. In Figure 10, it is demonstrated how this method can be applied to obtain a Mössbauer spectra.

In transmission geometry, a plot of relative absorption against the velocity of the source, having the absorber in a fixed position, is obtained from a Mössbauer measurement. Doppler effect is implied in this movement of the source, with the aim of varying the energy emitted by the Mössbauer gamma-ray (14.44 keV for ^{57}Fe).

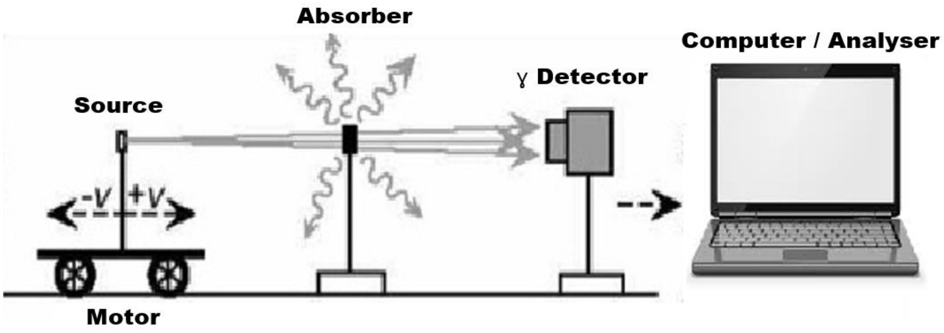

Figure 10. Experimental assembly representation of Mössbauer spectroscopy in transmission geometry.

There are 3 types of interactions between the emitted gamma-rays and the samples being studied: isomer shift, quadrupole splitting and hyperfine magnetic field. Depending on the nature of the sample to be studied, some interactions are more evident than others. At the origin of each hyperfine interaction there is a coupling between resonant nuclei and the electrons surrounding them [39]. The parameters obtained in the fitting of spectra are the hyperfine parameters, as it is described and illustrated in Table 3.

Table 3. Description and illustration of hyperfine interactions that occur in Mössbauer spectroscopy [17].

Name	Description
Isomer shift (δ)	Shift in the resonance energy of the transition produced by an energy difference in the s-electron environment between the source and absorber. Depending on the s-electron density, this shift is positive or negative.
Quadrupole splitting (ΔE_Q)	Interaction between the nuclear quadrupolar moment and an electric field gradient at the nucleus causes splitting of energy levels.
Hyperfine magnetic field (H)	Interaction of the dipole moment of the nucleus and the hyperfine magnetic field causes splitting of the nuclear energy levels.
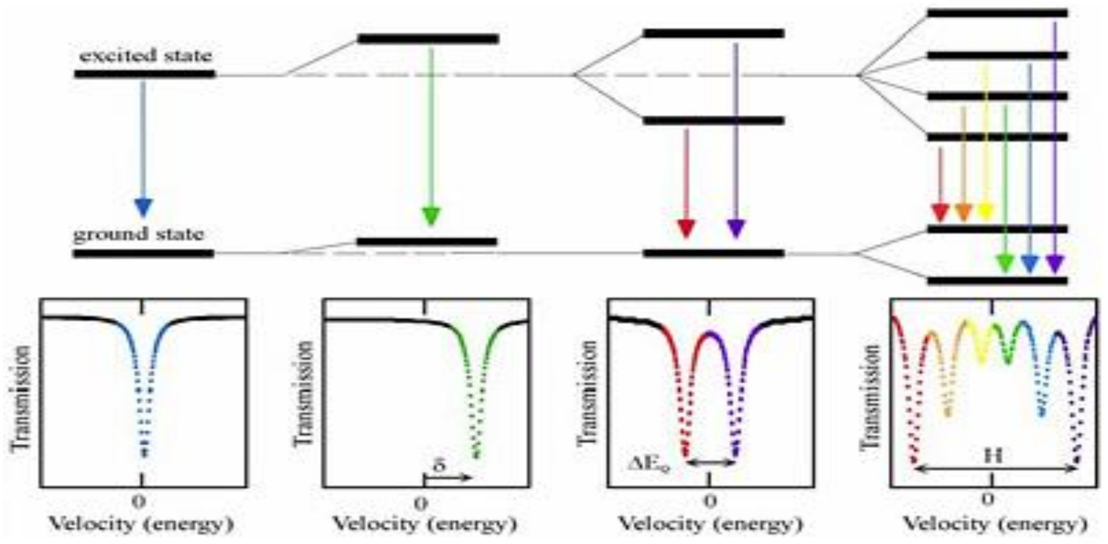	

The number of peaks obtained in a Mössbauer spectrum is related to the solid state transitions allowed between the ground state ^{57}Fe, and its excited state ^{57}Fe*. Depending on the crystal arrangement of the sample, several absorption lines as function of source velocity can be observed. The central position of each line is given relatively to an arbitrary origin, which is frequently the centre of the spectrum and corresponds to a sample of metallic iron measured at room temperature.

The magnetic properties of nanoparticles may differ from those of bulk materials, so when the size of the grains is too small, as it is expected for nanoparticles, the superparamagnetic character (relaxation effect of the magnetic state) of iron is shown by the presence of a single line centred near zero nm s^{-1}. The most dramatic effect of a small particle size is the fluctuation of the magnetization direction, instead of being stable.

Due to the exponential dependence of the relaxation time on the energy barrier, kV, the distribution of sizes shown by a sample of magnetic nanoparticles results in a very broad distribution of relaxation times, and Mössbauer spectra may have sextets and doublets or singlets. Frequently, the broad components due to particles with same size have low relative area and they are barely visible in the spectra. The temperature dependence of the relaxation times implies a variation of the area ratio of the sextets and doublets or singlets with the temperature.

The study of samples with a broad distribution of relaxation times, in Mössbauer spectroscopy, shows that the average blocking temperature is often defined as the temperature where half of spectrum is in a sextet and half of it is in a doublet or in a singlet form [39].

2.5.8. Zeta Potential

The development of a net charge at the particle surface affects the distribution of ions in the surrounding interfacial region, resulting in an increased concentration of counter ions (ions of opposite charge to that of the particle) close to the surface. Thus, an electrical double layer exists around each particle. As it is shown in Figure 11, the liquid layer surrounding the particle exists as two parts: an inner region, called the Stern layer, where the ions are strongly bound, and an outer, diffuse, region where they are less firmly attached. Within the diffuse layer there is a notional boundary inside which the ions and particles form a stable entity. This boundary is called the surface of hydrodynamic shear or slipping plane and the potential that exists at this boundary is known as the Zeta potential [40].

The Zeta potential equipment calculates this propriety of particles by determining the electrophoretic mobility and then applying the Henry equation. The electrophoretic mobility is obtained by performing an electrophoresis experiment on the sample and measuring the velocity of the particles using Laser Doppler Velocimetry (LDV). The Henry equation connects this features and is expressed by:

$$U_{\mathrm{E}} = \frac{2\,\varepsilon\, z\, f(ka)}{3\eta}\ , \tag{14}$$

where U_{E} is the electrophoretic mobility, z the zeta potential, ε the dielectric constant, η the viscosity, and $f(ka)$ is the Henry's function that, for small particles, takes an approximate value of 1,0 [41].

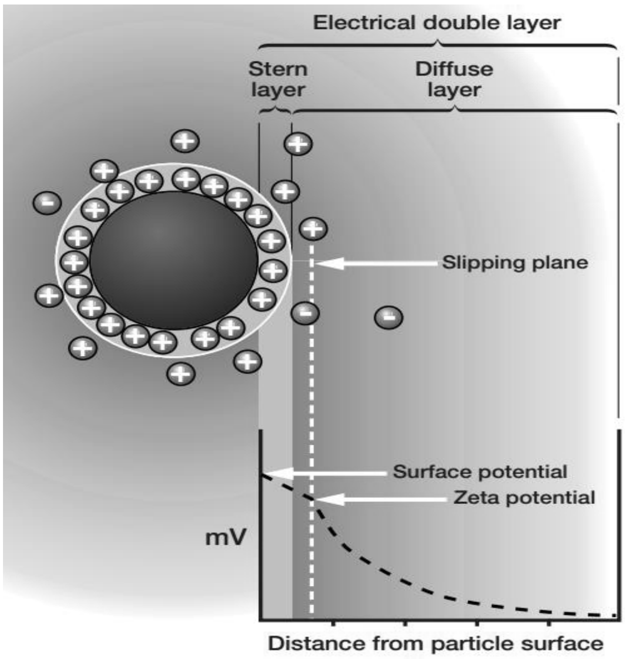

Figure 11. Representation of the electrical double layer.

The magnitude of the zeta potential gives an indication of the stability of the colloidal system. If all the particles in suspension have a large negative or positive zeta potential then they will tend to repel each other and there is no tendency to flocculate. However, if the particles have low zeta potential values, then there is no force to prevent the particles coming together and flocculating. Particles with zeta potentials more positive than +30 mV or more negative than -30 mV are normally considered stable [41].

In this equipment, a laser is used to provide a light source to illuminate the particles within the sample, being this light source splitted to provide an incident and reference beam. The reference beam is also 'modulated' to provide the necessary Doppler effect. The laser beam passes through the centre of the sample cell, and the scattering at an angle of 17° is detected. With insertion of the cell into the cell holder, the cell terminals allow the system to recognise the type of zeta potential cell fits, which configures the software to use the correct measurement sequence. When an electric field is applied to the cell, any particles moving through the measurement volume will cause the intensity of light detected to fluctuate with a frequency proportional to the particle speed. A detector sends this information to a digital signal processor. This information is then passed to a computer, where the software produces a frequency spectrum from which the electrophoretic mobility and, hence, the zeta potential are calculated. The intensity of the scattered light within the cell must be within a specific range for the detector to successfully measure it; to provide this, an “attenuator” is used to reduce the intensity of the laser and hence reduce the intensity of the scattering. The configuration of a Zeta Potential equipment is represented in Figure 12.

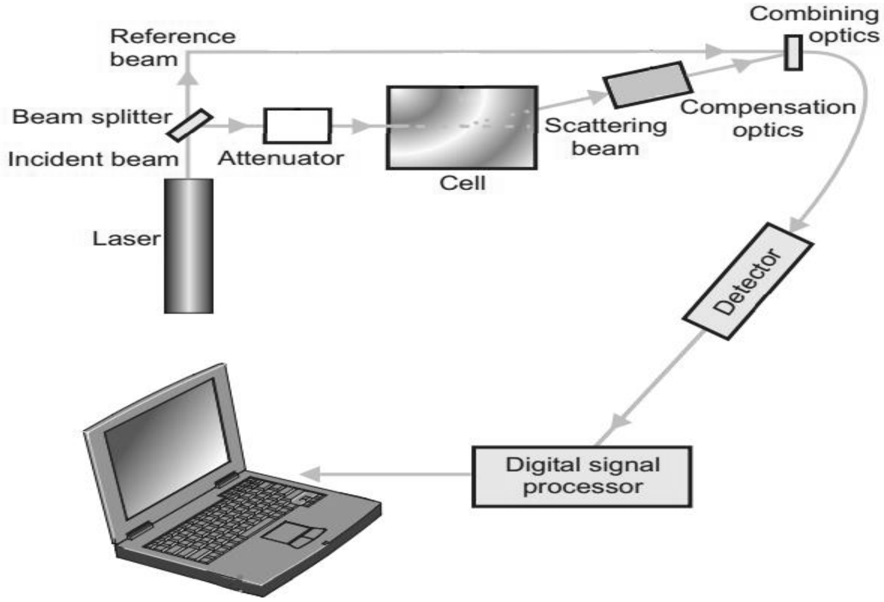

Figure 12. Configuration of a Zeta Potential equipment.

The most important factor that affects zeta potential is pH. A zeta potential value without a quoted pH is a virtually meaningless number. The point where the plot passes through zero zeta potential is called isoelectric point and is very important from a practical consideration. It is normally the point where the colloidal system is less stable.

2.5.9. Lowry Method for protein quantification

The most accurate method for determining protein concentration is acid hydrolysis followed by amino acid analysis. However, most other methods are sensitive to the amino acid type of the protein, and absolute concentrations cannot be obtained [42]. The procedure of Lowry *et al.* [43] is no exception, but its sensitivity is moderately constant from protein to protein, and it has been so widely used that Lowry protein estimations are a completely acceptable alternative to a rigorous absolute determination in almost all circumstances in which protein mixtures are involved.

The Lowry protocol is a two-step procedure. In a first step, a blue complex is produced by the reaction of the protein with Cu^{2+} ions in basic solution. In a second step, the intensity of the colour is enhanced by the reduction of phosphomolybdic-phosphotungstic reagent (Folin-Ciocalteau reagent) by tyrosine and tryptophan.

The implementation of this method needs the UV-Vis measurement of several samples with different protein concentrations in order to build a standard calibration curve that provides the obtainment of the protein concentration of the samples to being measured. All the procedures used in this method are further described in chapter 3.

2.5.10. UV-Vis Spectroscopy

As it was explained for FTIR spectroscopy (2.5.4), the spectroscopy is based on the study of the interaction between radiation and matter. This interaction causes in the atoms an electronic transition from a lower energetic level to a higher level due to energy absorption equal to the energy difference between both levels. Thus, UV-Visible spectroscopy (radiations with wavelengths between 10 and 1000 nm) provides information about the transition of the most external electrons of the atoms. Since different atoms or molecules absorb UV-visible radiation at different wavelengths, spectroscopy is massively used in analytical chemistry for the identification of substances through the spectrum emitted from or absorbed by them. This technique is also used to assess the concentration or amount of a given species using the Beer-Lambert law [44].

The Beer-Lambert law relates the absorption of radiation to the properties of the material through which it is passing through. It states that there is a logarithmic dependence between the transmission (or transmissivity), T, of light through a substance and the product of the absorption coefficient of that substance, α, and the distance the beam travels through the material (*i.e.* the path length), l. The absorption coefficient can, in turn, be written as a product of the molar absorptivity of the absorber, ε, and the concentration c of absorbing species in the material. For liquids, these relations are usually written as:

$$\log T = \log \frac{I}{I_0} = \varepsilon l c \; , \tag{15}$$

where I and I_0 are the intensity of the incident and the transmitted beams, respectively. The transmission can also be expressed in terms of absorbance (A):

$$A = -\log T \; . \tag{16}$$

So, Beer-Lambert equation can be written finally as:

$$A = \varepsilon l c \, . \tag{17}$$

Either transmittance or absorbance can be measured experimentally with the spectrometer. Thus, if the path length and the molar absorptivity are known and the absorbance is measured, the concentration of the substance can be deduced. Commonly, both parameters are constant for a given set of experiments, thus, a plot of the sample absorbance against its concentration should be a straight line. In practice, a calibration curve is obtained by plotting the measured absorbance of a series of standard samples as function of their concentration. If the absorbance of an unknown sample is then measured, the concentration of the absorbing component can be determined from this graph [44].

The basic parts of a spectrophotometer are a light source, a sample holder, a diffraction grating or monochromator to separate the different wavelengths of light, and a detector. The radiation source is often a Tungsten filament (300-2500 nm) and a deuterium arc lamp which is continuous over the ultraviolet region (190-400 nm). The detector is typically a photodiode. Photodiodes are used with monochromators, which permit that only light of a single wavelength reaches the detector.

A spectrophotometer can be either single beam or double beam. In a single beam instrument, all of the light passes through the same sample cell. First, the reference, I_o, (generally the solvent) must be measured before the sample. This was the earliest design, but is still in common use in both teaching and industrial labs. In a double-beam instrument, the light is split into two beams before it reaches the sample. One beam is used as the reference and the other passes through the sample. Some double-beam instruments have two detectors (photodiodes), and the sample and reference beam are measured at the same time. A diagram of a double-beam UV-Vis spectrometer is represented in Figure 13.

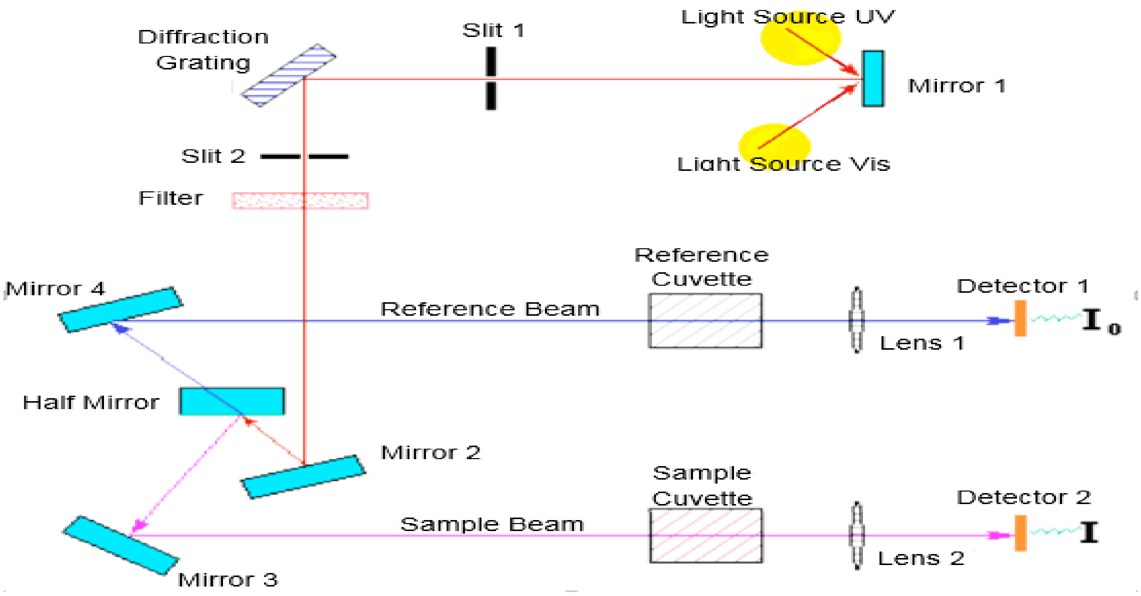

Figure 13. Schematic of a double-beam UV-Vis Spectrometer.

3. Experimental Procedures

This chapter briefly describes the used materials and procedures, as well as the characterization techniques applied during the entire experimental work that was performed. Throughout the course of this work the thermal decomposition technique was used for the synthesis of Fe_3O_4 nanoparticles.

3.1. Materials

Iron(III) acetylacetonate ($Fe(C_5H_7O_2)3$, $Fe(acac)_3$, 97%), oleylamine ($C_{18}H_{35}NH_2$, 70%), benzyl ether ($C_7H_7OC_7H_7$, 98%), hexane (C_6H_{14}, ≥99%), cyclohexane (C_6H_{12}, ≥99%), toluene (C_7H_8, ≥99.5%), tetrahydrofuran (C_4H_8O, ≥99%), 1,4-dioxane($C_4H_8O_2$, ≥99%), bovine serum albumin (BSA, ≥98%), α-casein from bovine serum and Folin-Cicalteau's phenol reagent were purchased from Sigma-Aldrich.

Sodium carbonate (Na_2CO_3, 98.8%) was bought from Gerbu and sodium hydroxide (NaOH, 98%) from PanReac AppliChem; copper sulfate ($CuSO_4.5H_2O$, 99%) and potassium sodium tartrate-4-hydrate ($KNaC_4H_4O_6.4H_2O$, 99.5%) were both purchased from Riedel-de Haën.

Phosphate-buffered saline (PBS), polyoxyethylene 20 sorbitan monooleate (Tween 80 or Polysorbate 80, $C_{64}H_{124}O_{26}$) and acetate buffer (pH = 3.6 and pH = 5) were produced and provided by investigators of Pharmaceutics Faculty of University of Coimbra. All presented reagents were used without any further purification.

3.2. Synthesis of Fe_3O_4 nanoparticles

Independently of the synthesis conditions that were used throughout the course of this thesis, which are posteriorly explained, Fe_3O_4 nanoparticles were always synthesized using the same experimental method – thermal decomposition – and assembly (Figure 14). Since this method requires high temperature, reflux was always used to condensate the released volatile gases.

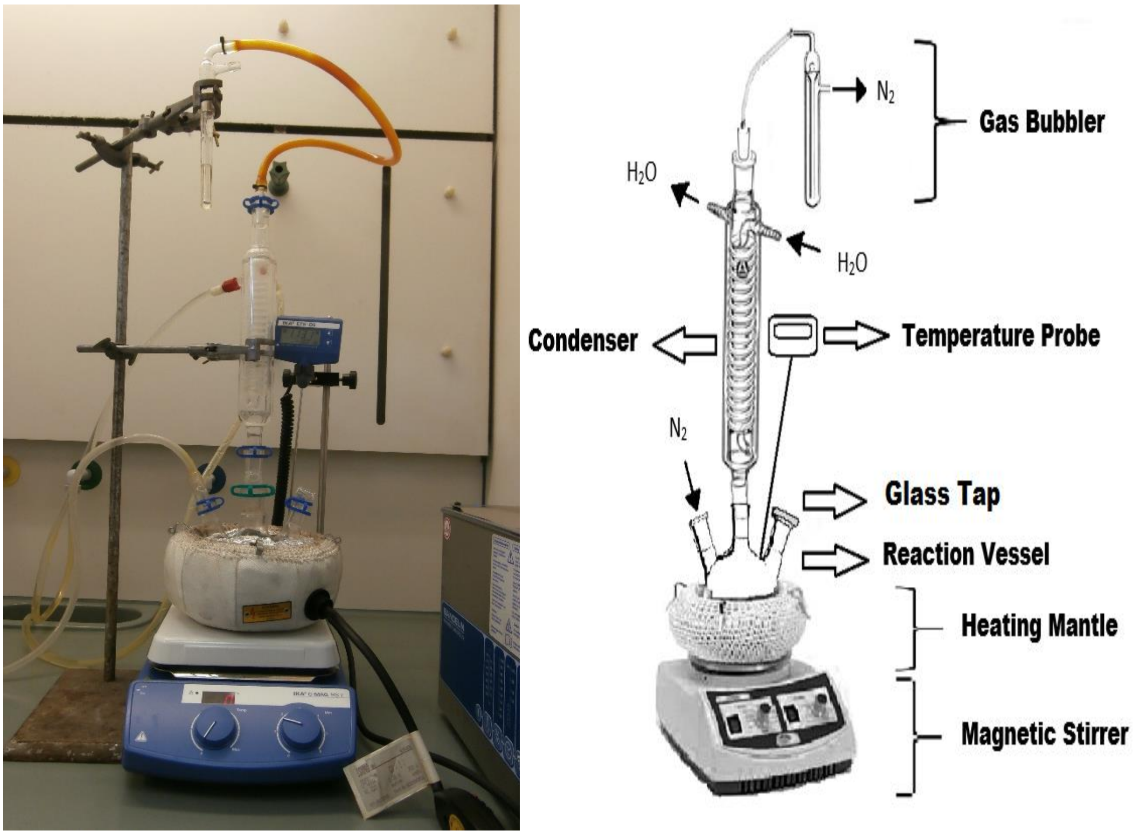

Figure 14. Real (left) and schematic (right) experimental assembly used in the synthesis of Fe_3O_4 nanoparticles.

The properties of the final nanoparticles may vary (particularly at nanoscale) due to small changes associated with: the equipment used in the experimental assembly, such as the inability to keep the heating mantle at a fixed temperature or the constant heat loss associated with the assembly; and details of procedures, such as the flow amount of N_2, the maintenance of temperature thresholds and the stirring speeds of the magnetic stirrer. To avoid these types of variations in nanoparticles characteristics, the levels of the N_2 flow and the stirring speed were controlled, as well as the temperature of heating mantle. Also, some renewable cotton jackets were used in order to prevent heat losses.

3.2.1. Procedures A, B and C

Initially, three major different procedures of synthesis were used: A, B and C. These were adjusted from the one used by *Xu et al.* [45] with changes on the amount and concentrations of the reagents.

In procedure A, 1 mmol of iron (III) acetylacetonate, 4 ml of oleylamine and 1ml of benzyl ether were added into a 3 neck round-bottom flask. Then, the mixture was magnetically stirred and put under a flow of N_2 during the reaction, in order to ensure an inert atmosphere that avoids the nanoparticles oxidation [45].

The temperature of the reactor was then increased and two thresholds of temperature were established: the first at 110 ^{o}C, during 75 minutes, for the formation of nuclei - nucleation process, and the second during 45 minutes at 300 ^{o}C, for the growth of nanocrystals. The first threshold was achieved at a heating rate of 10 ^{o}C min^{-1} and the second one was reached at 16^{o}C min^{-1}. Finally, the mixture was let to cool down until room temperature.

The two remaining procedures, B and C, were variations of the first (A), in order to investigate the effect of changing the initial ratio of oleylamine/benzyl ether in the resulting nanoparticles characteristics. This was made by changing the initial volumes of oleylamine and benzyl ether as summarized in Table 4.

Table 4. Volumes of oleylamine and benzyl ether and corresponding ratios used in procedures A, B and C.

Procedure	Volume of oleylamine (ml)	Volume of benzyl ether (ml)	oleylamine/benzyl ether Ratio (V/V)
A	4	1	4:1
B	2.5	2.5	1:1
C	1	4	1:4

3.2.2. Procedures A+A, B+B and C+C

In the A+A, B+B and C+C variations of the above procedures, before adding the iron (III) acetylacetonate to the respective volumes of oleylamine and benzyl ether into the 3 neck round-bottom flask, previously synthesized Fe_3O_4 nanoparticles were dried inside the reactor. This new approach was applied in order to achieve a larger size of the synthesized SPIONs, by using them as seeds [46] and expecting that no more nuclei would be created and the added $Fe(acac)_3$ would be used only for the nanocrystals growth. The temperature thresholds, time steps and heating rates were maintained as described before.

3.2.3. Procedures A*, B* and C*

These 3 procedures consisted in the variation of the time during which the second threshold of temperature was maintained. Thus, 1 hour was added in this part of the synthesis experiment, in order to better understand the impact that the increase of nanocrystals growth time in the nanoparticles size. A shorter time was not tested, as the original nanoparticles were already very small.

3.2.4. Procedures A(2x), B(2x) and C(2x)

Procedures A(2x), B(2x) and C(2x) were used with the objective of evaluating the influence of iron(III) acetylacetonate amount in the SPIONs size, shape and magnetic characteristics. As the name designations suggest, the initial amount of Fe(acac)$_3$ was doubled – 2 mmol was used. The volumes of oleylamine and benzyl ether that were used were the same as defined in Table 4. The remaining conditions/steps were the same as described in section 3.2.1.

3.2.5. Purification method

When the room temperature was achieved, the obtained mixture was dispersed in ethanol and centrifuged at 7000 rpm for 15 min. This separation process was repeated until a clear separation between the deposited nanoparticles and ethanol was observed.

3.2.6. Storage method

As hexane is a very polar solvent, it forms a highly stable nanofluid with the synthesized hydrophobic nanoparticles, and easily evaporates at room temperature. Thus, the deposited nanoparticles were re-dispersed in this solvent and stored in the refrigerator.

The obtained nanofluid was so stable centrifugation process proved to be inefficient to separate particles from hexane. So, this storage method can be applied until the synthesized nanoparticles are re-dispersed in water for future applications in human cells. Dispersion in water is only possible after coating the Fe_3O_4 nanoparticles with a surfactant, process that will be explained in the next section.

3.3. Stabilization of Fe_3O_4 nanoparticle suspensions

Nanoparticles are obtained and suspended in organic solvents. In order to evaluate the cytotoxicity of the nanoparticles in cell cultures, the organic solvent needs to be replaced by a non-cytotoxic solvent. With this objective, the particles were centrifuged and the supernatant was replaced by a compatible physiological buffer, like phosphate buffer saline (PBS). Compounds with surfactant properties were included on buffer composition to improve the physical stability of the suspension.

Tween 80 and bovine serum albumin (BSA) were tested as surfactants, mixing them in different concentrations with PBS. The surfactant concentrations ranged between 1% and 3% for BSA in PBS and from 1% to 5% for Tween 80 in PBS.

4 ml of the stored Fe_3O_4 nanoparticle suspensions were dried in glass cuvettes, letting hexane evaporate. Then, 4 ml of each surfactant mixture were added as re-suspension solvent and an ultrasonic bath was applied to homogenize those suspensions. Posteriorly, the new re-dispersed suspensions were let rest for 8 h to evaluate suspension stability, *i.e.* Fe_3O_4 nanoparticles deposition. Additionally, UV-Vis spectroscopy technique was applied (see 3.5.10.) in order to conclude about which surfactant solution allows a better stability of the Fe_3O_4 nanoparticle suspension.

3.4. Fe_3O_4 nanoparticles loading with α-casein and BSA

BSA and α-casein were chosen as model protein due to their isoelectric point (4.7 and 4.2-4.7, respectively). The protein loading of the SPIONs was firstly tested by directly mixing the protein aqueous solution and the stored hydrophobic nanoparticle suspension [47]. Since this loading process formed large clusters, due to the incompatibility of those components, a surfactant solution of PBS with Tween 80 was used to re-suspend the nanoparticles. This process increases the surface area available for protein adsorption and favors the interactions between the nanoparticles and the protein and, subsequently, may increases the protein adsorption.

The protein adsorption was quantified using an experimental procedure for protein quantification known as Lowry protein assay (see 2.5.9.) also described in detail later (3.5.11.).

3.5. Characterization techniques/procedures

3.5.1. X-Ray Diffraction (XRD)

The stored suspensions of nanoparticles could not be directly measured due to the presence of the liquid phase (hexane). For that reason, a procedure was developed that allowed a proper analysis of the nanoparticles which consisted in using a Pasteur pipette to deposit droplets of the solution in a microscope slide that had a parafilm mask. For each droplet deposited, hexane was let to evaporate. This process was repeated for 10 mL of the stored suspension with a concentration of 3.34 mg ml^{-1}, and a black-brown oily layer adhered to the glass. It was required an homogeneous deposited layer, but that process revealed to be difficult so the parafilm mask was essential to avoid the formation of a thin and heterogeneous layer. In the end of the microscope slide preparation, the mask was carefully removed.

X-ray patterns were recorded in a *Bruker 8D Advance* diffractometer working with 40 kV and 40 mA using a Ni-filtered Cu kα radiation (λ = 0.154184 nm) in a $\theta - 2\theta$ configuration of Bragg-Brentano geometry. The acquisition was usually in the 2θ range of 10-120^o with a step of 0.03^o and acquisition time for each step of 10 s. The diffractometer belongs to TAIL platform of University of Coimbra, installed at the Department of Physics. The software used to refine the cell parameters were TOPAS and EVA (both part of the Bruker diffractometer package).

The different phases present in the analyzed samples were identified by comparison of the XRD patterns with the ones stored in PDFs (Powder Diffraction Files) database from ICDD. The data of the diffractograms was compared with a calculated model (Pawley method), that is used to profile refinement and intensity extraction of powder diffraction data, constrained only by lattice parameters and FWHM distribution.

3.5.2. Transmission Electron Microscopy (TEM)

The procedure for implementation of this characterization technique involved a deposition of 25 µl of nanoparticles dispersion in a Cu microgrid, followed by drying during 30 seconds, and addition of a radioactive contrasting agent to allow a good quality image. This radioactive contrasting agent was also dried for 2 minutes. The concentration of the sample was very low, to assure its electron transparency and, consequently, a micrograph with measurable data.

The TEM equipment used for the analysis of the nanoparticles size was a *Jeol JEM 1400* transmission electron microscope, belonging to IBMC in Porto. This TEM is a 120 KV instrument, with a magnification range of 50X – 2 000 000X and resolution of 0.20 nm (lattice image). In the case of the tested samples, a magnification of 300 000X was applied.

3.5.3. Dynamic Light Scattering (DLS)

This characterization technique was used in order to evaluate the hydrodynamic diameter of the synthesized Fe_3O_4 nanoparticles. The necessary procedure for this characterization technique required an initial dilution of the original stored suspensions (one droplet of the nanoparticles suspension in 30 ml of the re-dispersive solvent) and a filtration of the nanoparticles agglomerates with a syringe filter of 450 µm. The diluted suspension was filtered into a glass cuvette and then applied in the DLS equipment. According to the report of count rate and approximation of the measuring models of the equipment, the sample to be measured was even more diluted or concentrated, with addition of more re-dispersive solvent or more droplets of the initial stored suspension, respectively.

Due to the inaccurate results obtained with hexane as re-dispersant solvent (see next chapter), others apolar solvents such as toluene, cyclohexane, 1,4-dioxane and tetrahydrofluran were used for that purpose. Independently of the solvent used, all procedures for this characterization technique were maintained.

A *Zetasizer Nano ZS* from Malvern Instruments was used for the analysis, equipment that belongs to the Chemical Engineering Department of the University of Coimbra. It allowed a size measurement range from 0.3 nm (diameter) to 10 µm using patented NIBS (Non Invasive Back scatter) technology. This equipment has a working range temperature between 0 to 90 °C and a He-Ne laser as light source. The used software was Zetasizer, part of the equipment package, applied to evaluate the measurement parameters.

3.5.4. Fourier Transform Infra-Red Spectroscopy (FTIR)

This characterization technique was applied to identify the chemical groups/bonds present in the synthesized Fe_3O_4 nanoparticles. To accomplish that purpose, a *FT/IR 4200* spectrometer from Jasco was used, selecting a wavenumber range of 4000-400 cm^{-1} with 4 cm^{-1} of resolution. The FTIR equipment that was used belongs to the Chemical Engineering Department of the University of Coimbra.

Initially, KBr was milled until a fine powder was obtained and, then, it was dried in an oven at 60^oC for 2 days. After that, 30 µl the sample were added to 79/80 mg of KBr powder, mixing them until a homogeneous powder was obtained. The mixture was then pressed to obtain a small, thin and translucent pellet for the analysis. Between each pellet, the mold was carefully cleaned to avoid contamination and inaccurate results.

Before acquiring the spectra of the samples a base line was built with a KBr pellet without sample in the equipment support. Then, the pellet with nanoparticles was placed in this support and the transmittance variation was recorded, according with the wave number of the incident radiation [48].

3.5.5. Thermal Gravimetric Analysis (TGA)

With the aim of quantifying the percentage of organic coating on the synthesized nanoparticles, thermal gravimetric analysis was applied. Similar to the XRD procedure, the stored suspensions of nanoparticles couldn't be directly measured due to the presence of the liquid phase. Thus, the same procedure of depositing the sample droplets in a microscope slide was applied.

When the samples of Fe_3O_4 nanoparticles were fully dried, they were transferred to the aluminum crucible of the measuring instrument. The used instrument was a *TGA Q50*, from TA Instruments. Its field-proven performance arises from a responsive low-mass furnace, ultra-sensitive scale, and efficient horizontal purge gas system (with mass flow control). So, under a nitrogen atmosphere, the samples were heated from room temperature to 600 °C, at a rate of 10 °C min^{-1}.

The obtained results were treated with the software of the instrument, TA Universal Analysis, which allows the graphical observation of the weight of the samples (or derivative) as function of its temperature.

3.5.6. Vibrating Sample Magnetometer (VSM)

This important characterization technique involved a drying procedure of the stored nanoparticles similar to the one applied for XRD and TGA procedures. The dried material was then weighted and placed in the powder sample support. The support was sealed and thoroughly cleaned to assure that there was not contaminating material that could saturate the measurement of weakly magnetic samples.

The sample support was placed in a rigid tube that vibrates vertically and the correct position of the sample was determined by a scanning in the sensitive zone of the magnetic coils. After this procedures, the $M(T)$ and $M(H)$ curves were obtained. The thermal dependence of the magnetisation was measured in zero-field cooled (ZFC) and field cooled (FC) curves under applied fields of 50 and 100 Oe. The hysteresis cycles where measured at room and low temperatures.

The magnetic measurements were performed in a VSM, with a cryogen-free Physical Properties Measurement System (*PPMS Dynacool Quantum Design*). The VSM belongs to TAIL platform of University of Coimbra, installed at the Department of Physics.

3.5.7. Mössbauer Spectroscopy

Mössbauer spectra were recorded at T=30 K with a conventional transmission geometry spectrometer with constant acceleration. The source was ^{57}Co in Rh matrix with a strength of 10 mCi. The fitting of spectra was done with Lorentz lines using the NORMOS program distributed by Wissel, Germany. Isomer shifts are given, as usually, relatively to α–Fe measured at room temperature.

The samples were dried in vacuum and, then, placed in a *perspex* sample holder.

The cryostat used was a closed-cycle system of low pressure helium gas, and is composed of several modules of "*Air Products and Chemicals, Inc*", like a compressor module, an expander module and a refrigeration system where the sample is placed.

This spectrometer and cryostat belong to CFisUC at Department of Physics of University of Coimbra.

3.5.8. Evaluation of the cytotoxicity

In order to perform these tests, the nanoparticles synthesized by procedures C(2x) and C were dried, weighted, UV-sterilized and dispersed in DMEM (culture medium), with 0.5% of Tween 80 which increased their stability in the suspension with a sonicate process for 60 s.

Then, cos-7 cells were seeded in a 96-well plate at a density of $1x10^5$ cells/well in 100 µl of DMEM and incubated 24 h. In the next day, medium was replaced by the same value of fresh medium and formulations were added to a final concentration from 0.975 to 2000 µg/ml of nanoparticles in each well. After incubation for 24 h at 37 °C, 20 µl of MTT 5mg ml^{-1} in PBS (pH=7.4) was added to each well and incubated for more 2 h at 37 °C. Then, the medium was removed and formazan crystals produced by metabolic active cells were solubilized with 200 µl of DMSO per well. In order to deposit the Fe_3O_4 nanoparticles, an 800 g (RCF) centrifugation was performed for 15 minutes and the optical density (OD) of the supernatant was measured at 540 nm with 630 nm as wavelength reference using a microplate spectrophotometer (*Thermo Scientific Multiskan EX*).

The viability of non-treated cells (control) was defined as 100% and the relative cell viability (%) calculated using the equation:

$$Cell\ viability\ (\%) = \frac{OD\ sanple(540\ nm) - OD\ sample\ (630\ nm)}{OD\ control\ (540\ nm) - OD\ control\ (630\ nm)} \times 100 \qquad (18)$$

3.5.9 Zeta Potential

Aiming to quantify the surface charge of the obtained Fe_3O_4 nanoparticles in several mediums, the measurement of the zeta potential was performed. The application of this characterization technique involved similar procedures to the ones applied in DLS. In fact, some of the measurements were done in the same instrument as DLS, *Zetasizer Nano ZS*, from Malvern Instruments (Chemical Engineering Department of the University of Coimbra). Other measurements were obtained with *Delsa Nano C Particle Analyzer* from Beckman Coulter (Pharmaceutics Faculty of University of Coimbra).

The Fe_3O_4 nanoparticles dispersed in PBS (6.66 mg/ml) were re-dispersed in water, PBS and acetate buffer using a dilution factor of 10 (100 µl:1 ml). Approximately 500 µl of these re-dispersions were put in the specific cell for Zeta potential measurement. Between the analyses of samples the cell was carefully washed with water to prevent any type of contamination.

3.5.10. UV-Vis Spectroscopy

The measurement of transmittance of the SPIONs dispersions allows an evaluation of their stability in the used solvents (see 3.3.). Furthermore, it can also give us a way to quantify the amount of protein adsorbed by the obtained Fe_3O_4 nanoparticles (see 3.4.). The UV-Vis spectroscopy was applied with both purposes.

To evaluate the stability of SPIONs dispersions, a *T70 UV-VIS spectrophotometer* from PG Instruments was used, which belongs to Chemical Engineering Department of the University of Coimbra. It required 4 ml of sample to fill the quartz cuvette. In addition, an automatic electronic background subtraction was needed, known as auto-zero procedure, for which only the dispersion agents were used. The samples to be measured were composed of those dispersion agents, PBS with BSA (1-3%) or Tween 80 (1-5%), and the synthesized SPIONs with a concentration of 6.66 mg/ml. For each sample, a spectrum of transmittance (%) as function of wavelength acquired using the UV Win5 software of the equipment.

In order to extrapolate the amount of protein adsorbed by Fe_3O_4 nanoparticles, the absorbance at 750 nm of some samples was measured according to the Lowry method (see 2.5.9. and 3.5.11.). That process was performed in a *Shimadzu UV 1603* spectrophotometer belonging to Pharmaceutic Faculty of University of Coimbra.

3.5.11. Lowry Method for evaluation of efficacy of protein adsorption

The application of this method for protein quantification required a specific protocol that has many variations of Lowry procedure depending on the laboratory. The procedures here described and applied were used for protein quantification of solutions of α-casein and BSA in different concentrations, where the stored nanoparticles were re-dispersed. The amount of protein in the supernatant was measured (after a centrifugation process) to be able to determine the efficiency of bonding of the protein to the nanoparticles (loading efficiency) and the capacity of nanoparticles to be loaded by the protein (loading capacity). These properties can be determined by :

$$Loading\ Efficiency\ (\%) = \frac{m_i(BSA) - m_s(BSA)}{m_i(BSA)} \times 100 \qquad (19)$$

$$Loading\ Capacity\ (\mu g/mg) = \frac{m_i(BSA) - m_s(BSA)}{m(nanoparticles)} \qquad (20)$$

being m_i(BSA) the initial mass of BSA (µg/ml), m_s(BSA) the mass of BSA in the surfactant (the measured property - µg/ml) and m(nanoparticles) the mass of nanoparticles in the dispersions (mg/ml).

For that, an adapted protocol[49] was performed, where the Lowry reagent was prepared fresh each day composed by 1 ml of sodium carbonate (370 mM), 800 µl of sodium hydroxide (245.25 mM), 100 µl of copper sulfate (7.8 mM) and 100 µl of potassium sodium tartrate-4-hydrate (14 mM) that were thoroughly mixed. Then, several dilutions were done of α-casein/BSA protein standard solution (5.0 mgml^{-1}) in acetate buffer (pH=5)/water, according to Table 5. From the 500 µl of each dilution, 200 µl of them were mixed with another 200 µl of Fe_3O_4 nanoparticles (1 mg/ml), already re-dispersed in acetate buffer or water with 0.1% of Tween80. These samples were mixed for 30 minutes and then centrifuged at 2300 rpm for 20 minutes, in order to remove and analyse the supernatant.

For 200 µl of each supernatant sample and α-casein/BSA standard protein dilutions, 2 ml of the Lowry reagent (previously prepared) was added and the suspension was allowed to stand for 10 minutes at room temperature. After, 100 µl of Folin-Cicalteau reagent was added to each sample and immediately mixed thoroughly.

Table 5.α-casein/BSA standard protein stock solution dilutions.

Stock solution (µl)	0	2.5	5	10	20	30	40	50	60	70
Acetate Buffer/Water (µl)	500	497.5	495	490	480	470	460	450	440	430
[protein] (µg/ml)	0	25	50	100	200	300	400	500	600	700

The absorption measurements at 750 nm were done after letting the samples stand for 20 minutes at room temperature. First, a plot curve of absorption at 750 nm versus α-casein/BSA standard protein content (µg/ml) was obtained and, then, the unknown protein content of each sample was calculated by using with the equation of the linear function obtained with the protein standards.

4. Discussion of SPIONs' characterization results – Physicochemical Aspects

In this chapter we will present and discuss the physicochemical characterization of all the synthesized SPIONs samples by applying the techniques described in the last chapter. Once we reach the end of this chapter, almost all of the different procedures and paths followed during the synthesis work will hopefully be clarified. Only the discussion of the results of their biological application will remain, which is presented in chapter 5.

4.1. Standard Mössbauer spectra of magnetite and maghemite

In order to draw a comparison between the synthesized materials using different procedures, some considerations about the standard Mössbauer spectra of magnetite and maghemite must be known and taken into account. This information will allow a proper analysis of the spectra obtained for those synthesized materials.

4.1.1. Magnetite Mössbauer spectra

At room temperature (RT), ^{57}Fe Mössbauer spectrum of magnetite shows 2 magnetic sextets, which strongly overlap (Figure 15). These sextets arise from the iron atoms in tetrahedral sites and in octahedral sites, respectively. There are also fast electron changes between Fe^{2+} and Fe^{3+} ions in octahedral sites providing time average species with only one magnetic sextet. The magnetic hyperfine fields are 49.0 T and 46.0 T [50].

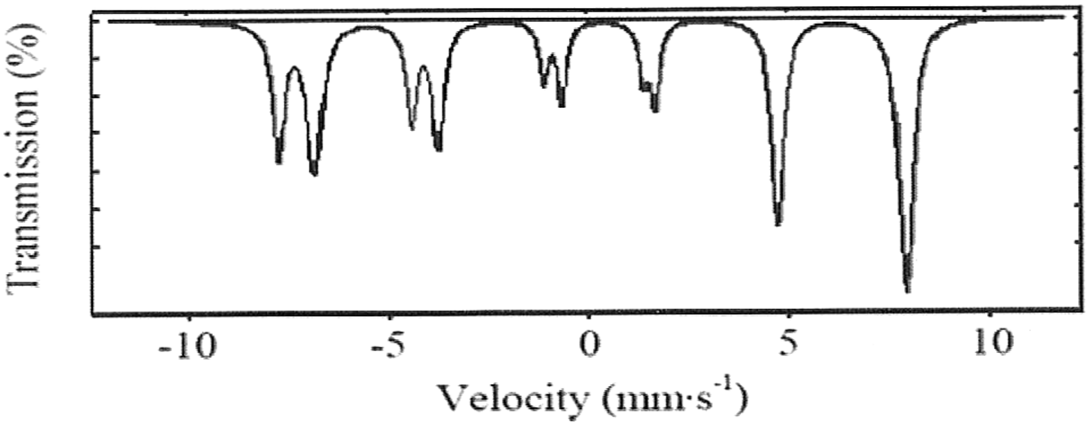

Figure 15. Mössbauer spectrum of natural magnetite at RT [51].

The spectrum of magnetite at 4.2 K (Figure 16), is commonly fitted with 5 sextets, but because of the lack of resolution, different models can be proposed. The model using 5 sextets was proposed by Berry *et al.* [53]. Four components correspond to Fe^{3+} and Fe^{2+} situated two non-equivalent octahedral sites of the inverse spinel-related structure, while the remaining one corresponds to Fe^{3+} on the tetrahedral sites. This spectrum has a very characteristic line at ~-3.5 mm/s.

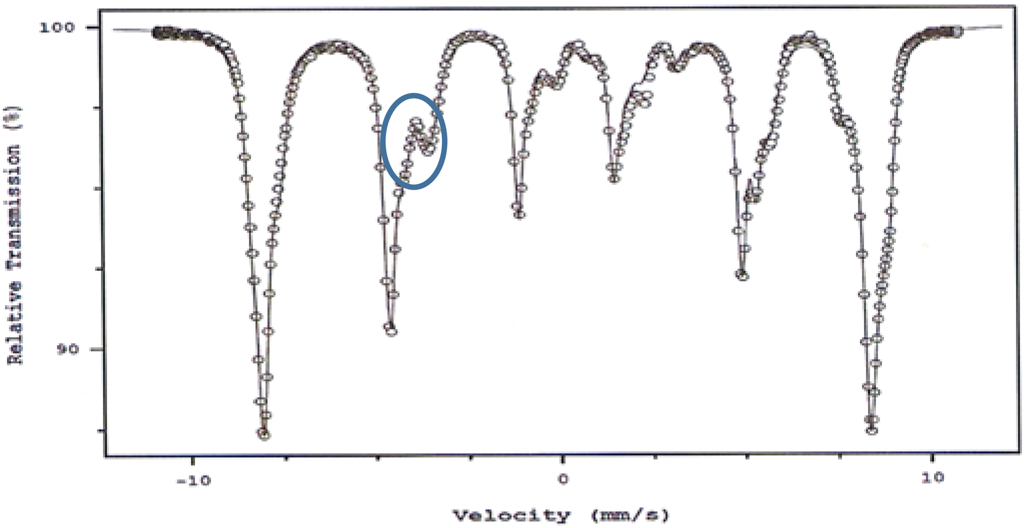

Figure 16. Mössbauer spectrum of natural (well crystalized) magnetite taken at 4.2 K [52].

Since nanoparticles have superparamagnetic behaviour and their magnetic properties can differ, depending on particle size and on the type of interactions between them, the spectra may be very complex [54].

The Mössbauer spectra recorded at different temperatures for magnetite with particle size of 5 nm is shown in Figure 17. The fitting of the 16 K spectrum with 5 magnetic sub-spectra results in hyperfine fields between 51.4 T and 43.9 T [54].

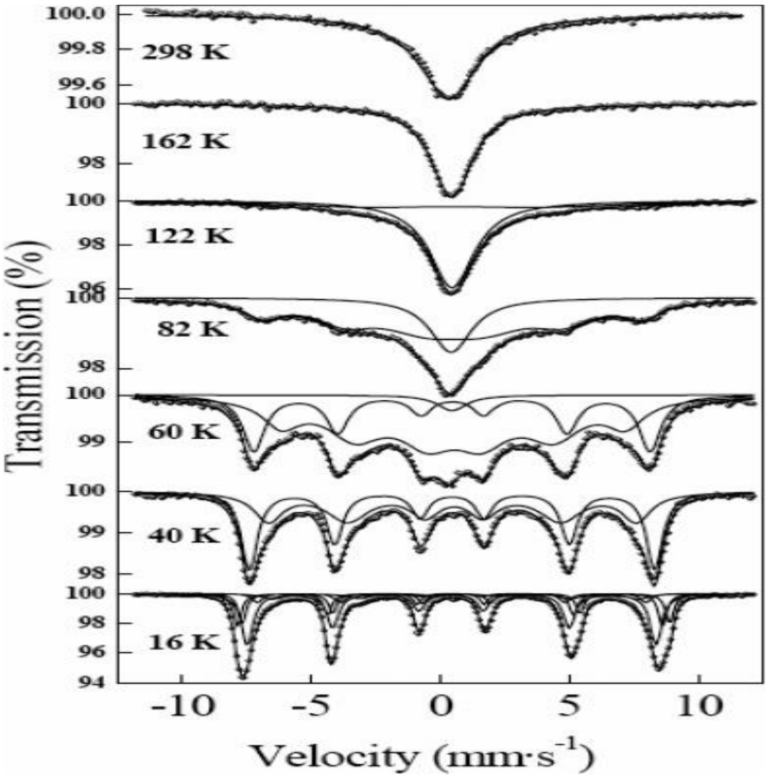

Figure 17. ^{57}**Fe Mössbauer spectra of magnetite with particle size of 5 nm for several temperatures** [54]**.**

From these spectra analysis, with an increase of temperature, it is visible the fading of the sextets and the appearance of a centred singlet.

4.1.2. Maghemite Mössbauer spectra

Figure 18 shows the ^{57}Fe Mössbauer spectrum of maghemite recorded at RT. This spectrum exhibits 2 magnetically split sextets with a small difference of the internal magnetic fields: 50.2 T and 50.5 T [51].

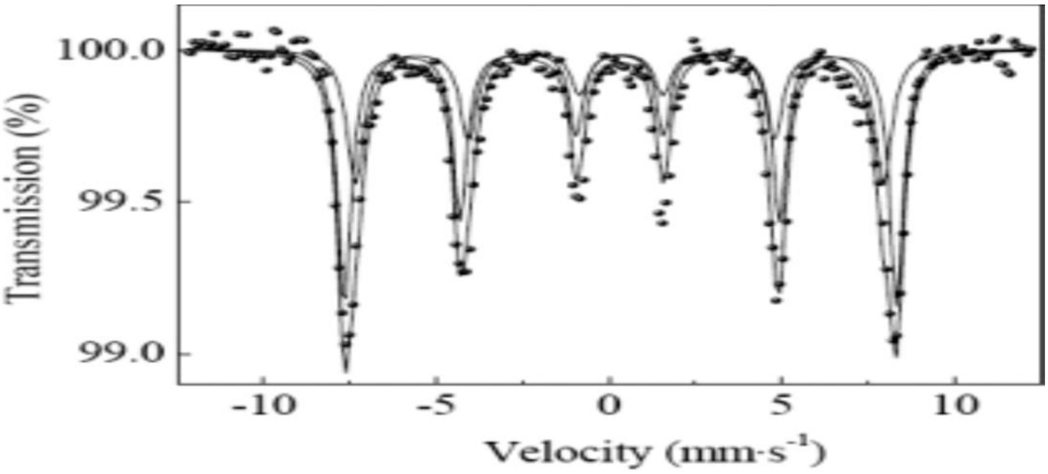

Figure 18. ^{57}**Fe Mössbauer spectrum of pure (well crystallized) maghemite taken at RT** [54]**.**

Figure 19 presents a typical spectrum of pure and crystalline maghemite obtained at 8 K. The asymmetry in the line depths should be noted, with the leftmost peak being narrower and deeper than the rightmost one. The spectrum can also be fitted with 2 sextets with internal magnetic fields of 48.0 T and 51.5 T [55].

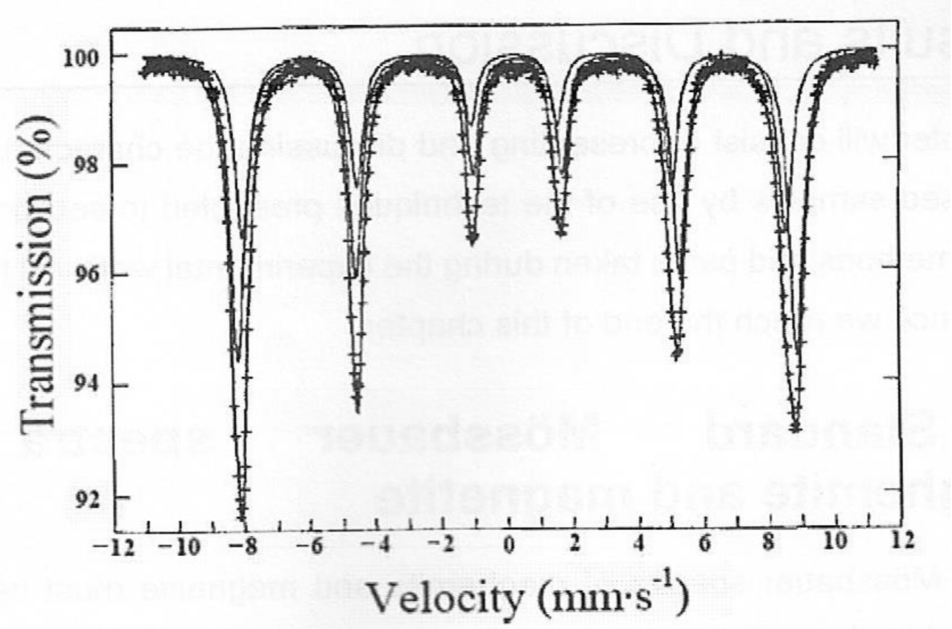

Figure 19. Mössbauer spectrum of pure (well crystallized) maghemite taken at 8 K [55].

As it will be shown in Figure 20, the spectrum taken at RT of nanoparticles with small sizes consists only of a central paramagnetic doublet, with parameters: IS = 0.33 mm/s and QS = 0.67 mm/s. The spectrum also shows a broad band [54]. At 16 K, the spectrum indicates the existence of 2 sextets with hyperfine fields of 51.7 T and 49.2 T. Small particle size decreases the hyperfine fields below that of bulk material and broad resonance lines [56]. However, direct comparison cannot be done by using these values with the values of bulk samples given above, because the spectra were taken at different temperatures.

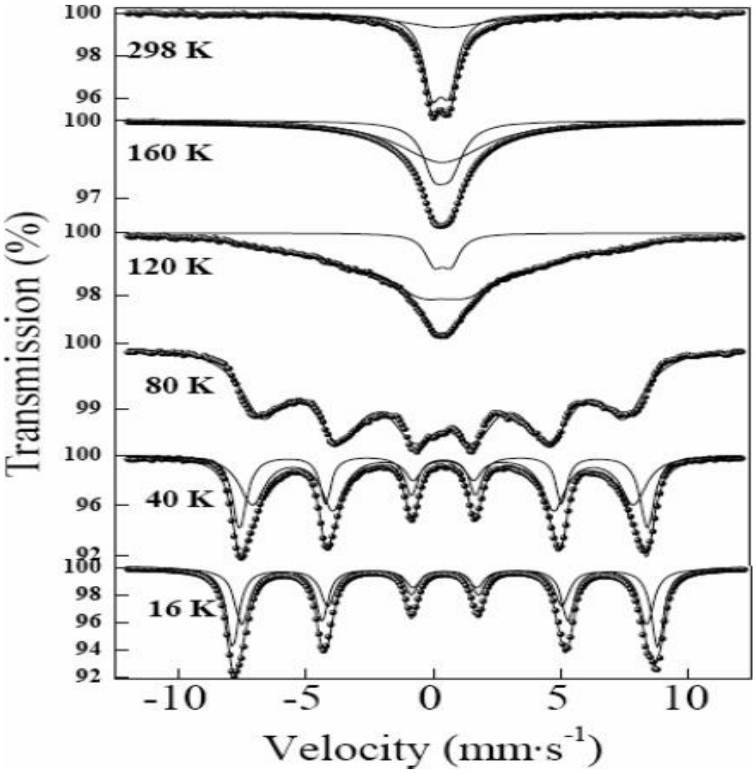

Figure 20. Mössbauer spectra of maghemite with particle size of 5 nm for different temperatures [54].

The separation between magnetic nanoparticles has an important influence in the magnetic dynamics due to the existence, or not, of magnetic particle interactions. Furthermore, the temperature dependence of the magnetic hyperfine field is also different for interacting and non-interacting nanoparticles, and the size of the magnetic hyperfine field is higher for interacting nanoparticles.

In this work, magnetite would be preferred over maghemite for the target application due to its higher saturation magnetization and susceptibility, saturating at lower magnetic fields. Given the significant broadening of the nanocrystalline character of the samples and the existence of a particle size distribution and changeable proportions of magnetite and maghemite in each sample produced in this work, data of spectra are difficult to analyse and must be carefully treated.

4.2. Influence of the time for nanocrystals growth on the characteristics of the obtained iron oxide nanoparticles

We begin by presenting and discussing the characteristics of the synthesized SPIONs from the starting procedures – A, B and C, followed with the characteristics of nanoparticles synthesized by the procedures A*, B* and C*, in which the time for nanocrystals growth was lengthen by 1 hour. Our goal slightly increase the nanoparticles size and verify the effect of this change in the magnetic yield, while optimizing the used oleylamine/benzyl ether ratio. Considering this challenge, the procedures that provide the most promising properties will be selected to pursuit the study.

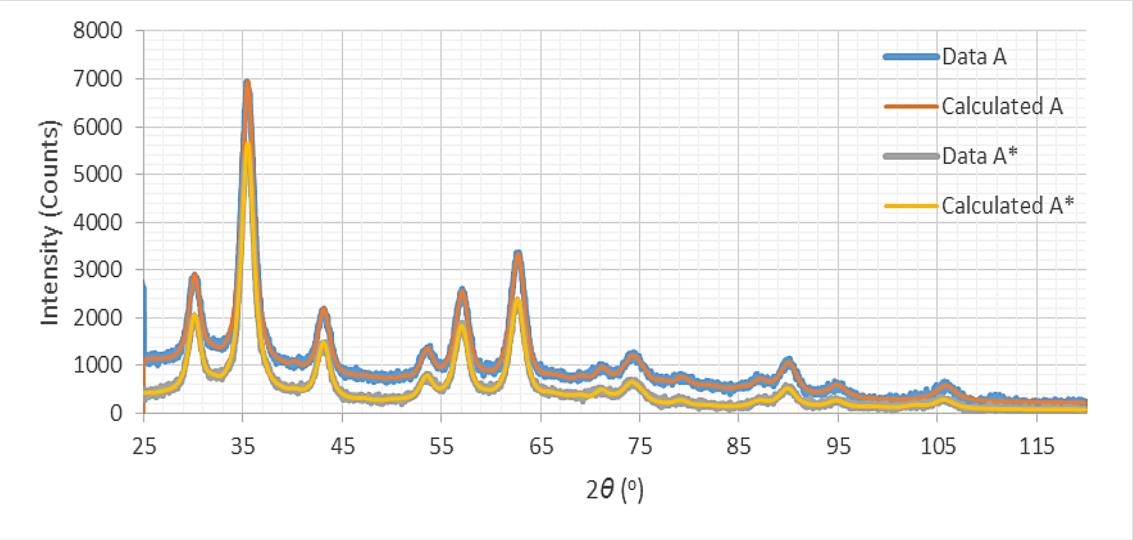

Figure 21. Diffractograms for samples obtained by procedures A and A*.

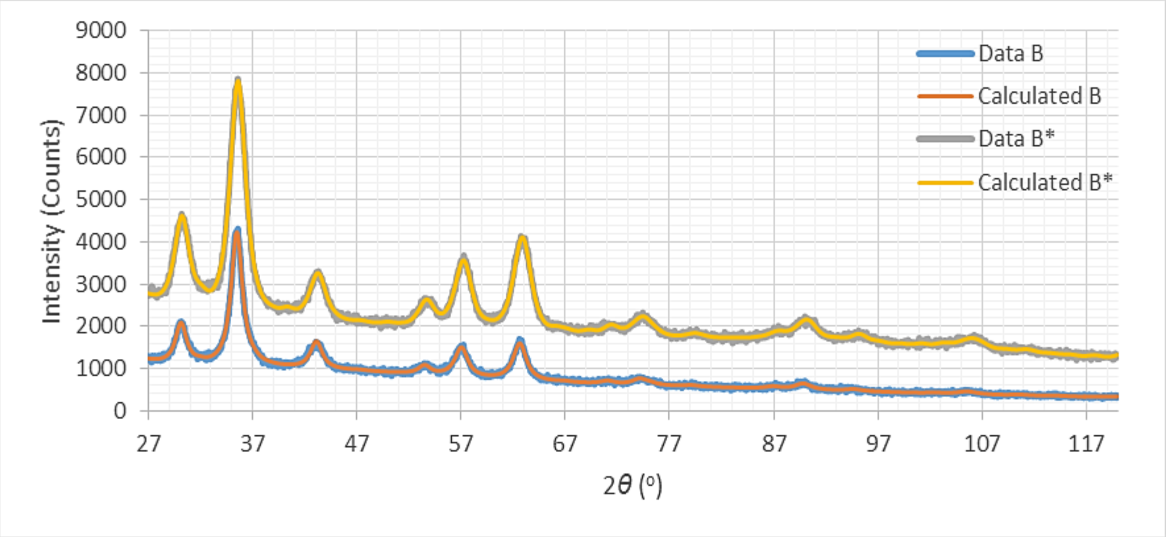

Figure 22. Diffractograms for samples obtained by procedures B and B*.

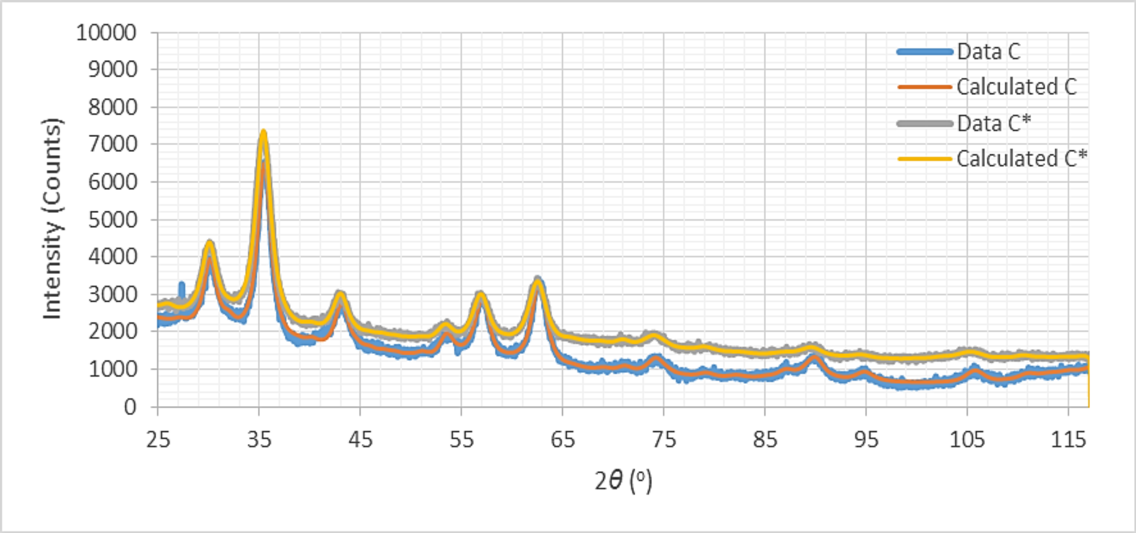

Figure 23. Diffractograms for samples obtained by procedure C and C*.

Figure 21, 22 and 23 show the diffractograms obtained by the XRD analysis of the samples A, A*, B, B*, C and C*. The main purpose was to calculate their lattice parameter (considering a cubic structure) and crystallites size. The diffractograms presented very broad lines, due to the yield nano-sized particles from all procedures, and their pattern is very similar when comparing the different samples. The peak exhibited in Data C of Figure 23 for 2θ=27.3° is related to an interference of the sample holder, which was made of aluminium. Table 6 presents the results obtained for the lattice parameter (*a*) and crystallites sizes (*D*) for the synthesis procedures under comparison.

Table 6. XRD derived results for the lattice parameter and crystallites size of nanoparticles produced by procedures A, A*, B, B*, C and C*.

Procedure	A	A*	B	B*	C	C*
***a* (nm)**	0.83540(11)	0.83677(31)	0.83771(14)	0.83357(27)	0.83613(34)	0.83598(35)
***D* (nm)**	6.85(81)	6.85(16)	6.53(14)	5.22(14)	6.36(20)	5.33(14)

Knowing that the reference value of the lattice parameter for maghemite is *a*=0.8347 nm, and for magnetite is *a*=0.8396 nm, the results exhibited in Table 6 show a mixture of both maghemite and magnetite for all procedures except for procedure B* that presents a dominant contribution of maghemite. There is a decrease in the value of the lattice parameter and crystallite size for B* and C* when compared to their respectively native procedures (B and C). The same didn't happen for A*, where the crystallite size remained unchanged and the lattice parameter increased, suggesting an increase of magnetite content for this procedure.

When the DLS technique was applied to measure the hydrodynamic diameter of the nanoparticles prepared by these procedures, there were some complications due to the solvent used for re-dispersions. There was a fast deposition of nanoparticles when hexane was used as dispersing medium, leading to incorrect measurements. Furthermore, a high variation of intra-sample sizes, a clear agglomeration for the majority of samples and a bad adjustment of the measurement models was verified. For these reasons, some other re-dispersive agents were tested: tetrahydrofuran (THF), 1,4-dioxane, toluene and cyclohexane. Only the last one allowed a proper measurement of the hydrodynamic diameter of the prepared nanoparticles and the acquired results are presented in Table 7.

Table 7. Hydrodynamic diameter measured by DLS for the nanoparticles obtained by procedures A, A*, B, B*, C and C*.

Procedure	Hydrodynamic diameter (nm)	
A	15,5 ± 1.9	
A*	19.2 ± 5.4	
B	19.1 ± 7.2	
B*	12.0 ± 3.7	136.1 ± 30.3
C	18.7 ± 3.1	
C*	32.9 ± 3.4	152.6 ± 21.6

DLS results show a small change of nanoparticles size of nanoparticle between samples prepared from procedures A and A*, and a clear agglomeration of nanoparticles synthesized from procedures B* and C*. This agglomeration is clear by the existence of two equal intensity peaks, whose diameters are represented in the table. It is worth nothing that, by the results presented in Tables 6 and 7, it can be concluded that each nanoparticle is constituted, at least, by 2-3 crystallites.

Since the DRX and DLS results for the nanoparticles synthesized by the procedures A*, B* and C did not reveal a significant increase in size of crystallites and/or nanoparticles or in the amount of magnetite, it was concluded that increasing the time of growth of nanocrystals had not the desired effect. On the other hand, it may cause agglomeration during the synthesis. This agglomerative effect of nanoparticles enhances their cytotoxic effect and, theoretically, reduces the drug absorption as the area/volume ratio is decreased.

By this point, procedures A*, B* and C* were abandoned as they did not lead to high quality and size-controlled superparamagnetic iron oxide nanoparticles with the necessary characteristics for drug delivery in brain. It was not possible yet to choose between procedures A, B and C, with the present results, but procedures A and C seem to be the ones with larger size of nanoparticles.

4.3. Influence of the addiction of seeds in the synthesis process (two stage-process) on the nanoparticles characteristics

Based on procedures A, B and C, procedures A+A, B+B and C+C were developed. As it was described in the experimental work, these procedures used previously synthesized nanoparticles as nuclei/seeds (nucleation targets) for the next synthesis, hoping that no more nucei were created, and the added Fe(acac)$_3$ was used in the nanocrystals growth. Once again, the criteria for the selection or rejection of the suitable procedures were mainly the obtained phase(s) and particle size.

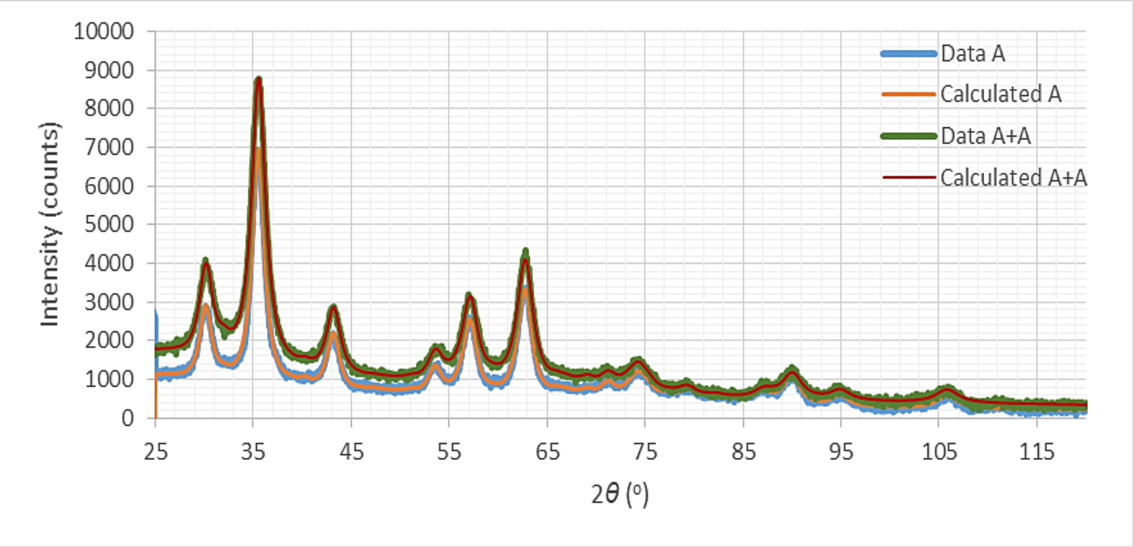

Figure 24. Diffractograms for samples obtained from procedures A and A+A.

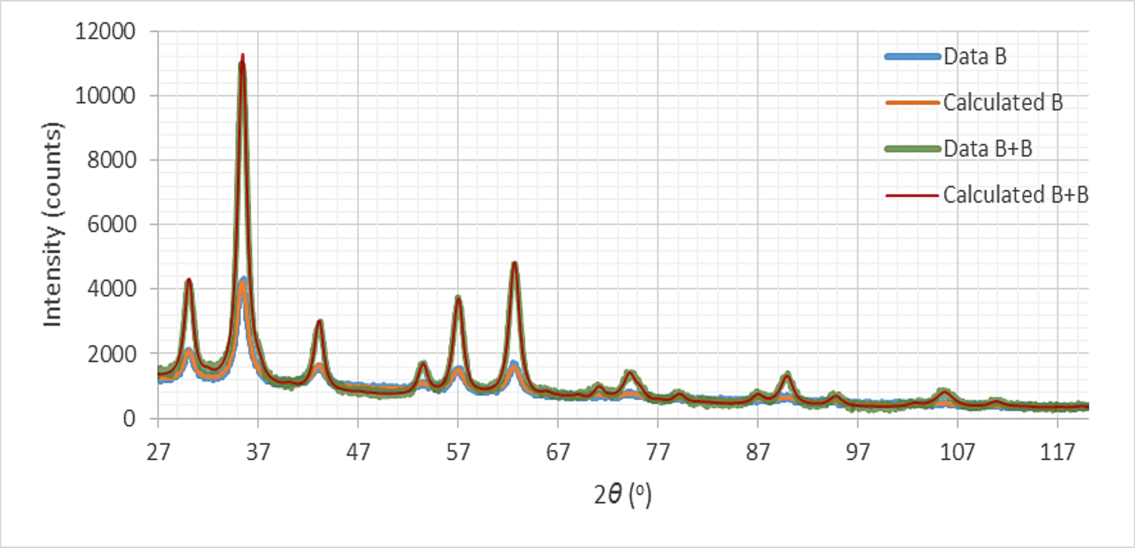

Figure 25. Diffractograms for samples obtained from procedures B and B+B.

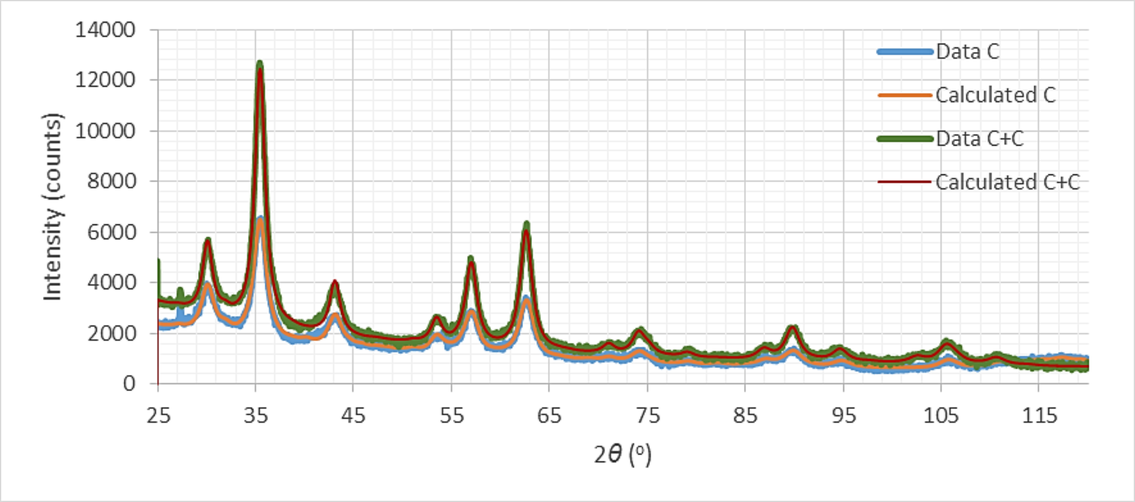

Figure 26. Diffractograms for samples obtained from procedures C and C+C.

Diffractograms of Figures 24-26, obtained for the referred samples continue to have very broad lines due to the yield nano-sized particles of all methods. The peak exhibited in Data C and Data C+C of Figure 26 for $2\theta=27.3^{o}$ is related to the sample holder, as it was described in Section 4.2. Besides that, the diffractograms show no significant difference between the position and shape of peaks for the samples compared in each figure, but the peaks intensity and the calculated lattice parameter change. Table 8 presents the results of nanoparticles calculated from DRX for the synthesis procedures under comparison.

Table 8. XRD derived results for the lattice parameter and crystallites size of nanoparticles produced by procedures A, A+A, B, B+B, C and C+C.

Procedure	A	A+A	B	B+B	C	C+C
***a* (nm)**	0.83540(11)	0.83624(53)	0.83771(14)	0.83699(12)	0.83613(34)	0.83785(18)
***D* (nm)**	6,.5(81)	5.62(14)	6.53(14)	9.99(14)	6.36(20)	7.640(76)

When we observe the values of the lattice parameter of each sample (Table 8), it is obvious that these values are between the reference ones for maghemite (*a*=0.8347 nm) and for magnetite (*a*=0.8396 nm), confirming the existence of a mix of the two iron oxides in these samples. A closer look lets us conclude that, except for procedure A+A, the crystallite size of the samples B+B and C+C increased when compared to the samples produced by their respective native procedures (B and C).

Table 9. Hydrodynamic diameter measured by DLS for the nanoparticles obtained by procedures A, A+A, B, B+B, C and C+C.

Procedure	Hydrodynamic diameter (nm)	
A	15.5 ± 1.9	
A+A	35.3 ± 5.0	
B	19.1 ± 7.2	
B+B	15.5 ± 1.1	130.0 ± 23.0
C	18.7 ± 3.1	
C+C	25.7 ± 2.3	120.2 ± 26.4

As can be observed in Table 9, and although XRD results did not give us that idea, DLS results indicate a significant change of the size of nanoparticles between samples prepared from procedures A and A+A. On the other hand, the results for the samples synthesized by procedures B+B and C+C indicate the formation of nanoparticles with two different hydrodynamic diameters that are not found in samples produced with B and C procedures. The existence of bimodal distributions for samples produced by procedures B+B and C+C can be possibly explained by the creation of more nucleation points with the Fe(acac)$_3$ that was added and, as before, due to agglomeration.

From the analysis of DLS results of Tables 7 and 9, we concluded that possibly, a reduction of the amount of oleylamine in the protective shell of the nanoparticles (B and

C procedures), in addiction with a procedure where time of growth of nanoparticles is increased, or where previously synthesized nanoparticles are added (as seeds) for the next synthesis, may promote an agglomeration of nanoparticles. Thus, it was decided to perform TEM analysis, in order to give us a reliable information about the particle size and agglomeration.

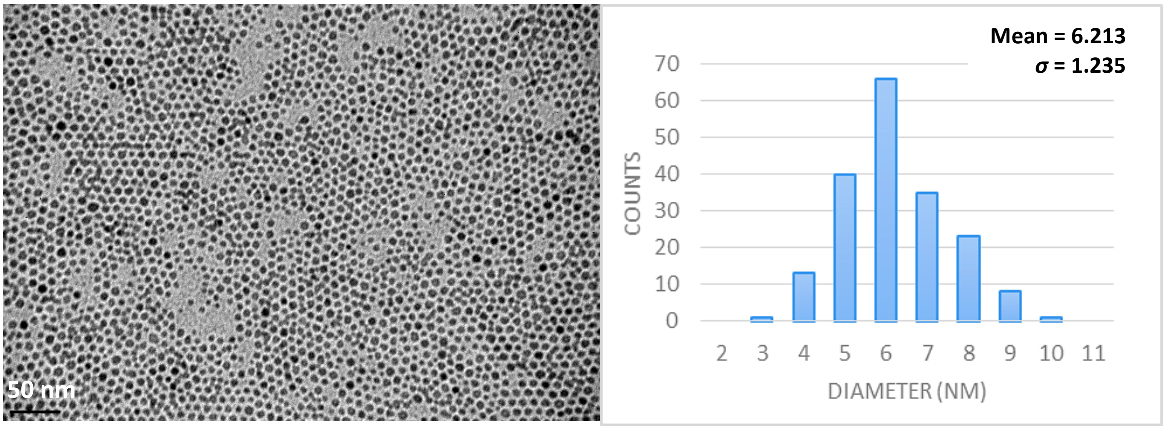

Figure 27. TEM image and respective size distribution for sample of procedure A.

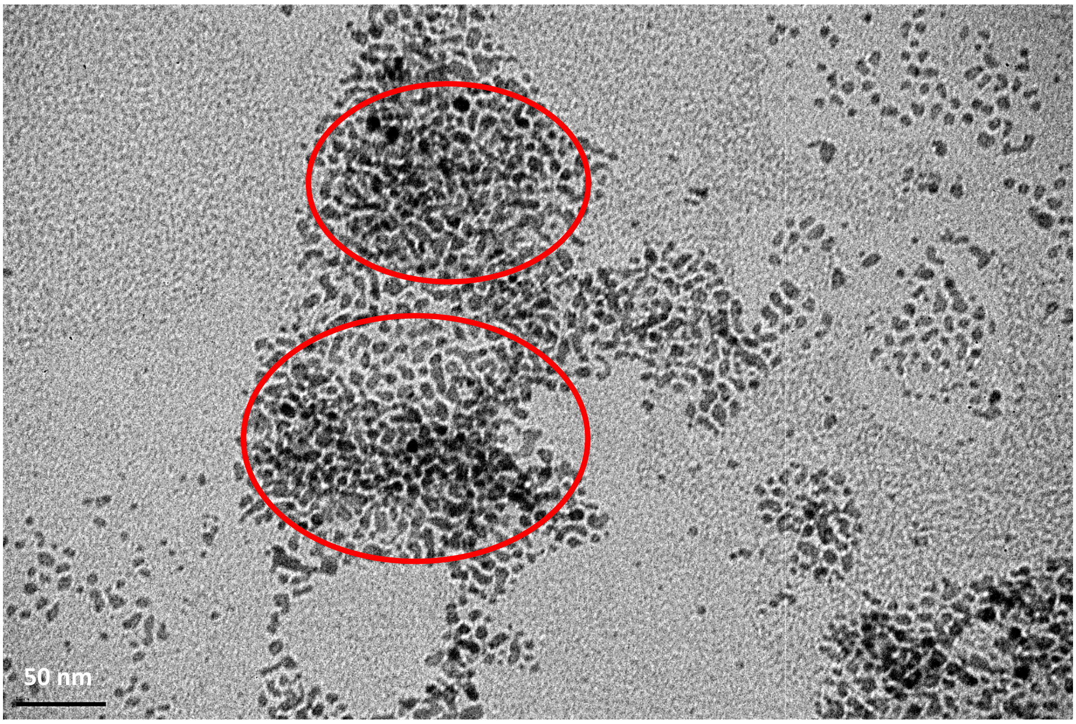

Figure 28. TEM image for sample of procedure A+A.

By observing Figure 27 and taking into account the confidence intervals, TEM results for particle sizes are consistent with those obtained from XRD analysis, meaning that each nanoparticle created from procedure A is composed by only one crystallite.

Thus, the DLS diameter seems to be oversized, which is possibly due to the hydrodynamic layer formed by the oleylamine coating (not clearly seen in TEM) and to some degree of agglomeration.

The particle sizes of the sample produced by procedure A+A were impossible to quantify by TEM, due to the agglomeration of nanoparticles observable in the circled areas of Figure 28, where there is high uncertainty related with the beginning and end of the nanoparticles. Therefore, the DLS result, although it measures a different property, was also affected by this agglomerative effect.

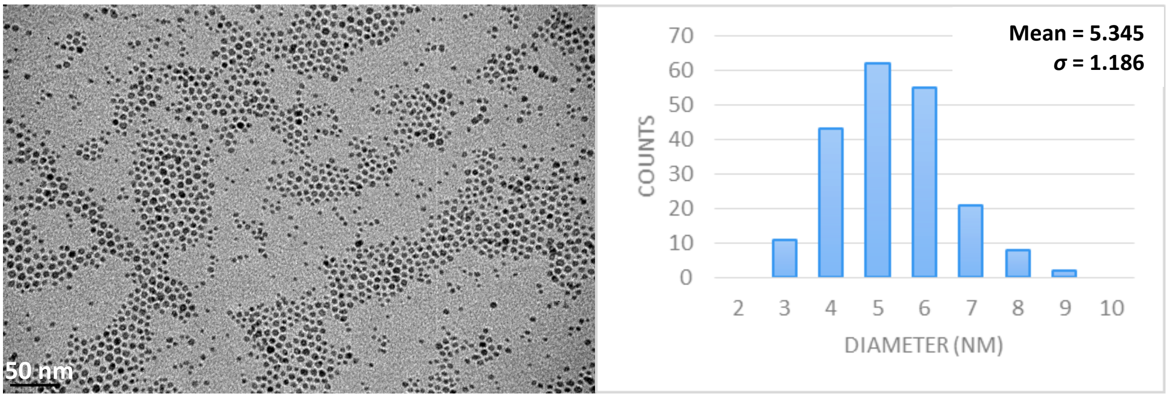

Figure 29. TEM image and respective size distribution for sample of procedure B.

As can be noticed in Figure 29, procedure B allows the production of well-dispersed iron oxide nanoparticles with average sizes consistent with the crystallite sizes obtained through XRD. Similar to procedure A, the nanoparticles prepared by procedure B are composed by a single crystallite but their size seems to be slightly lower. The DLS result for this sample was certainly also affected by the hydrophobic coating and some agglomeration.

The samples prepared by procedure B+B were not tested by TEM, since we had other more promising samples to test, and the ones synthesized by A+A and C+C could serve as comparison for the extreme ratios of oleylamine/benzyl ether used. The next figures (Figures 30 and 31) show the obtained TEM results for the samples synthesized by procedures C and C+C.

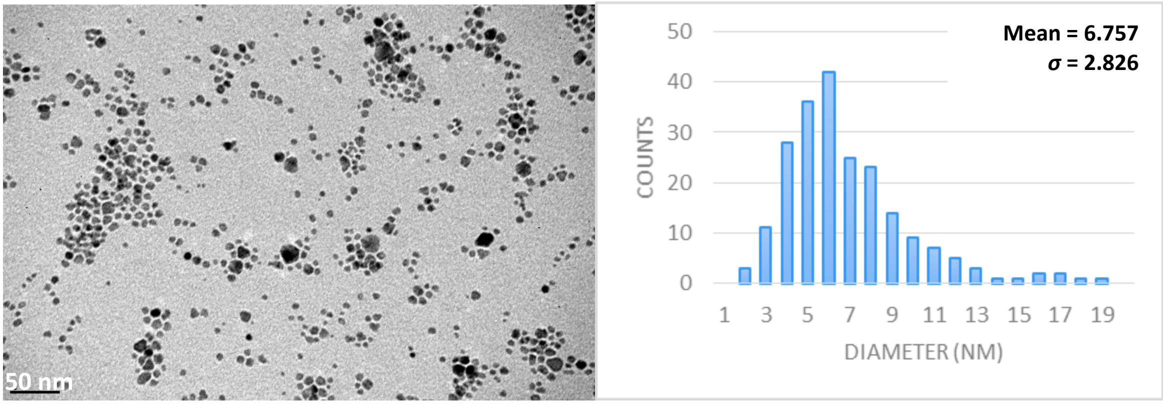

Figure 30. TEM image and respective size distribution for sample of procedure C.

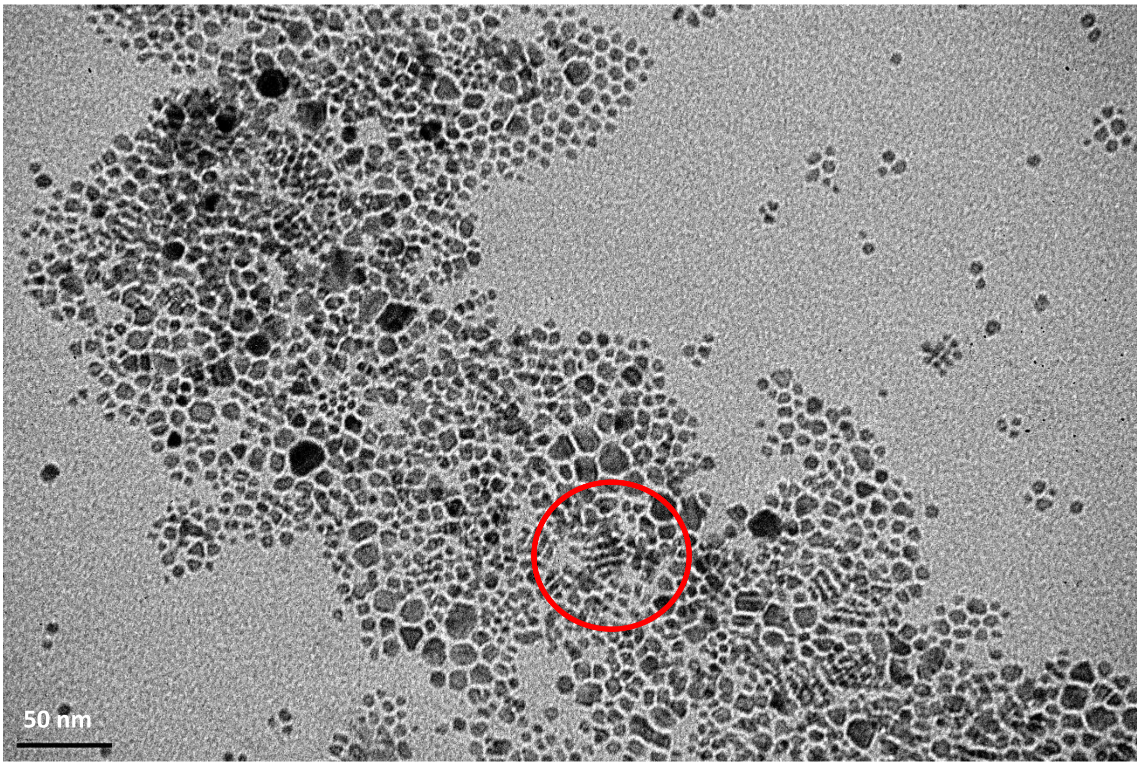

Figure 31. TEM image for sample of procedure C+C.

For samples prepared by procedure C, Figure 30 presents TEM results for particle sizes which continue to be consistent to those acquired from XRD analysis, if their confidence intervals are considered. Nanoparticles created by this procedure are also composed by a single crystallite and DLS results seem unreliable. It is important to refer the evident broader size distribution for this procedure in comparison with procedure A and B, given by the standard deviation values of 2.826, 1.235 and 1.186, respectively.

Once again, when we analyse the particle sizes of a sample produced by a procedure that uses previously prepared nanoparticles as points of nucleation for the next synthesis (C+C – Figure 31), it was impossible to quantify them by TEM. Apart from the observable formation of agglomerates of nanoparticles in the circled areas of Figure 31, there are some outlined areas where it seems to appear a degree of organization between nanoparticles, like it a crystallization effect is occurring.

Thus, the DLS measurements for samples of the C+C method are confirmed, due to the capacity of the instrument to separate and quantify the isolated nanoparticles from the agglomerates.

We can conclude that for procedures A+A, B+B and C+C, during the synthesis of nanoparticles, not only the used seeds acted as points of nucleation for the next synthesis, being created more nucleation points with fresh $Fe(acac)_3$ that the ones that were added. Therefore, few new nanoparticles were created similar to the first prepared ones, and others result from the growth and/or agglomeration of the prior nanoparticles.

From the previous discussion, it is clear that the procedures that use the previously prepared nanoparticles as points of nucleation for the next synthesis – A+A, B+B and C+C - are not prone to obtain sized controlled iron oxide nanoparticles and, because of that, they were discarded and not considered the best routes to pursue this work.

Procedure B was abandoned at this point, since the synthesis conditions are intermediate between A and C and TEM results proved that the nanoparticles produced by this procedure are the smallest ones.

4.4. Impact of doubling the amount of $Fe(acac)_3$ on the characteristics of the synthesized nanoparticles

Also based on procedures A and C, procedures A(2x), and C(2x) were used with the objective of evaluating the influence of iron(III) acetylacetonate quantities in the SPIONs size, shape and magnetic characteristics. As it was described in the experimental procedures, the initial amount of $Fe(acac)_3$ was doubled for these two procedures.

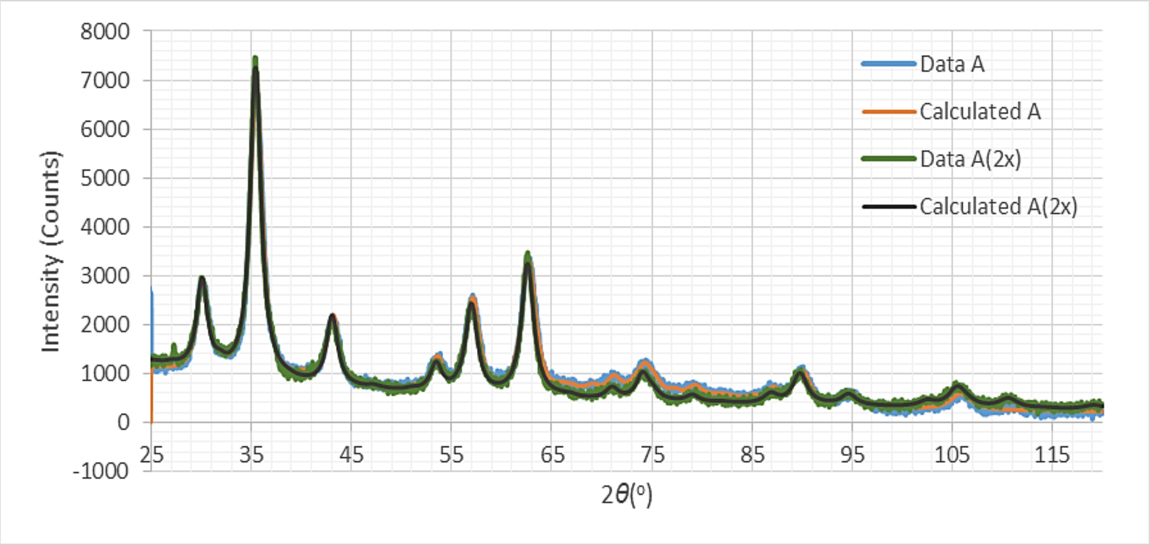

Figure 32. Diffractograms for samples obtained by procedures A and A(2x).

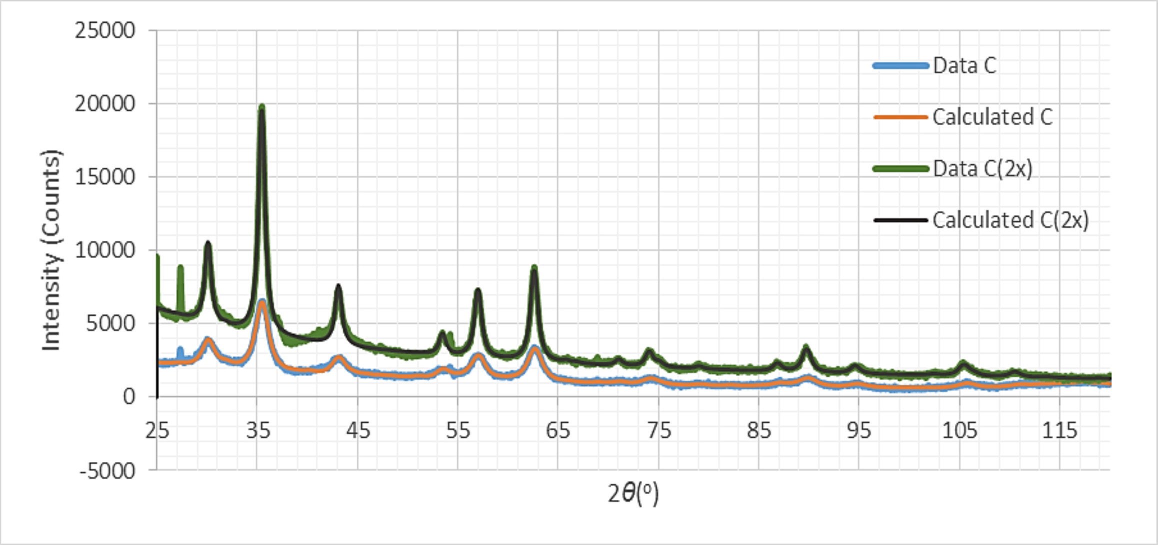

Figure 33. Diffractograms for samples obtained by procedures C and C(2x).

The samples synthesized by procedures A and A(2x) (Figure 32) depict a nearly perfect match between their respective diffractograms. Figure 33 also denotes a high similarity between the diffractograms obtained for the samples prepared by procedures C and C(2x), although different peak intensities. These XRD derived parameters are presented in the Table 10.

Table 10. XRD derived results for the lattice parameter and crystallites size of nanoparticles produced by procedures A, A(2x, C and C(2x).

Procedure	**A**	**A(2x)**	**C**	**C(2x)**
***a* (nm)**	0.83540(11)	0.83815(21)	0.83613(34)	0.83884(24)
***D* (nm)**	6.85(81)	7.40(11)	6.36(20)	11.12(12)

If we analyse the results in Table 10, it is noted an increase of the lattice parameter value for the samples synthesized by the procedures in which the amount of Fe(acac)$_3$ was doubled – A(2x) and C(2x), when compared with the corresponding native ones – A and C. Samples of procedures A(2x) and C(2x) are however still interpreted as mixtures of maghemite and magnetite, but this last phase seems to be the major contributing due to the higher proximity of the lattice parameter values of the samples and the reference value for magnetite (*a*=0.8396 nm).

The same enhanced effect happens with the increase of the crystallite sizes of each set of samples, being more evident for sample prepared by procedure C(2x).

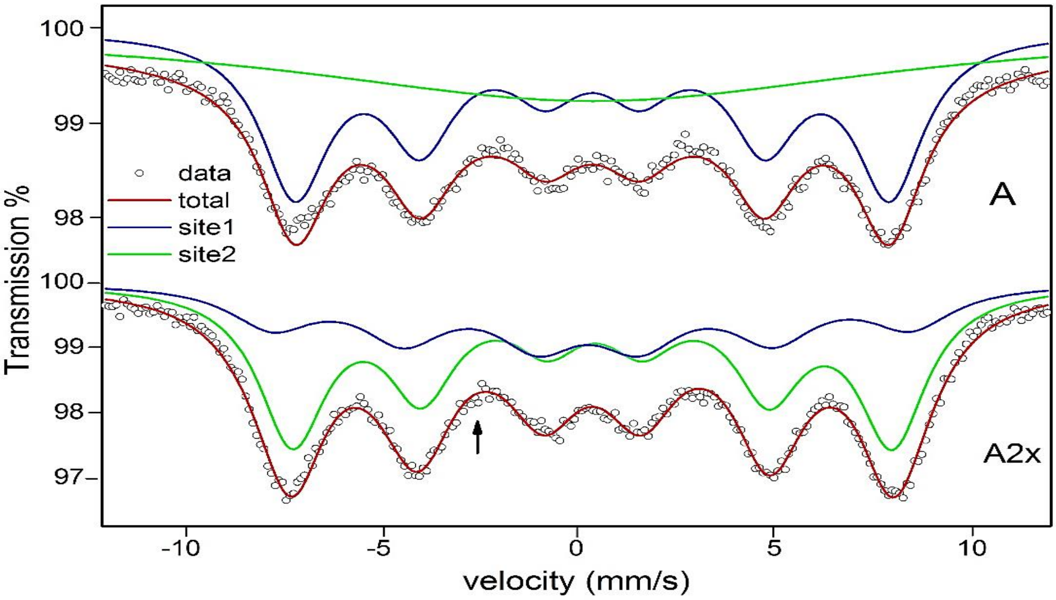

Figure 34. Mössbauer spectra of the samples obtained by procedures A and A(2x), taken at 30 K.

The Mössbauer spectra, at 30 K, for the sample of procedure A (upper part of Figure 34) presents a broad line that clearly represents a superparamagnetic relaxation effect, not typical at this low temperature. Although maghemite is the main phase of this sample, magnetite also exists (in a lower amount). The spectrum was fitted with a sextet with an average hyperfine field of about 46.6(1) T, which is typical of maghemite with small particles size [54]. The hyperfine parameters obtained by the fitting of a set of Lorentzians to the data are shown in Table 11.

Table 11. Mössbauer hyperfine parameters obtained by fitting the spectra shown in Figure 34,taken at 30 K, for samples A (upper part) and A(2x) (lower part).

Sub spectrum shape	IS ± 0.01 (mm/s)	QS ± 0.001 (mm/s)	H ± 0.1 (T)	FWHM ± 0.1 (mm/s)	Relative amount (%)	Iron sites
Sextet	0.51	-0.004	46.6	2.1	50.3	Fe^{3+}
Singlet	0.53	---	---	18.3	49.7	Fe^{3+}
Sextet 1	0.54	-0.065	47.0	2.1	63.5	$^{IV}Fe^{3+}$
Sextet 2	0.45	0.075	50.0	2.6	36.5	$^{VI}Fe^{3+}$

In turn, the lower part of Figure 34 presents the Mössbauer spectra at 30 K for a sample of procedure A(2x) for which two sextets were fitted, with broad lines (≥ 2.0 mm/s) and hyperfine fields of 47.0(1) T and 50.0(1) T that can be ascribed to magnetite with small particles (Figure 17) [54]. The characteristic line of magnetite at ~-3.5 mm/s is also present in this spectrum. Thus, comparing of the two spectra of Figure 34, the synthesis procedure A(2x), shows a higher content of magnetite, while the sample from procedure A has major amount of maghemite. These results are consistent with the earlier conclusions based on the obtained lattice parameter values from XRD analysis.

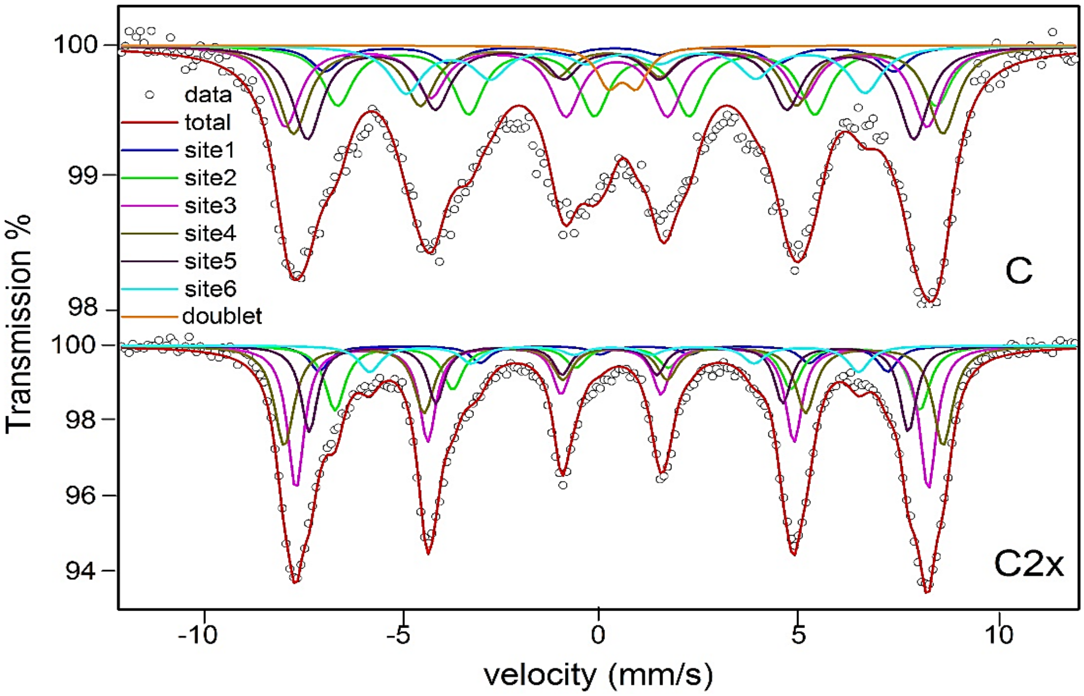

Figure 35. Mössbauer spectra of the samples obtained by procedures C and C(2x), taken at 30 K.

Table 12. Mössbauer hyperfine parameters obtained by fitting the spectra shown in Figure 35, taken at 30 K, for samples C (upper part) and C(2x) (lower part).

Sub-spectrum shape	IS ± 0.01 (mm/s)	QS ± 0.001 (mm/s)	H ± 0.1 (T)	FWHM ± 0.01 (mm/s)	Relative amount (%)	Iron sites
sextet 1	0.44	-0.120	44.0	0.90	5.5	Fe$^{2.5+}$ oct.
sextet 2	1.13	-0.120	46.3	0.90	20.5	Fe^{2+} oct.
sextet 3	0.43	-0.260	49.7	0.90	21.2	Fe$^{2.5+}$ oct.
sextet 4	0.48	0.240	50.3	0.90	18.7	Fe^{3+} tet.
sextet 5	0.42	-0.019	47.0	0.90	19.9	Fe$^{2.5+}$ oct.
sextet 6	0.88	0.312	35.5	1.00	11.1	Fe^{3+}
doublet	0.60	0.700	-------	0.70	3.1	Fe^{3+}
sextet 1	0.74	-1.038	44.0	0.60	6.3	Fe$^{2.5+}$ oct.
sextet 2	0.96	0.137	45.3	0.60	15.7	Fe^{2+} oct.
sextet 3	0.43	0.024	49.0	0.55	29.1	Fe$^{2.5+}$ oct.
sextet 4	0.37	-0.036	51.0	0.60	24.4	Fe^{3+} tet.
sextet 5	0.37	-0.020	46.4	0.55	17.5	Fe$^{2.5+}$ oct.
sextet 6	0.48	0.036	37.8	0.65	7.0	Fe^{3+}

The Mössbauer spectra shown in Figure 35, related to the samples produced by procedures C and C(2x), obviously indicates a mixture of magnetite and maghemite. The obtained spectra were fitted with the 5 magnetic sub-spectra model proposed by Berry *et a*l. with hyperfine fields between 51 T and 44 T, which is the common procedure used to fit magnetite spectra collected at low temperature [54]. From this fitting procedure, another sextet arised with a low field (Table 12 - 11% and 7% of the spectra for C and C(2x), respectively) that can be ascribed to maghemite with very small particles. For the sample prepared by procedure C, a Fe^{3+} doublet (3%) was also found in its spectrum, denoting a higher content of maghemite, when compared with the sample prepared with the doubled amount of $Fe(acac)_3$ – C(2x). From these results, it is possible to state that samples obtained from procedures C and C(2x) have ~14% and 7% of maghemite, being the remaining part magnetite. This is a very high yield of magnetite.

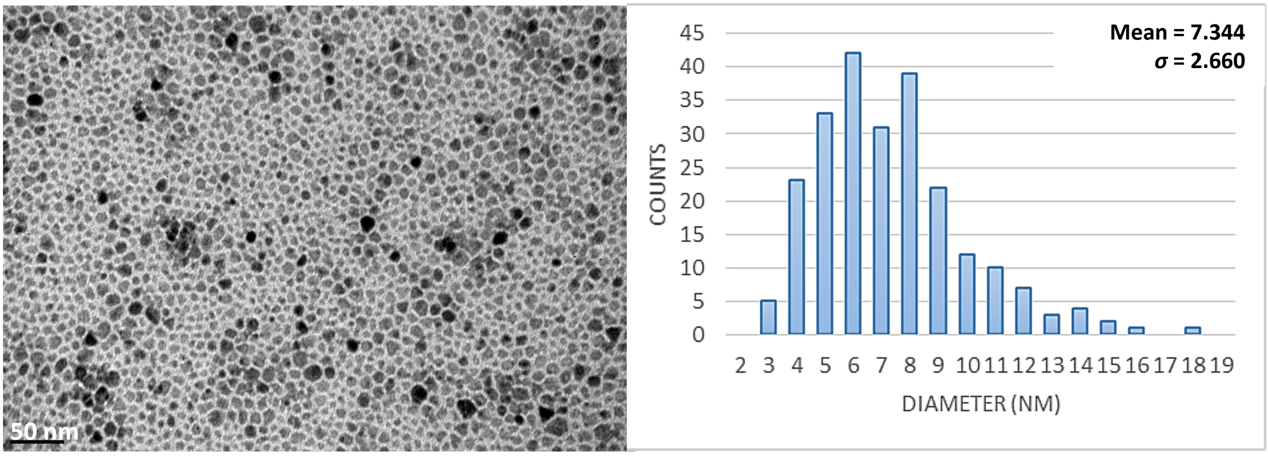

Figure 36. TEM image and respective size distribution for sample of procedure A(2x).

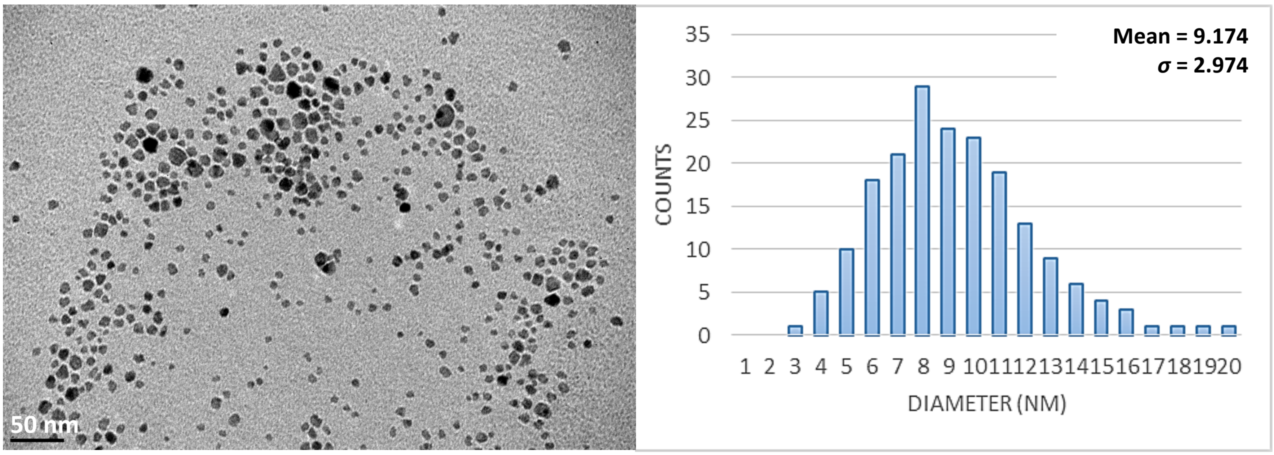

Figure 37. TEM image and respective size distribution for sample of procedure C(2x).

TEM results for samples produced by procedures A(2x) and C(2x) are presented in Figures 36 and 37, respectively. In both samples the average size of particles increased comparing to the TEM results obtained for samples synthesized by their native procedures, A and C (Figures 27 and 30) – 6.213 and 6.757 nm, respectively. This growth in particle size is consistent with the same increase in their respective crystallite sizes. Comparing these values we can assure that each particle is composed by a single crystallite, being these particles bigger when the amount of precursor is doubled during the synthesis of nanoparticles.

Table 13. Hydrodynamic diameter measured by DLS for the nanoparticles obtained by procedures A, A(2x), C and C(2x).

Procedure	Hydrodynamic diameter (nm)
A	15.5 ± 1.9
A(2x)	24.8 ± 2.9
C	18.7 ± 3.1
C(2x)	28.6 ± 2.1

As observed in Table 13, and as the XRD average crystallite size and TEM average particle size announced, the DLS results also indicate a significant increase in the size of nanoparticles between samples prepared from procedures A and A(2x). The same happened between samples prepared by procedures C and C(2x).

These improved results for particles size leads us to believe that doubling the amount of Fe(acac)$_3$ in the beginning of the synthesis is the most suitable route to pursue our goal. Thus, a further analysis of magnetic properties of the samples prepared by these procedures was done, always comparing them with the obtained results for the respective nanoparticles obtained by A and C procedures.

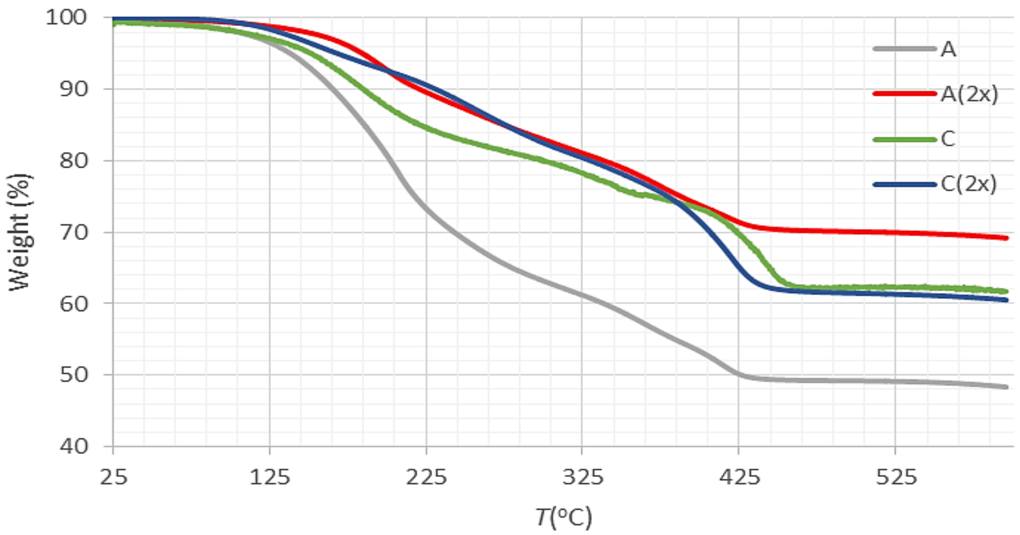

Figure 38. Thermograms of samples of procedures A (grey), A(2x) (red), C (green) and C(2x) (blue).

Figure 38 presents the thermograms showing the difference between the amounts of coating on nanoparticles for procedures A, A(2x), C and C(2x). This becomes clearer upon further analysis of the residual weight percentage of the samples, which indicate that samples from procedure A have a 51.52% of coating to 48.48% of iron oxide, contrasting with the ratio obtained for samples of procedure A(2x) with 30.73% of coating to 69.27% of iron oxide. As for procedure C, a ratio of 37.31% of coating to 62.69% of iron oxide was obtained, similar with the ratio obtained for procedure C(2x) of 39.45% to 60.55%. These results improved our understanding of the used procedures. When the amount of benzyl ether is lower, as in A and A(2x), the percentage of coating depends on the ratio between the volume of oleylamine and the amount of $Fe(acac)_3$ used during the synthesis. However, when the amount of benzyl ether is higher, as in C and C(2x), that dependence does not seems to exist since there is no significant difference in the percentage of coating.

The calculated percentage of iron oxide for each procedure allows us to obtain the magnetic properties of the samples as function of their iron oxide masses instead of the total mass of each sample. In this way we have better means of comparison with theoretical magnetic values.

In superparamagnetic materials, the magnetization *M* of these materials follows the Langevin's law:

$$M = nm\left[\coth\left(\frac{mH}{kT}\right) - \frac{kT}{mH}\right] \quad (21)$$

where, *m* is the magnetic moment of one particle which is, in first approximation, proportional to the volume of the particle, *n* is the number of particles, *H* is the magnetic field, *k* is the Boltzmann's constant and *T* is the temperature.

The magnetization curves represent the behaviour of the magnetic moment (classified in emu: being 1 emu = 1000 A/m) as a function of the magnetic field and temperature. These curves will be now presented.

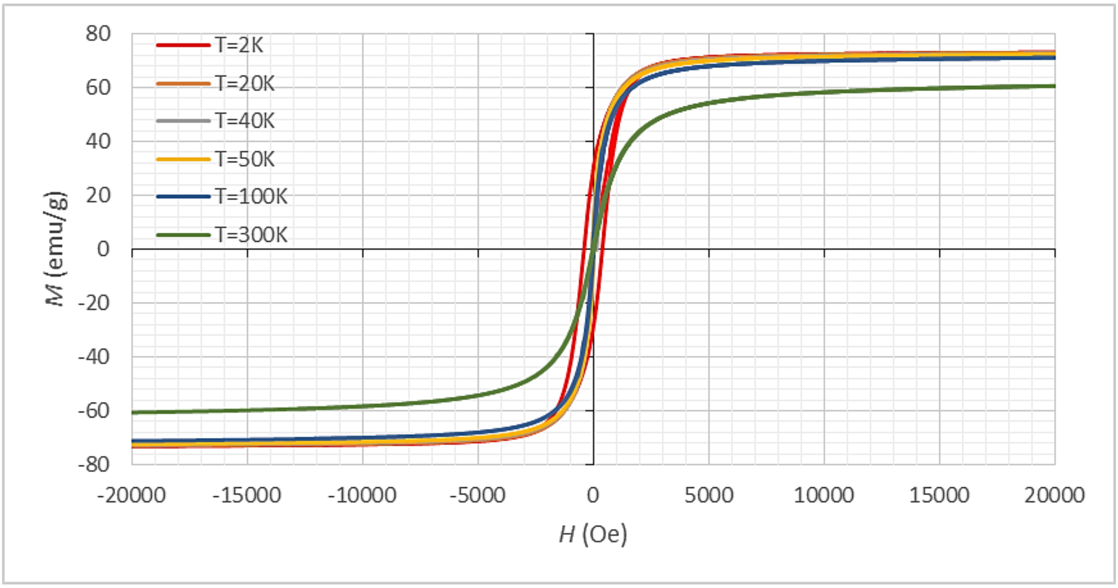

Figure 39. Magnetization as function of the applied field, for different temperatures - Sample A.

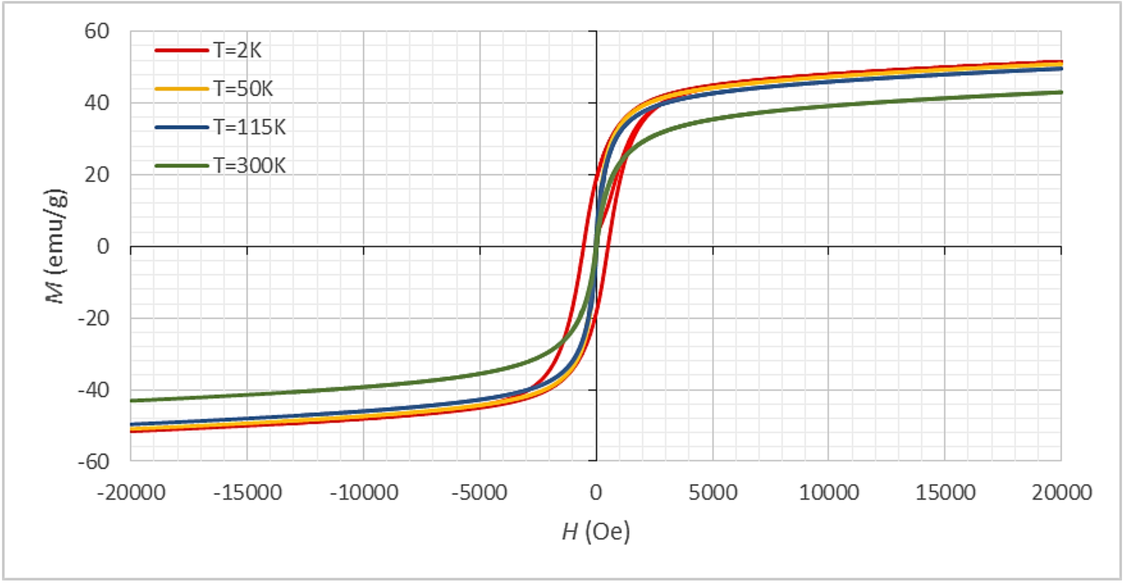

Figure 40. Magnetization as function of the applied field, for different temperatures - Sample A(2x).

Figures 39 and 40 show the magnetization of the samples obtained by procedures A and A(2x), respectively. From their analysis, the magnetization saturation obtained, at 300 K, for sample A (about 60 emu g^{-1}) is higher than for sample A(2x), although until 20 kOe the magnetization did not reach saturation. At lower temperatures, the magnetization saturation of both samples increased and, for sample A (73 emu g^{-1}) the magnetization saturation continues to be higher than the obtained for the sample A(2x) - ~50 emu g^{-1}. Is supposed that the inexistence of magnetization saturation may indicate presence of a paramagnetic effect probably due to the surfactant coating of oleylamine in the nanoparticles.

According to literature, magnetization saturation values found for maghemite particles with 5 nm is 35 emu g^{-1}at room temperature (RT) and 42 emu g^{-1}at 5 K and, for magnetite particles of equal size, 50 emu g^{-1}, at 5 K [57][58]. The values obtained in this work for samples A and A(2x) are higher than those obtained by Morales [57][58] for particle sizes of 5 nm, but the particle interactions are certainly different.

For bulk maghemite and magnetite, in theory, magnetization saturations of 77 emu/g and 82 emu/g at 5k are expected. The reduction of magnetization saturation in nanoparticles is a surface phenomenon. At the surface of magnetic materials, the spins are not as well oriented as observed in the interior, and this leads to a surface layer with very small magnetization saturation. As the surface/volume ratios of nanoparticles are larger by a few orders of magnitude than those of conventional materials, the contribution of spin disorder at the surface is important and causes a significant reduction in magnetization saturation [50].

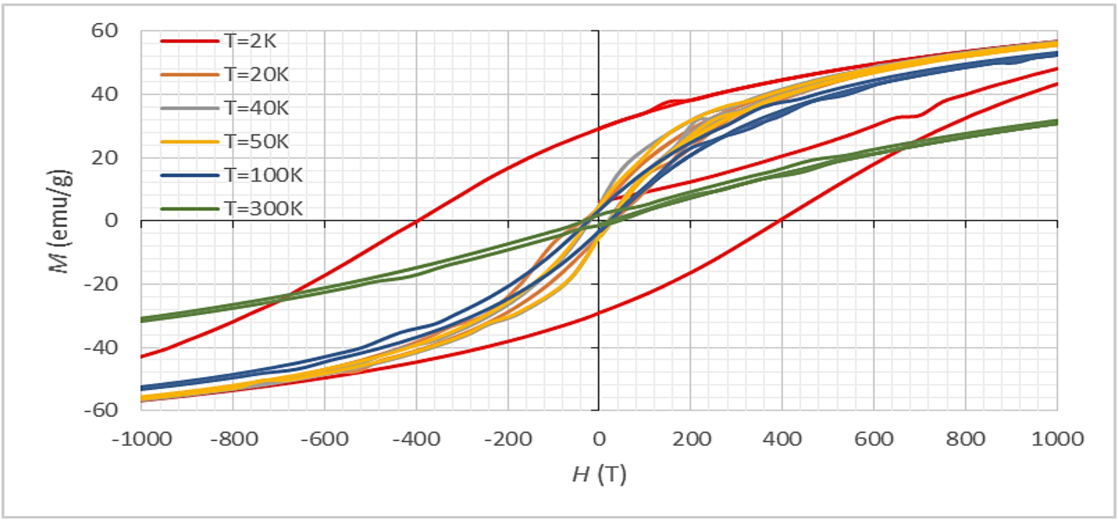

Figure 41. Details of hysteresis curves shown in Figure 39.

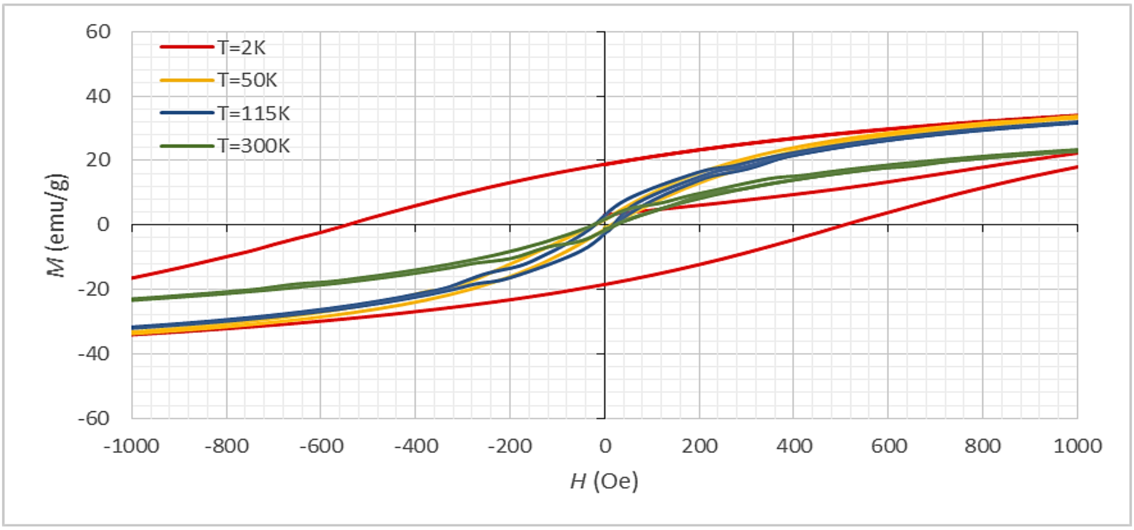

Figure 42. Details of hysteresis curves shown in Figure 40.

Figure 41 and 42 show that the hysteresis curves are not reversible and that interparticle interaction exists. For all temperatures, except for T=2 K, the superparamagnetic properties are apparent, being these characterized by a vanishing hysteresis. At T=2 K, the magnetization curves clearly show hysteresis. For these samples, the blocking temperature is clearly in the range between 100 K and 2 K, as seen in the Figures.

The coercive fields H_c are 392 Oe and 500 Oe for samples prepared by procedures A and A(2x), respectively. The remanent magnetization moment is about 30 emu/g for sample of procedure A and 18 emu/g for sample of procedure A(2x), also at 2K.

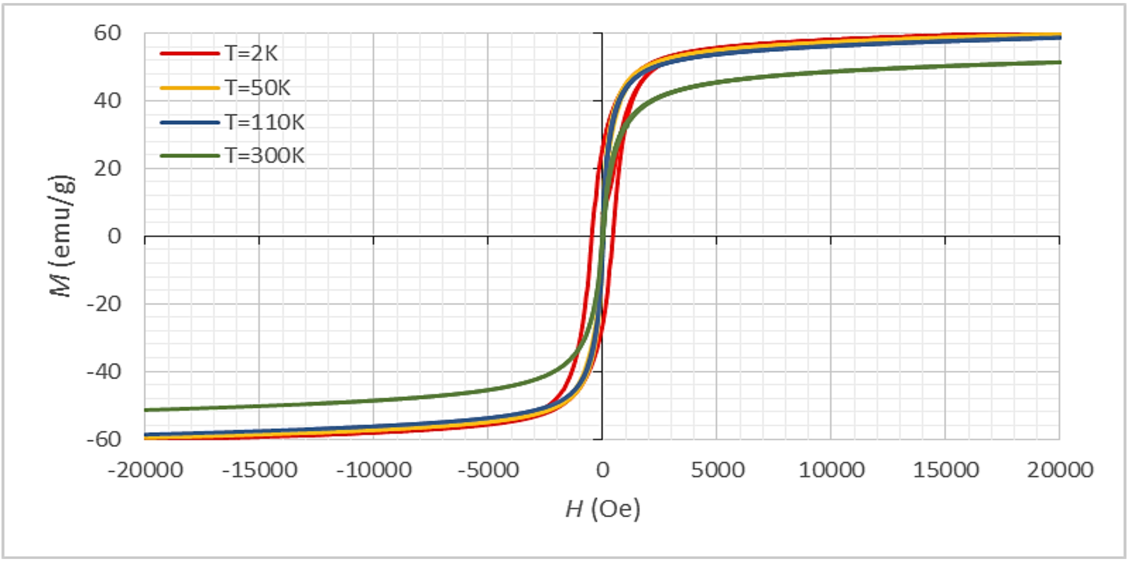

Figure 43. Magnetization as function of the applied field, for different temperatures - Sample C.

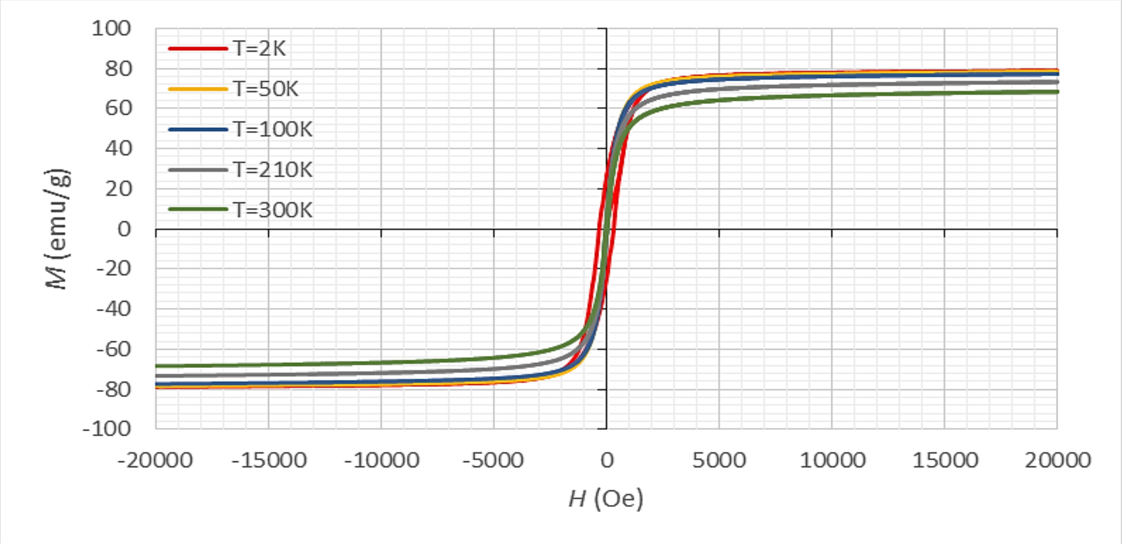

Figure 44. Magnetization as function of the applied field, for different temperatures - Sample C(2x).

In turn, for nanoparticles obtained from procedures C and C(2x), Figures 43 and 44 show a different magnetization saturation phenomenon from the ones presented in figures 39 and 40. Here, the magnetization saturation revealed itself to be higher for the sample prepared by procedure C(2x) when compared with the one prepared by procedure C. For sample C, at 300 K, the magnetization does not saturate till 20 kOe (Figure 43), but it seems lower than the one obtained for sample C(2x) (68 emu g^{-1} – Figure 44). At lower temperatures, the magnetization saturation of both samples increases and, for sample C(2x) (78 emu g^{-1}) the magnetization saturation continues to be higher than the "apparent" one of sample C. These obtained values for samples C and C(2x) continue to be slightly higher than those obtained by Morales [57][58], but as referred, our results are influenced by particle interactions.

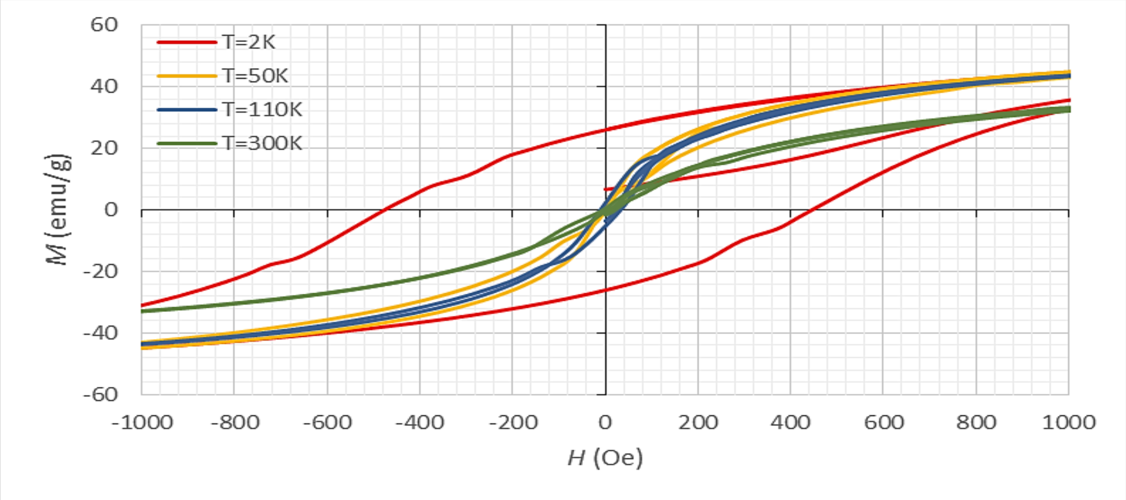

Figure 45. Details of hysteresis curves shown in Figure 43.

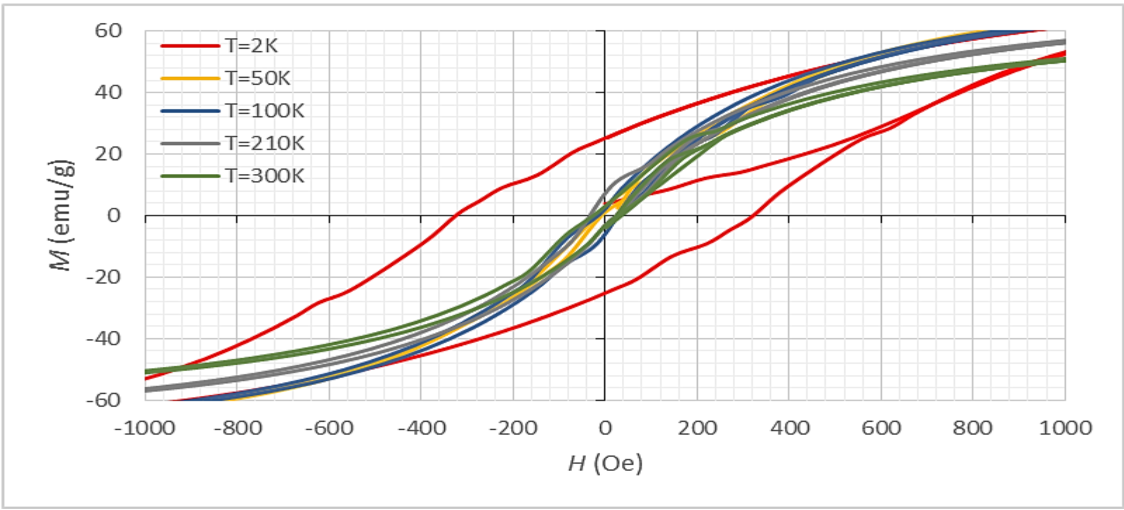

Figure 46. Details of hysteresis curves shown in Figure 44.

Figures 45 and 46 show that the hysteresis curves are also not reversible and that interparticle interaction exists for the samples produced by these two procedures. As in samples from procedures A and A(2x), with exception of T=2 K, for all the tested temperatures, the superparamagnetic properties of samples C and C(2x) are apparent, being these characterized by a vanishing hysteresis, while at T=2 K the magnetization curves clearly show hysteresis. The coercive fields for procedures C and C(2x) are 440 Oe and 320 Oe, respectively. The remanent magnetization moment is about 26 emu g^{-1} for procedure C, and 25 emu g^{-1} for procedure C(2x).

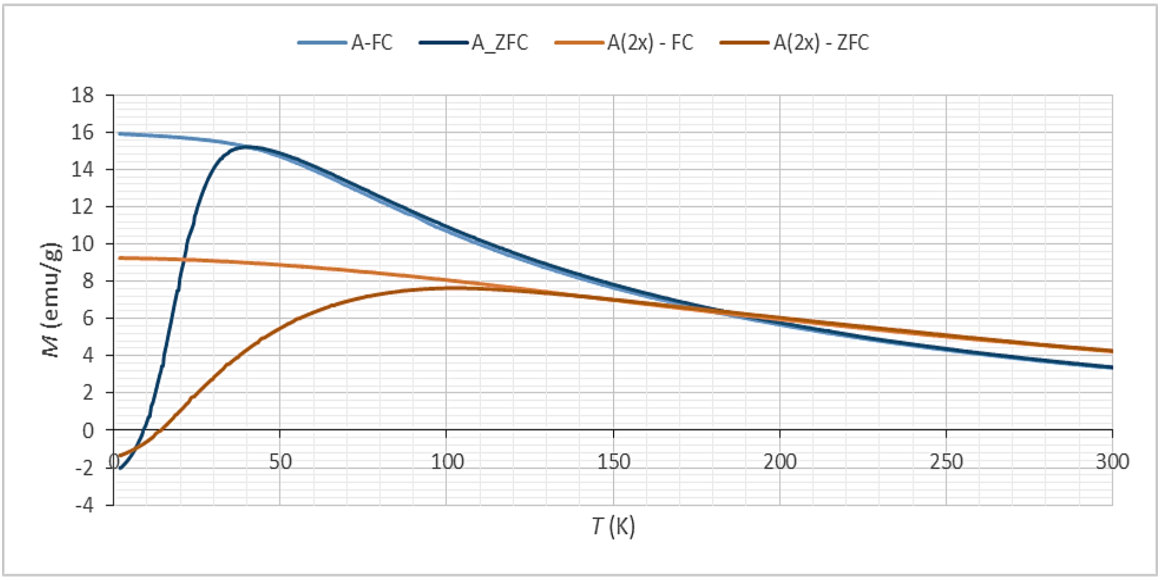

Figure 47. FC and ZFC curves of samples obtained from procedures A and A(2x), at H=100 Oe.

Field cooled (FC) and zero-field cooled (ZFC) magnetization curves of samples A and A(2x) were measured at 100 Oe as function of temperature, from 2 K to 300 K (Figure 47). From the analysis of these curves, we were able to calculate the blocking temperature for these samples, about 40.1 K and 102.3 K for procedures A and A(2x), respectively.

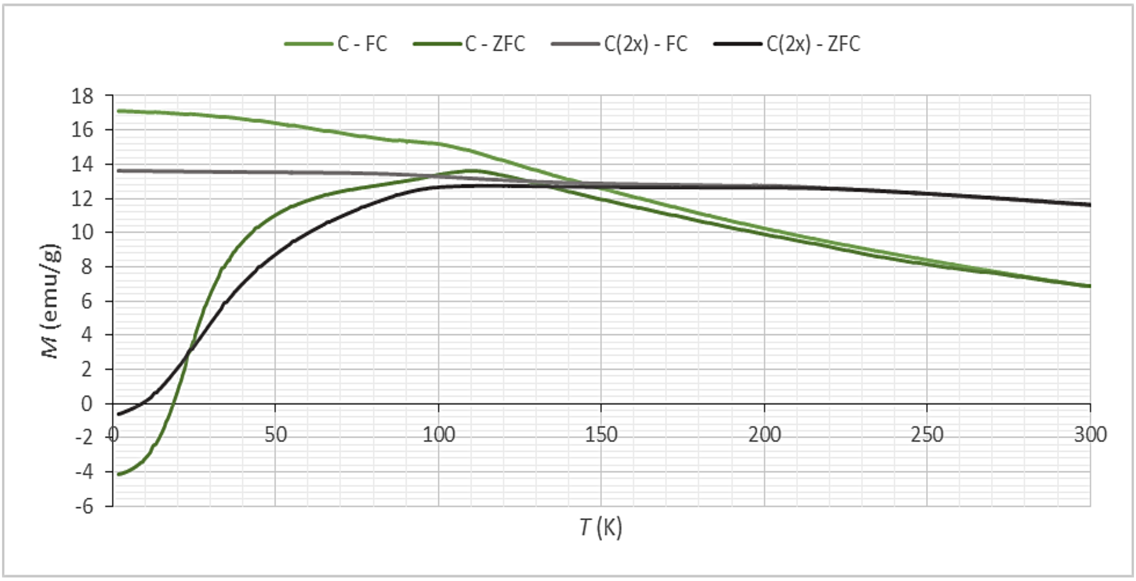

Figure 48. FC and ZFC curves of samples obtained from procedures C and C(2x), at H=100 Oe.

The same analysis was done from FC and ZFC curves of samples of procedures C and C(2x), measured in equal conditions to the ones of procedures A and A(2x). The blocking temperature is about 110.7 K and 116.0 K for samples by procedures C and C(2x), respectively.

ZFC curves shown in Figures 47 and 48 show negative remanent magnetization (NRM), which increase at lower applied fields (*e.g.* -4.12 and -5.60 emu g^{-1} were registered for sample C, at 50 and 100 Oe, respectively). The existence of NRM in homogeneous magnetic materials is still in debate, but recently a physical justification was given for homogeneous nanoparticles [59]. This justification applies a “wasp-waist” model in combination with energy calculations.

The temperature dependence shown for FC magnetization of samples A(2x) and C(2x) is weaker than that of the one observed from FC curves of A and C samples, indicating higher particle interaction in the samples produced by procedures where the amount of $Fe(acac)_3$ was doubled.

Considering Langvin’s law (eq. 21), the magnetic moment of superparamagnetic materials can be seen as a temperature independent function of H/T ratio. Therefore, plotting magnetization curves, at different temperatures over H/T ratio, provides a clear indication regarding the validity of Langvin’s function, thus confirms the existence of superparamagnetism. That analysis is shown in Figures 49, 50, 51 and 52.

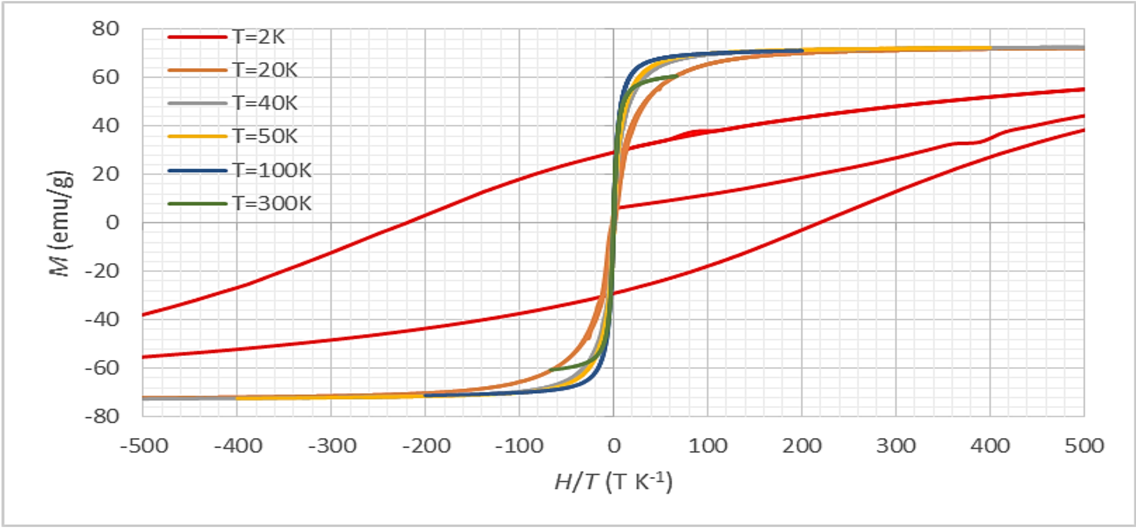

Figure 49. Magnetization, at different temperatures, as function of *H*/*T* ratios - Sample A.

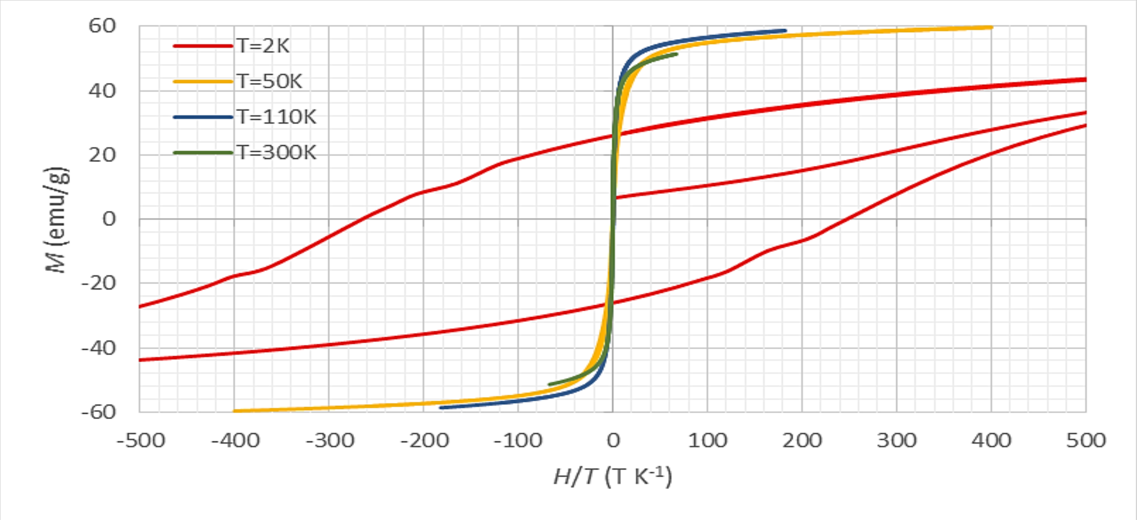

Figure 50. Magnetization, at different temperatures, as function of *H*/*T* ratios - Sample A(2x).

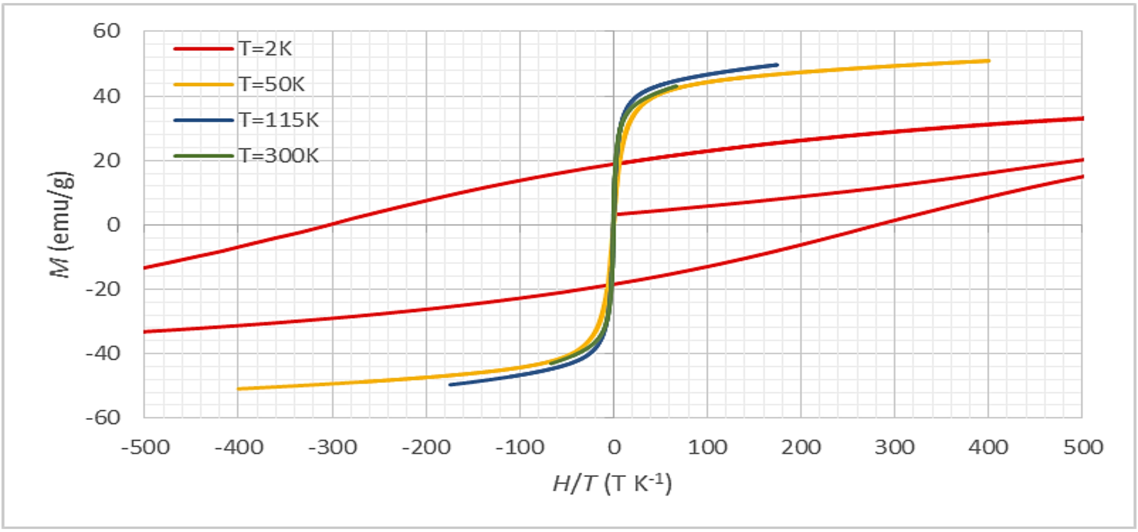

Figure 51. Magnetization, at different temperatures, as function of *H*/*T* ratios - Sample C.

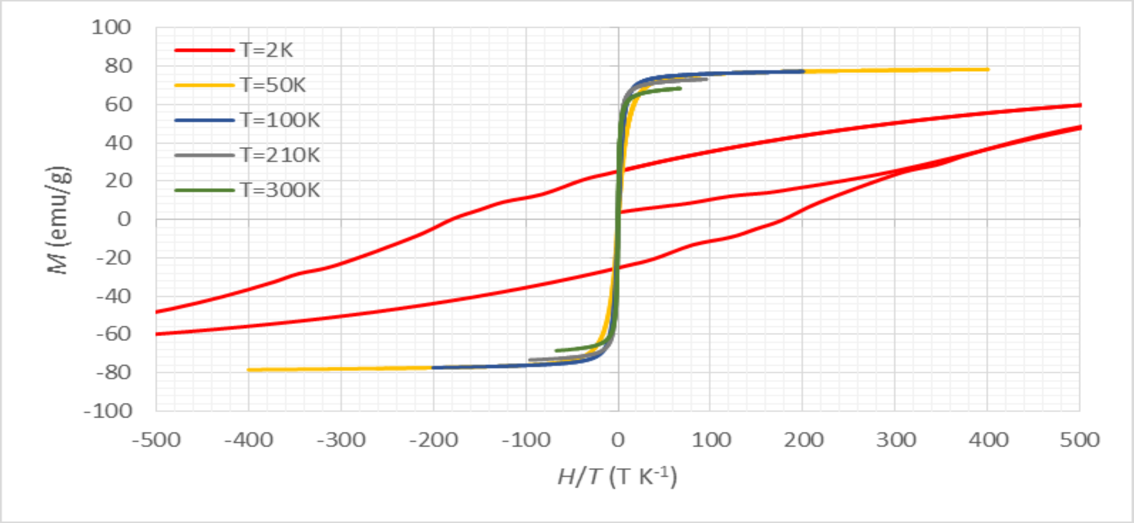

Figure 52. Magnetization, at different temperatures, as function of *H*/*T* ratios - Sample C(2x).

Figures 49, 50, 51 and 52 prove Langvin's law and, consequently, the existence of superparamagnetic behaviour for all of the tested samples and temperatures, with exception for T=2 K, where the magnetic moment of the samples cannot be regarded as temperature independent in relation to the H/T ratio. From the analysis of Figure 49, for T=20 K, it is visible a loss of superparamagnetic behaviour by the particles, attributed to the deviance from the curves for other temperatures.

After measuring different size properties of the produced nanoparticles as well as their magnetic, phase and shape properties, a better understanding of the chemical structure of the coating is needed. That knowledge was obtained by performing a FTIR analysis on the synthesized samples of the procedures A, A(2x), C and C(2x). The obtained spectra are shown in Figure 53.

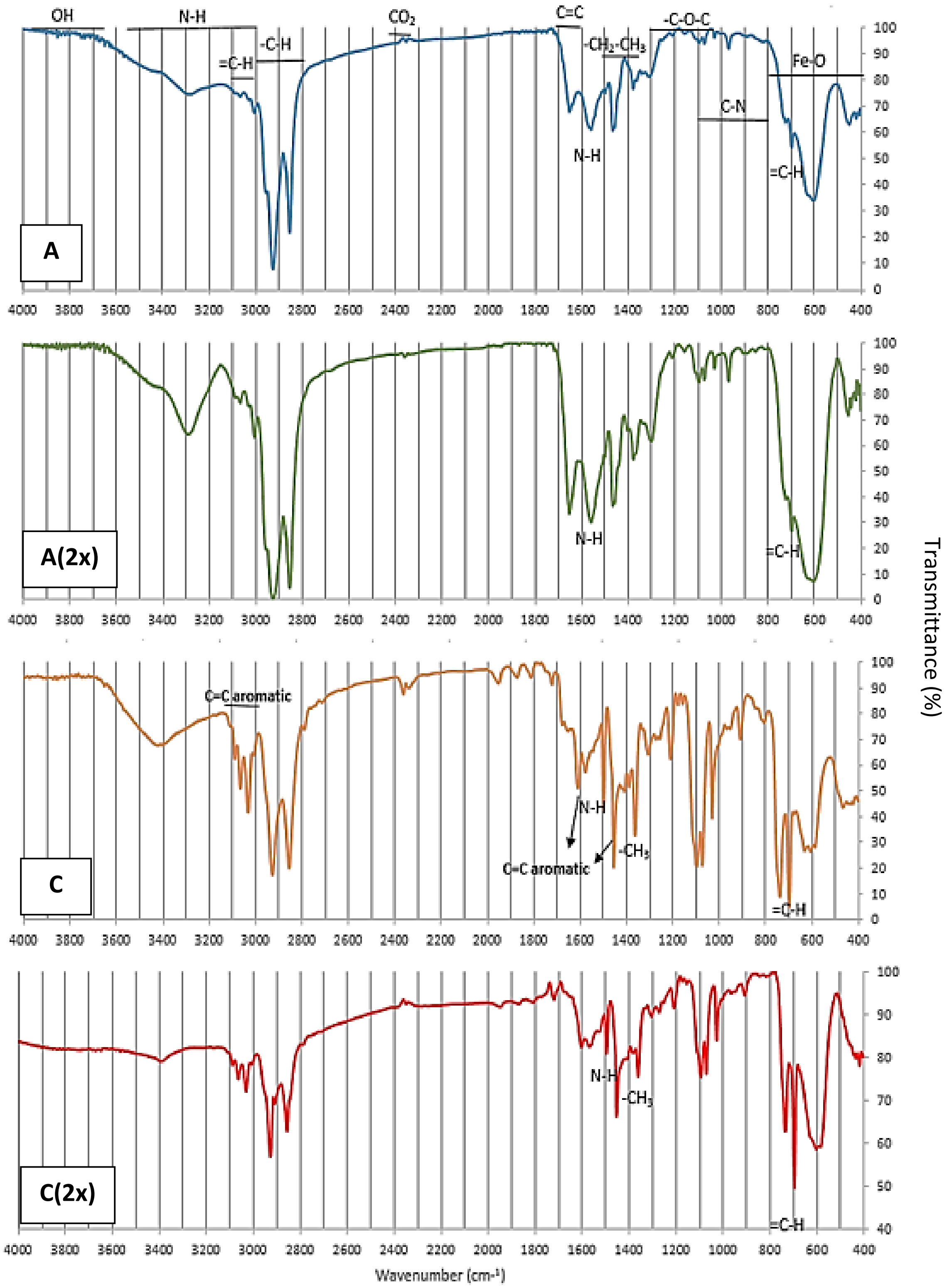

Figure 53. FTIR spectra obtained for the samples of procedures A, A(2x), C and C(2x), respectively.

Even though the four procedures of the synthesis of nanoparticles used the same reactants, the coating of nanoparticles might be affected by the different amount of each (Figure 53). The spectra baseline hardly recovers back after achieving a peak due to the broad bands characteristic of amine groups (being difficult the identification of other chemical bonds in that wavenumber band), which strongly confirms the oleylamine presence in the samples. The spectra of the samples from the procedures C and C(2x) differs from the spectra acquired for samples A and A(2x), due to the overwhelming presence of benzyl ether (3100-3000 cm^{-1}, 2000-1800 cm^{-1}, 1300-1020 cm^{-1} and the peaks displayed in Figure 53 as C=C aromatic), which dominates great part of the spectra. All the characteristic vibrations from this compound often create peaks of higher intensity or slight deviations from where those peaks were expected to be.

Despite the presence of the spectra peaks related to the N-H bonds (typical of oleylamine) in all samples, the spectra of samples from procedures A and A(2x) display fewer and smoother peaks, related to the benzyl ether bonds, barely suggesting the presence of this compound, contrary to what is seen in samples C and C(2x). This fact confirms what was expected, since these last samples used a smaller amount of benzyl ether and a higher of oleylamine during their synthesis. It allows to conclude as well that the coating in procedures A and A(2x) is rather simple and only being composed of oleylamine. However, samples form procedure C and C(2x) have a more complex coating. Its IR spectra suggests an interaction between oleylamine and benzyl ether to form the coating of the nanoparticles. Therefore, these specific amounts of reactants seem to favour the anchoring of the benzyl ether molecules in the coating.

The spectrum of magnetite has broads at 580 and 400 cm^{-1}, while the spectrum of maghemite shows broad bands at 700, 640-660, 620, 580, 560, 460 and 430 cm^{-1}. In spite of the Fe-O bond at 580 cm^{-1} is shown in all obtained spectra, which strongly confirms the presence of magnetite and/or maghemite, the distinction between maghemite and magnetite is difficult to evaluate due to the slight deviation of the peaks, when comparing with the reference. Despite this fact, all spectra suggest the existence of maghemite in the produced nanoparticles.

By this point, size, shape, phase and magnetic properties, as well as the chemical structure of coating of the produced iron oxide nanoparticles were assessed. They revealed us that, although they have a larger size distribution, a lower coercive field and more particle interactions, samples prepared by procedure C(2x) are mainly composed by magnetite (Mössbauer and XRD results) and have the highest increase in size (XRD, DLS and TEM results), highest magnetization saturation (VSM results), with a oleylamine and benzyl ether coating. Therefore, procedure C(2x) was the one chosen to continue the further studies of dispersion stability, cytotoxicity and proteins adsorption analysis, since it revealed itself the most promising one to synthesize high quality, size controlled superparamagnetic iron oxide nanoparticles (SPIONS). This analysis will also be done to samples of procedure C just to provide a comparison basis.

5. Discussion of results for SPIONs application – Biological Aspects

In this chapter we will describe and discuss the results of the influence of surfactant on SPION stability in water dispersions, the SPION cytotoxicity, as well as the protein adsorption efficacy using SPIONs as the adsorbent matrix.

5.1. Influence of surfactant on superparamagnetic iron oxide nanoparticle stability in water dispersions

Owing to chemical nature of the SPIONs, a stable aqueous suspension is not possible to obtain with further development. On the other hand, a water-based SPION suspension is preferred in order to evaluate both, *in vitr*o and *in vivo* biological SPION properties. With the aim to obtain aqueous stable suspensions, two different compounds with surfactant properties were tested: bovine serum albumin (BSA) and polysorbate 80 (Tween 80). As it was described in section 3.3., several concentrations of the surfactant compounds were previous dissolved in phosphate buffer saline (PBS) solution (from 1% to 3% for BSA and1% to 5% for Tween 80) , being these mixtures used as the SPION's re-dispersion solvents. The aim was to determine which surfactant solution and whose concentration permits longer and more physical stability of the Fe_3O_4 nanoparticles suspension.

With this intention, the stored solutions of Fe_3O_4 nanoparticles were dried in cuvettes and the different surfactant mixtures were added. An ultrasonic bath was applied to homogenize those suspensions. After 8 h rest period, the transmittance of the suspensions was directly measured in the UV-Vis spectrometer. Additionally, two controls were made without surfactant, being only composed by nanoparticles in PBS. One of them was also subjected to the rest period (Control 1) and, the other was thoroughly mixed before measuring its transmittance (Control 2).

The transmittance value of the Control 1 represents normal stability (without surfactant) of the nanoparticles in PBS, after the rest period, while the transmittance of the Control 2 corresponds to the potential maximum value of the stability of the nanoparticles in suspension. Therefore, the higher values of the transmittances of the samples measured were matched to poor results of stability of the nanoparticles in suspensions.

The results of UV-VIS spectroscopy were obtained after an 8 h period of rest of the SPIONs re-dispersions, displayed in the Figure 54.a) and 54.b). By the analysis of Figures 54.a) and 54.b), a wavelength of 500 nm can easily distinguish the obtained results, before reaches the transmittance threshold. Figure 54.C shows the obtained average results and respective standard deviation for all re-dispersion solvents used at a wavelength of 500 nm.

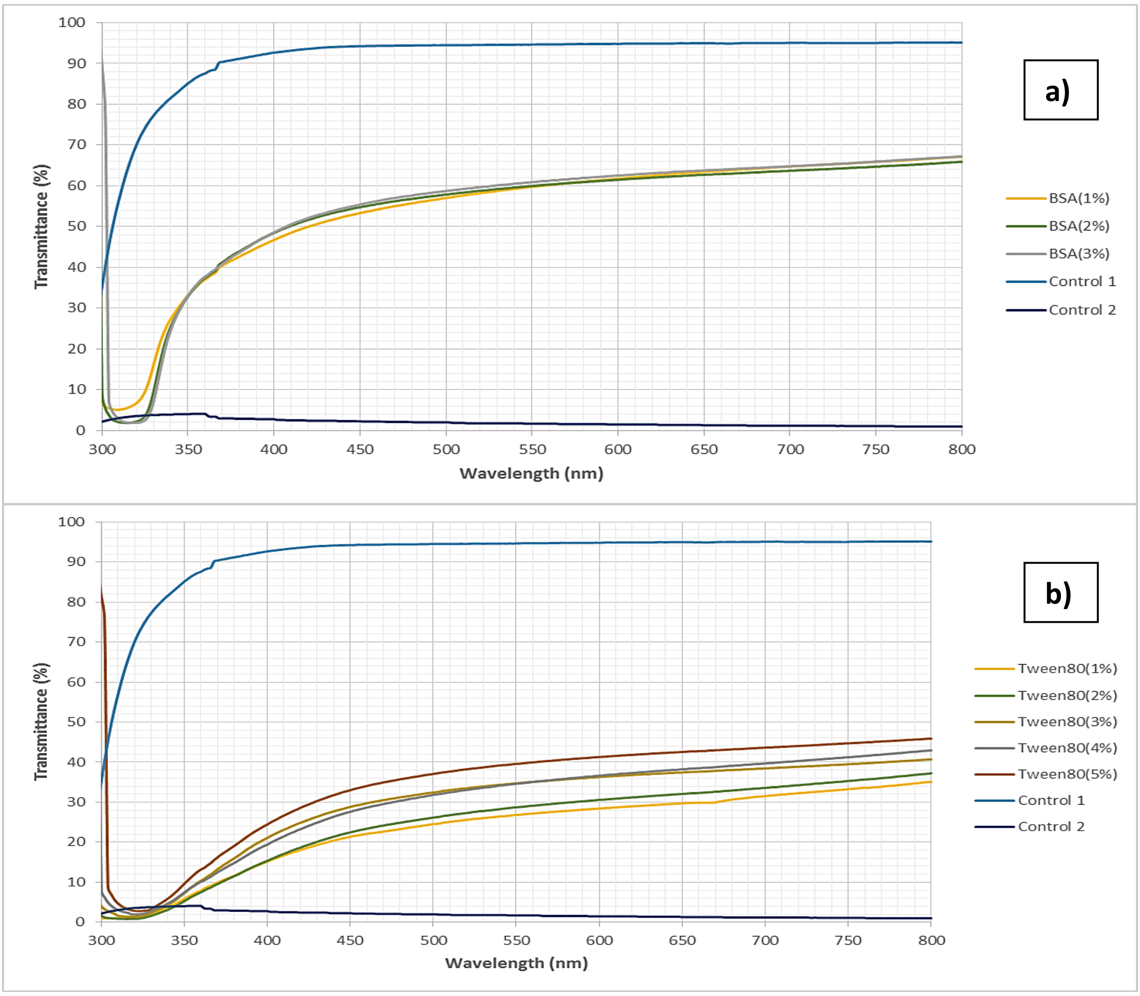

		% Transmittance (500nm) Mean	Standard Deviation
Control 1		94.5	0.1
Control 2		2.00	0.1
Tween80	5%	37.1	0.4
	4%	31.9	0.1
	3%	32.4	0.1
	2%	26.2	0.1
	1%	24.5	1.2
BSA	3%	58.8	0.2
	2%	57.9	0.2
	1%	57.0	0.2

c)

Figure 54. UV-Vis results for samples obtained by procedure C(2x) re-dispersed in PBS and mixtures of BSA (a)) and Tween 80 (b)) in PBS in different concentrations. The transmittance results of all samples for a wavelength of 500 nm are also presented(c)).

The analysis of Figure 54.a) demonstrates that the presence of BSA in PBS solutions decreases the percentage of transmittance when compared with the PBS solution alone. This ultimately indicates that in fact BSA increases the stability of SPIONs in cell solutions. Of note, the insignificant influence of BSA concentration in the percentage of transmittance – showed in Figure 54.c) - and, consequently, in the stability of dispersions.

The presence of Tween 80 in PBS solutions also reduces the percentage of transmittance from the PBS solution standalone, improving the stability of SPIONs. Moreover, by analysing Figure 54.b) and c), it seems that a minor concentration of Tween 80 is beneficial for that stabilization to occur. If we now compare the two surfactants, Tween 80 presents higher capacity to improve the stabilization of the prepared nanoparticles in water and cell solutions, due to the lower percentage of transmittance registered.

Thus, during the planning of the procedures for the remaining SPIONs characterization that concept was taken into account and small amounts of Tween 80 were used to improve the results of these analysis.

5.2. Evaluation of the iron oxide nanoparticle cytotoxicity

Testing the effect of compounds on the viability of cell grown in culture is widely used as a predictor of potential toxic effects in whole animals. The MTT assays is a colorimetric assay and allows the determination of the cell viability through the direct measurement of the cell enzymatic metabolic activity. In order to perform cytotoxic tests of the synthesized nanoparticles, an improvement of the protocol was necessary.

With this intuit, different concentrations of nanoparticles dispersed in medium of culture (DMEM) - from 0.975 to 2000 µg/ml, were added to cos-7 adherent cells, already seeded in a 96-well plate in DMEM. After a day of incubation, the MTT in PBS (pH=7.4) was added to each well and incubated for more 2 h at 37 °C. Then, the medium was removed and formazan crystals produced by metabolic active cells were solubilized with the addition of DMSO in each well. Then, a centrifugation was performed to precipitate the nanoparticles and the optical density (OD) of the supernatant was measured at 540 nm with 630 nm as wavelength reference. The measurement of the optical density (OD) allowed the determination of the cell viability (%) (see eq. 18) for each concentration of nanoparticles.

Figures 55 illustrates the cytotoxic effect of the prepared SPIONs through a representation of the percentage of cell viability as function of the logarithm of the several concentrations – in µg/ml – of nanoparticles that were in contact with cos-7 cells. These figures also show the best fitting to the curve of results, as well as the IC_{50} (the concentration needed for 50% of the cells to die) for nanoparticles obtained by procedures C and C(2x).

The IC_{50} was calculated by solving the polynomial equation of the curve that best fits the results (see Table 14.). By solving the 6th degree polynomial equations, the calculated IC_{50} is 303.92 µg/ml for samples of procedure C and 759.07 µg/ml for samples of procedure C(2x). These particular results show a less cytotoxic effect for samples originated by procedure C(2x).

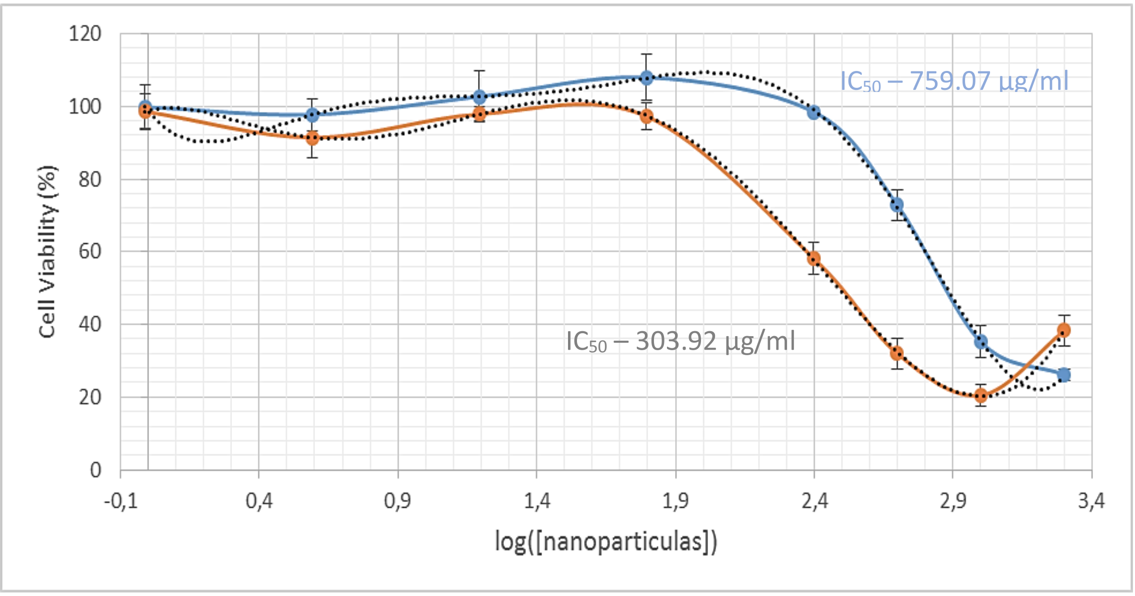

Figure 55. Viability of cos-7 cells as function of the logarithm of the concentration of nanoparticles prepared by procedures C (red) and C(2x) (blue).

Table 14. Parameters of the curve that fits the results for samples produced by both procedures (equation, R^2 and the result of IC_{50}).

Sample	Polynomial Equation	R^2	IC_{50} (µg/ml)
C	$y = -2.4218x^6 + 30.88x^5 – 132.15x^4 + 228.61x^3 – 149.4x^2 + 19.646x + 98.825$	0.9999	303.92
C(2x)	$y = 8.856x^6 – 81.669x^5 + 280.11x^4 – 449.9x^3 + 341x^2 – 94.678x + 98.754$		759.07

5.3. Evaluation of BSA and α-casein adsorption efficacy

Since the main focus of this work is to apply this system for located drug-delivery, the measurement of the surface charge of the prepared nanoparticles was needed to understand to which protein we could apply the adsorption procedure and how strong would be the interaction between protein and nanoparticles.

Therefore, the Fe_3O_4 nanoparticles dispersed in PBS (6.66 mg/ml) were re-dispersed in several biocompatible solutions with different pH (water, PBS and acetate buffer with pH=5 and pH=3.6) using a dilution factor of 10 (100 µl:1 ml). The Zeta potential of these re-dispersions was determined and the average values are displayed in Table 15.

Table 15. Zeta Potential results for nanoparticles re-dispersed in solutions with different pH.

Type of suspension	$\overline{Zeta\ Potential}$ **(mV)**	$\sigma(\overline{Zeta\ Potential})$ **(mV)**
Water : Nanoparticles in PBS (1ml:100µl)	7.776	0.527
PBS : Nanoparticles in PBS (1ml:100µl)	-3.148	0.326
Acetate Buffer (pH=3,6) : Nanoparticles in PBS (1ml:100µl)	14.282	1.982
Acetate Buffer (pH=5,0) : Nanoparticles in PBS (1ml:100µl)	8.140	0.962

Thus, water and acetate buffer with a pH=5.0 were the re-dispersive solutions selected to employ during the protein adsorption tests. Although the surface charge of the produced nanoparticles is not as high as in the other acetate buffer, and because the interactions between nanoparticles and the proteins could be weak, their pH does not varies from the physiological pH of brain as when acetate buffer with pH=3.6 was used.

Bovine serum albumin (BSA) and α-casein were chosen as the proteins for adsorption tests, since they have isoelectric points (4.7 and 4.2-4.7, respectively) similar to the pH of the buffers selected. For brain therapeutic purposes, these proteins have no particular applications; however, they served as model of therapeutic proteins. The two used properties – loading efficiency and capacity (see eq. 19 and 20), evaluate the efficiency of bonding between the protein and the nanoparticles (relates the mass of protein attached to nanoparticles and to the initial mass of protein used) and the capacity of nanoparticles to attach protein to their surface (relates the mass of protein bond to the nanoparticles and the mass of nanoparticles employed), respectively.

With this aim, nanoparticles were suspended (1 mg/ml) in water or acetate buffer and they were mixed in same extents with protein solutions comprising several concentrations from 25 to 700 µg/ml for 0.5 h. Subsequently, a centrifugation process was applied in order to remove the supernatant. Finally, the non-adsorbed protein was quantified by implementing a colorimetric procedure - Lowry protocol (see section 3.5.11.).

The results of measuring the proteins loading efficiency and the loading capacity of the nanoparticles prepared from procedures C and C(2x), as function of the initial concentration of BSA mixed with nanoparticles is shown in Figures 56 and 57, respectively.

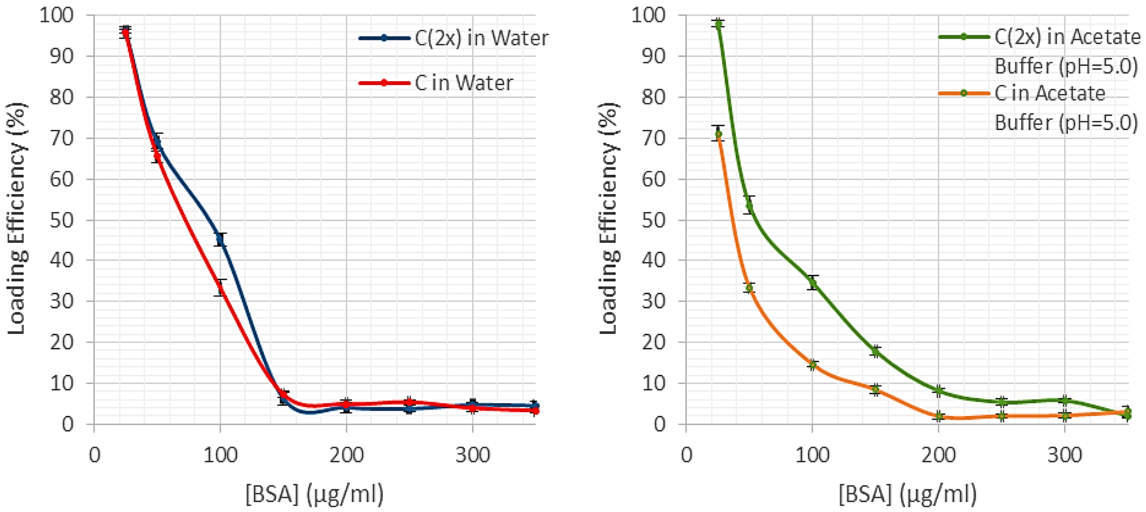

Figure 56. Obtained loading efficiency (%) as function of the concentration of BSA (µg/ml) using Water (left) and Acetate buffer of pH=5.0 (right) as the SPIONs re-dispersive solutions.

The analysis of Figure 56 revealed a higher loading efficiency (%) for lower concentrations of BSA. Moreover, BSA has greater loading efficiency with nanoparticles prepared by procedure C(2x) when 50 ≤ [BSA] ≤ 150 µg/ml with water used as the solution where both samples of nanoparticle were suspended. Regardless of the concentration of BSA, when acetate buffer was employed the loading efficiency of BSA was significantly higher for samples of nanoparticles produced from procedure C(2x).

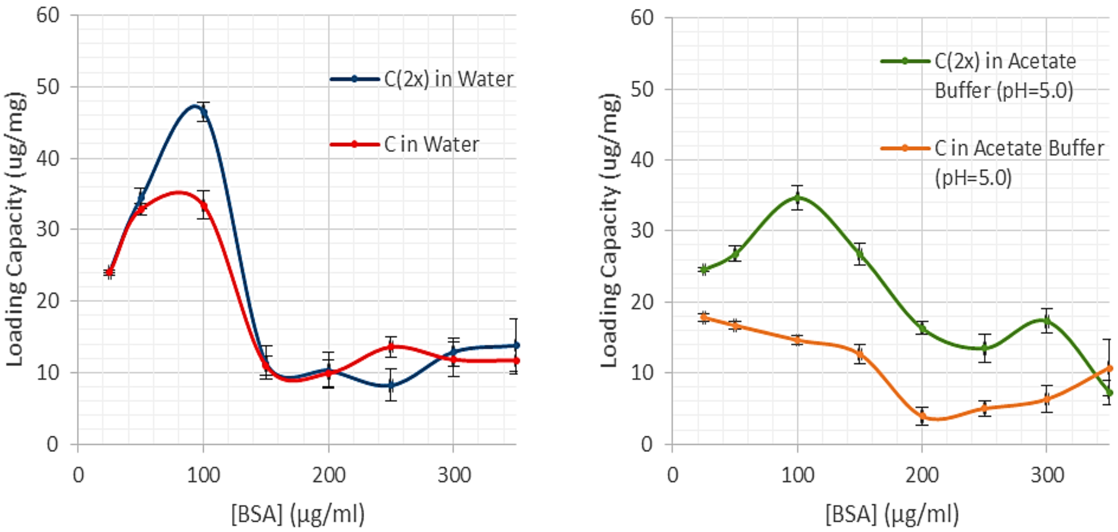

Figure 57. Obtained loading capacity (%) as function of the concentration of BSA (µg/ml) using Water (left) and Acetate buffer of pH=5.0 (right) as the SPIONs re-dispersive solutions.

As for loading efficiency, nanoparticles of procedure C(2x) have greater loading capacity (Figure 57) when 50 ≤ [BSA] ≤ 150 µg/ml with water used as the solution where both samples of nanoparticles were suspended. The observed peak for 100 µg/ml of BSA for nanoparticles prepared by procedure C(2x) re-dispersed in water could be related to an increase in interactions between BSA molecules attached to the SPIONs and free BSA molecules of each solution or can be related to the possibility of having distinct amount of nanoparticles with different sizes in each sample. When acetate buffer was used, the loading capacity of nanoparticles of procedure C shows constantly lower that the one produced by procedure C(2x), regardless of the BSA concentration. These results demonstrate that the nanoparticles synthesized from procedure C(2x) are the most suitable to adsorb BSA and to potentially be used as nano-carriers for drug delivery systems to be applied for brain therapeutic purposes.

The assessment about the type of the used re-dispersant solutions can be obtained when a single type of nanoparticles is highlighted. The results for loading efficiency and capacity related to the concentration of BSA for nanoparticles by procedure C(2x) are displayed in Figure 58.

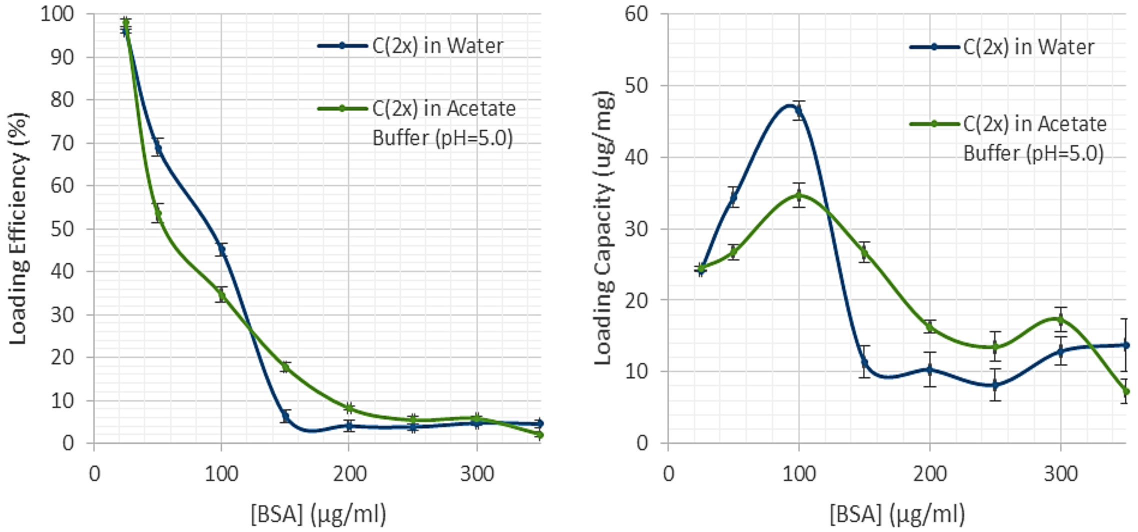

Figure 58. Obtained loading efficiency (left) and capacity (right) as function of the concentration of BSA (µg/ml) for nanoparticles of procedure C(2x).

According to Figure 58, there is a dependence relation between the loading efficiency/capacity and the two used re-dispersant solutions. As a result, for low concentrations of BSA (25 ≤ [BSA] ≤ 125 µg/ml), both calculated loading efficiency and loading capacity are higher when water is used but, beyond concentrations of 125 µg/ml of BSA, these adsorption properties are enhanced when acetate buffer (pH=5) was employed.

When the same method was used to evaluate the properties of α-casein adsorption, the protein did not dissolve in both of the re-dispersant solutions employed. Therefore, when the centrifugation process was performed, almost all of the protein precipitated, giving us variable and inaccurate results about the amount of protein adsorbed by the prepared Fe_3O_4 nanoparticles. From this analysis is possible to conclude that, when selecting a biocompatible re-dispersant solution, it must completely dissolve the protein of interest.

For brain treatment purposes another protein should be chosen but, its adsorption profile may not be the same and the solution where nanoparticles are suspended must be also carefully selected. Nevertheless, it became proved that the protein adsorption by the prepared nanoparticles can be enhanced with a proper selection between the re-dispersant solution and the drug/protein concentration.

6. Conclusions and Future Work

In the present work, we studied several aspects on how to achieve the best possible biodegradable magnetic system for targeted drug delivery in the brain. In order to this, we followed the procedure described by Xu *et al.* [45], where oleylamine acted as both a reducing agent and a stabilizer to produce SPIONs – procedure A.

To better understand the influence of oleylamine and benzyl ether in the synthesis reaction and in the characteristics of nanoparticles, procedures B and C were designed by changing the ratio between the amounts of these two reactants.

Since the initial aim was to increase the average size of nanoparticles produced by Xu to assure their passage through the blood-brain barrier, three more synthesis procedures were additionally defined by extending the time of the nanocrystals growth by one hour (procedures A*, B* and C*). The samples from these procedures were characterized through XRD and DLS and the results compared with those obtained for their native procedures (A, B and C).

XRD and DLS results for the samples of procedures A*, B* and C* didn't reveal the desired increase of nanoparticles size and amount of magnetite. Besides that, we have concluded that increasing the time of growth of nanocrystals may have an agglomerative effect during its synthesis. The agglomeration of nanoparticles enhances their toxic effect and, theoretically, reduces the drug absorption as the area/volume ratio is decreased.

Next, and using procedures A, B and C methods as basis, we developed a procedure where the previously prepared nanoparticles were used as seeds or points of nucleation for the next nanoparticles synthesis, hoping that the new iron(III) acetylacetonate was only used in the nanocrystals growth– procedures A+A, B+B and C+C.

The XRD results showed a general increase of the amount of magnetite and of the average crystallite size but, from DLS and TEM results, we concluded that not all of the previous used nanoparticles acted as points of nucleation for the next synthesis, being created more nucleation points with the added $Fe(acac)_3$. Thus, few new nanoparticles were created, similar to the first ones and other particles grew or suffered agglomeration.

At this point, procedure B and all resulting from this one were discarded due their intermedium conditions of reactants, which always led to results in between the other two procedures.

After, we focused on the study of the influence of doubling the amount of precursor, iron(III) acetylacetonate, taking the basis of procedures A and C. Since XRD lattice parameter, TEM and DLS results were consistent and showed a significant growth of nanoparticles, and, additionally, Mössbauer and XRD results proved to have an increase of the amount of magnetite between the samples in which the precursor was doubled – A(2x) and C(2x) –when compared to the samples produced by their native procedures, a further magnetic and coating characterization was applied.

VSM results presented a higher magnetization saturation for procedure A when comparing with procedure A(2x). However, the opposite was found for C and C(2x), where C(2x) had higher magnetization saturation than C. They also showed the highest coercive field for sample A(2x) and the lowest for C(2x), being the remanent magnetization approximately similar for samples of both procedures.

Although non-reversibility was found in the hysteresis curve in the VSM, as well as higher values of magnetization saturation when comparing to the references for maghemite and magnetite (which indicates the existence of particle interactions), TEM results revealed well dispersed nanoparticles.

FTIR analysis lead us to conclude that the coating in samples from procedures A, A(2x) and C(2x) is rather simple and only being composed of oleylamine. However, procedure C has a more complex coating. Its IR spectra suggests an interaction between oleylamine and benzyl ether to form the coating of nanoparticles.

Thus, and although samples of procedure C(2x) had a larger size distribution, a lower coercive field and more particle interactions, they were mainly composed of magnetite (Mössbauer and XRD results) and had the highest increase in size (XRD, DLS and TEM results), highest magnetization saturation (VSM results), with a simple oleylamine coating, making this the elected procedure to pursuit our work.

One of the purposes of this work was to stabilize the SPIONs in water allowing them to be applied in future human brain cells treatment. Therefore, Tween 80 and BSA were tested as surfactants, mixing them in different concentrations with a PBS solution, and being these mixtures used as the SPION's re-dispersion solvents.

UV-Vis results revealed that both surfactants improved the stability of SPIONs. Moreover, the highest capacity to increase the stabilization of the prepared nanoparticles in water and cell culture medium was found for small concentrations of Tween 80. Thus, this concept was taken into account and small amounts of Tween 80 were used to improve the results of cytotoxicity and proteins' adsorption analysis.

Cytotoxicity tests performed on the nanoparticles synthesized by procedures C and C(2x) revealed an IC_{50} of 303.917 µg/ml and 759.071 µg/ml, respectively, with cos-7 cells. The results elucidate us about the lower toxic effect of nanoparticles produced from procedure C(2x).

Finally, the surface charge of the prepared nanoparticles dispersed in different solutions was evaluated and it showed that water and acetate buffer with a pH=5.0 were suitable solutions, capable to enhance the surface charge of the nanoparticles. Although their surface charge is not as high as in the acetate buffer with pH=3.6, and because of the interactions between the proteins and nanoparticles could be weaker, the pH=5 is more close to the physiological pH of brain, potentially allowing a normal function and behaviour of this organ.

Despite they have no declared effect in brain treatments, BSA and α-casein were chosen as the model proteins for testing adsorption on the nanoparticles, since they have an isoelectric point similar to the pH of the buffers selected. After promoting the protein adsorption, the obtained results from the application of Lowry protocol, for quantification of protein, indicated higher values of loading efficiency of BSA and loading capacity of nanoparticles for smaller concentrations of BSA (50 ≤ [BSA] ≤ 150 µg/ml) when water was used as an re-dispersant solution. When acetate buffer was employed, the loading efficiency of BSA and the loading capacity of nanoparticles from procedure C were always lower than for the nanoparticles produced by procedure C(2x), regardless of the BSA concentration.

Regarding the of the solution used, the results showed that for low concentrations of BSA (25 ≤ [BSA] ≤ 125 µg/ml) both calculated loading efficiency and loading capacity are higher when water was used but, beyond concentrations of 125 µg/ml of BSA, these adsorption properties are enhanced with acetate buffer (pH=5).

When the same method was employed to evaluate the properties of α-casein adsorption, the protein did not dissolve in both of the re-dispersant solutions.

Therefore, it gave us variable and inaccurate results of the amount of protein adsorbed by the prepared Fe_3O_4 nanoparticles. From this analysis, it was possible to conclude that, when selecting a biocompatible re-dispersant solution to enhance the surface charge of nanoparticles, it must completely dissolve the protein of interest.

Concluding, it is of our understanding that a biodegradable magnetic nano-carrier for drug delivery in brain can be assembled by using a therapeutic protein and the iron oxide nanoparticles synthesized in this work. The relatively narrow size distribution, the low toxicity of the nanoparticles and a proper selection of the re-dispersant solution and protein concentration can constitute a novel route to develop therapeutic treatment in brain.

There are still some questions that were brought up during the course of this work and can be vectors for future work. One possible effort is to improve the study made by VSM and Mössbauer, by using iron oxide nanoparticles with the stabilizing coating – Tween 80 – and with the protein adsorbed. This would give us a better insight into the magnetic properties of the overall drug delivery system instead of the nanoparticles by themselves.

Another possible exertion is to improve the study about the protein adsorption by using a known brain's therapeutic protein and a re-dispersant solution that takes into account the proteins characteristics and brain's physiological conditions.

The forces related to the protein adsorption on the produced SPIONs could also be evaluated by resorting to Atomic Force Microscopy (AFM) tests.

At last, a complete in vivo test could be done to determine the drug releasing kinetics and, consequently, evaluating the efficiency of this developed technology.

7. References

[1] P. Poizot, S. Laruelle, S. Grugeon, L. Dupont, J.M. Tarascon, *Nano-sized transitionmetaloxides as negative-electrode materials for lithium-ion batteries*, Nature, 407(6803) (2000) 496–499.

[2] A. Tari, R.W. Chantrell, S.W. Charles, J. Popplewell, *Magnetic-properties and stability of a ferrofluid containing Fe_3O_4 particles*, Physica B & C, 97 (1) (1979) 57–64.

[3] M. Mahmoudi, A. Simchi, M. Imani, P. Stroeve, A. Sohrabi, *Templated growth of superparamagnetic iron oxide nanoparticles by temperature programming in the presence of poly(vinyl alcohol)*, Thin Solid Films, 518 (15) (2010) 4281–4289.

[4] Lu, A.H., Salabas, E.L., & Schüth, F., *Magnetic nanoparticles: synthesis, protection, functionalization, and application*. Angewandte Chemie International Edition, 46 (8) (2007) 1222-1244.

[5] M.W. Freeman, A. Arrott, J.H.L. Watson, *Magnetism in medicine*, Journal of Applied Physics, 31 (5) (1960) 404–405.

[6] C. Alexiou, W. Arnold, R.J. Klein, F.G. Parak, P. Hulin, C. Bergemann, W. Erhardt, S. Wagenpfeil, A.S. Lubbe, *Locoregional cancer treatment with magnetic drug targeting*, Cancer Research 60 (23) (2000) 6641–6648.

[7] A. Senyei, K. Widder, G. Czerlinski, *Magnetic guidance of drug-carrying microspheres*, Journal of Applied Physics, 49 (6) (1978) 3578–3583.

[8] K. Mosbach, U. Schroder, *Preparation and application of magnetic polymers for targeting of drugs*, FEBS Letters, 102 (1) (1979) 112–116.

[9] K.J. Widder, A.E. Senyei, D.G. Scarpelli, *Magnetic microspheres — model system for site specific drug delivery in vivo*, Proceedings of the Society for Experimental Biology and Medicine, 158 (2) (1978) 141–146.

[10] O. Veisegh, J. Gunn, M. Zhang, *Design and fabrication of magnetic nanoparticles for target drug delivery and imaging*, Advanced Drug Delivery Reviews, 60 (3) (2010) 284-304.

[11] P. Tartaj, C.J. Serna, *Synthesis of monodisperse superparamagnetic Fe/silica nanospherical composites*, Journal of the American Chemical Society, 125 (51) (2003) 15754–15755.

[12] J. Lodhia, G. Mandarano, N.J. Ferris, P. Eu, S.F. Cowell, *Development and use of iron oxide nanoparticles (Part 1): Synthesis of iron oxide nanoparticles for MRI*. Biomedical imaging and intervention journal, 6 (2) (2010) 12.

[13] Y. Zhang, N. Kohler, M. Zhang, *Surface modification of superparamagnetic magnetite nanoparticles and their interacellular uptake*, Biomaterials, 23 (7) (2002) 9.

[14] S. Laurent, S. Dutz, U.O. Häfeli, M. Mahmoudi, *Magnetic fluid hyperthermia: focus on superparamagnetic iron oxide nanoparticles*, Advances in Colloid and Interface Science, 166(1) (2011) 8-23

[15] S. Blundell, *Magnetism in Condensed Matter* (Oxford Master Series in Physics), Oxford University Press, USA, (2001).

[16] D.C., Jiles, *Introduction to Magnetism and Magnetic Materials*. 1998: Taylor & Francis

[17] R.M. Cornell, U. Schwertmann, *The Iron Oxides: Structure, Properties, Reactions, Occurrences and Uses*. 2006: Wiley.

[18] U. Schwertmann, R.M. Cornell, *The Iron Oxides: Preparation and Characterization*. 2008: Wiley.

[19] A.K. Gupta, M. Gupta, *Synthesis and surface engineering of iron oxide nanoparticles for biomedical applications*. Biomaterials, 26 (2005) 3995-4021.

[20] M. Mahmoudi, S. Sant, B. Wang, S. Laurent, T. Sen, *Superparamagnetic iron oxide nanoparticles (SPIONs): Development, surface modification and applications in chemotherapy*. Advances Drug Delivery Reviews, 63 (2011) 24-46.

[21] M. Lin, D.K. Kim, A. J.E. Haj, J. Dobson, *Development of superparamagnetic iron oxide nanoparticles (SPIONS) for translation clinical applications*. IEEE Transactions on nanobioscience, 7 (2008) 298-305.

[22] J. Koetz, S. Kosmella, *Polyelectrolytes and nanoparticles*. 2007: Springer.

[23] S. Rudge, C. Peterson, C. Vessely, J. Koda, S. Stevens, L. Catterall, *Adsorption and desorption of chemotherapeutic drugs from a magnetically targeted carrier (MTC)*, Journal of Controlled Release 74 (1–3) (2001) 335–340.

[24] R.A.L. Jones, *Soft Mashines: Nanotechnology and Life*, 2004: Oxford University Press.

[25] A.S. Lubbe, C. Bergemann, J. Brock, D.G. McClure, *Physiological aspects in magnetic drug-targeting*, Journal of Magnetism and Magnetic Materials 194 (1999) 7.

[26] P.A. Voltairas, D.I. Fotiadis, L.K. Michalis, *Hydrodynamics of magnetic drug targeting*, Journal of Biomechanics 35 (6) (2002) 813–821.

[27] A.D. Grief, G. Richardson, *Mathematical modelling of magnetically targeted drug delivery,* Journal of Magnetism and Magnetic Materials. 293 (1) (2005) 455–463.

[28] A.K. Gupta, R.R. Naregalkar, V.D. Vaidya, M. Gupta, *Recent advances on surface engineering of magnetic iron oxide nanoparticles and their biomedical applications*, Nanomedicine 2 (1) (2007) 23–39.

[29] J. Milton Harris, R.B. Chess, *Effect of pegylation on pharmaceuticals*, Nature Reviews. Drug Discovery 2 (3) (2003) 214–221.

[30] S.K. Pulfer, S.L. Ciccotto, J.M. Gallo, *Distribution of small magnetic particles in brain tumor-bearing rats*, Journal of Neuro-Oncology 41 (2) (1999) 99–105.

[31] M. Birkholz, Thin Film Analysis by X-Ray Scattering, 2006: John Wiley & Sons.

[32] D. B. Williams, *Transmission Electron Microscopy: A Textbook for Materials Science*, (4 Volume) 2010: Springer.

[33] W. Schärtl**,** *Light Scattering from Polymer Solutions and Nanoparticle Dispersions*, 2007: Springer

[34] P.R. Griffiths, J.A. De Haseth, *Fourier Transform Infrared Spectrometry*, 2007: Wiley.

[35] A.W. Coats, J.P. Redfern, *Thermogravimetric Analysis: A Review*, Analyst 88 (1963) 906–924. doi:10.1039/AN9638800906.

[36] M. J. O'Neill, *The Analysis of a Temperature-Controlled Scanning Calorimeter, Anal. Chem.* 36 (7) (1964) 1238–1245. doi:10.1021/ac60213a020.

[37] K.J. Buschow, F.R. De Boer, *Physics of magnetism and magnetic materials*. Vol.92. 2003: Springer.

[38] B.D. Cullity, C.D. Graham, *Introduction to magnetic materials*. 2011: John Wiley & Sons.

[39] A. Vértes, L. Korecz, K. Burger, *Mössbauer spectroscopy*. 1979: Elsevier Scientific Pub. Co.

[40] B.J. Kirby, *Micro- and Nanoscale Fluid Mechanics: Transport in Microfluidic Devices.* Cambridge University Press, (2010) ISBN 978-0-521-11903-0.

[41] W.B. Russel, D.A. Saville, W.R. Schowalter, *Colloidal Dispersions*, Cambridge University Press, (1992) ISBN 0-521-42600-6

[42] C.V. Sapan, R.L. Lundblad, N.C. Price, *Colorimetric protein assay techniques*, Biotechnol. Appl. Biochem. 29 (1999), 99–108.

[43] O. H. Lowry, N.J. Rosebrough, A.L. Farr, R.J. Randall, *Protein measurement with the Folin phenol reagent,* Journal Biol. Chem., 193 (1951), 265–275.

[44] H. Perkampus, *UV-VIS Spectroscopy and Its Applications,* 1992: Springer.

[45] Z. Xu, C. Shen, Y. Hou, H. Gao, S. Sun, *Oleylamine as both reducing agent and stabilizer in a facile synthesis of magnetite nanoparticles*, Chemistry of Materials, 21(9) (2009) 1778-1780.

[46] S. Sun, H. Zeng, *Size-Controlled Synthesis of Magnetite Nanoparticles*. IBM T. J. Watson Research Center, (2002).

[47] J. Huang, L. Wang, R. Lin, A. Y. Wang, L. Yang, M. Kuang, W. Qian, H. Mao, *Casein-coated Iron Oxide Nanoparticles for High MRI Contrast Enhancement and Efficient Cell Targeting,* Published online (2013) doi: 10.1021/am400713j

[48] M.E. Khosroshahi, L. Ghazanfari, *Preparation and characterization of silica-coated iron oxide bionanoparticles under N2 gas*, Physica E., 42 (2010) 1824-1829.

[49] F.K. Shakir, D. Audilet, A.J. Drake, K.M. Shakir, *A rapid protein determination by modification of the Lowry procedure*, Analyt. Biochem. 216 (1994), 232–233.

[50] C. McCammon, *Mössbauer spectroscopy of minerals*, Mineral physics & crystallography: A handbook of physical constants (1995), 332-347.

[51] P. Gütlich, R. Link, A. Trautwein, *Mössbauer spectroscopy and transition metal chemistry*, 1978: Springer-Verlag Berlin.

[52] F.J. Berry, S. Skinner, M.F. Thomas, *Mössbauer spectroscopy examination of a single crystal of*, Journal of Physics: Condensed Matter 10 (1) (1998) 215.

[53] Courtesy of Professor Friedrich Wagner, Technical University of Munich, Germany

[54] A.G. Roca, J.F. Marco, M.P. Morales, C.J. Serna, *Effect of nature and particle size on properties of uniform magnetite and maghemite nanoparticles*, The Journal of Physical Chemistry C, 111(10) (2007) 18577-18584.

[55] G. Da Costa, E. De Grave, L.H. Bowen, P.M.A. De Bakker, R.E. Vandenberghe, *Temperature dependence of the hyperfine parameters of maghemite and Al-substituted maghemites*, Physics and Chemistry of Minerals, 22(3) (1995) 178-185.

[56] J. Dormann, D. Fiorani, E. Tronc, *On the models for interparticle interactions in nanoparticles assemblies: comparison with experimental results*, Journal of Magnetism and Magnetic Materials, 202 (1) (1999) 251-267.

[57] M.P. Morales, M. Andres-Verges, S. Veintmillas-Verdagoer, M.I. Montero, C.J. Serna, *Structural effects on the magnetic properties of y-Fe2O3 nanoparticles*, Journal of Magnetism and Magnetic Materials, 203 (1) (1999) 146-148.

[58] P. Guardia, B. Batlle-Brugal, A.G. Roca, O. Iglesias, M.P. Morales, C.J. Serna, A. Labarta, X. Batlle, *Surfactant effects in monodisperse magnetite nanoparticles of controlled size,* Journal of Magnetism and Magnetic Materials, (2007) 316

[59] S. Gu, W. He, M. Zhang, T. Zhuang, Y. Jin, H. ElBidweihy, Y. Mao, J.H. Dickerson, M.J. Wagner, E. Della Torre, L.H. Bennett, *Physical Justification for Negative*

*Remanent Magnetization in Homogeneous Nanoparticle*s, Scientific Reports, 4 (2014) 6267.